United States
Department of
Agriculture

Forest Service

Forest
Products
Laboratory

Research
Paper
FPL–RP–658

Concerns about a Variance Approach to the X-ray Diffractometric Estimation of Microfibril Angle in Wood

Steve P. Verrill
David E. Kretschmann
Victoria L. Herian
Michael Wiemann
Harry A. Alden

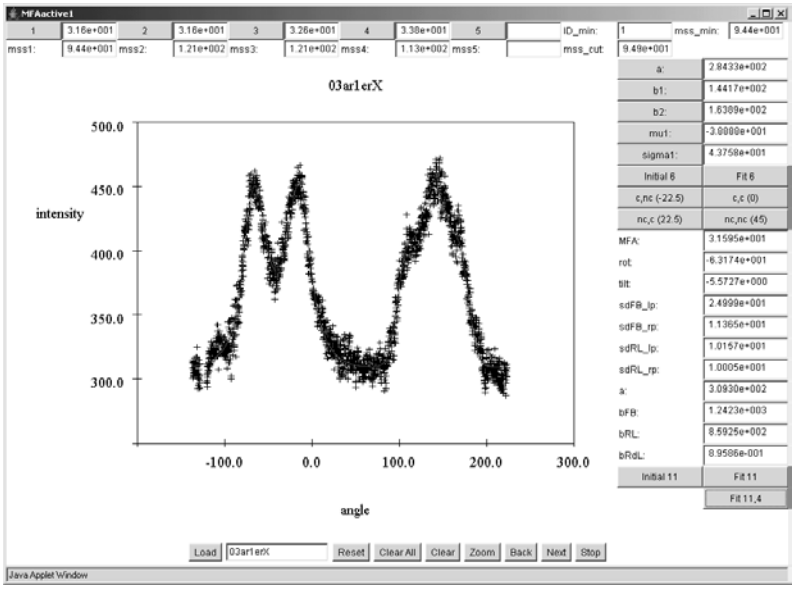

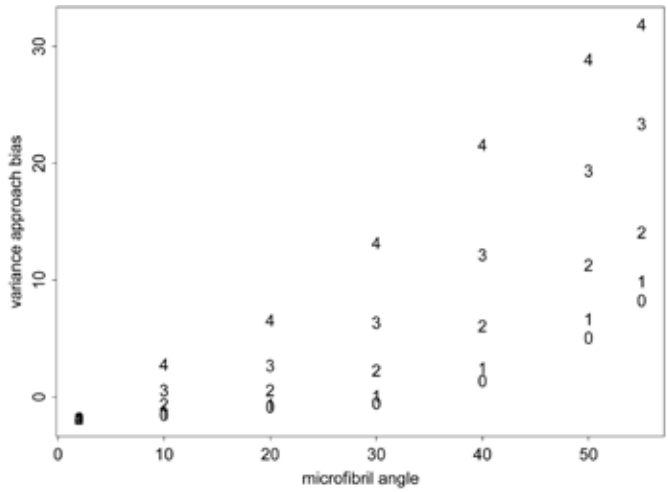

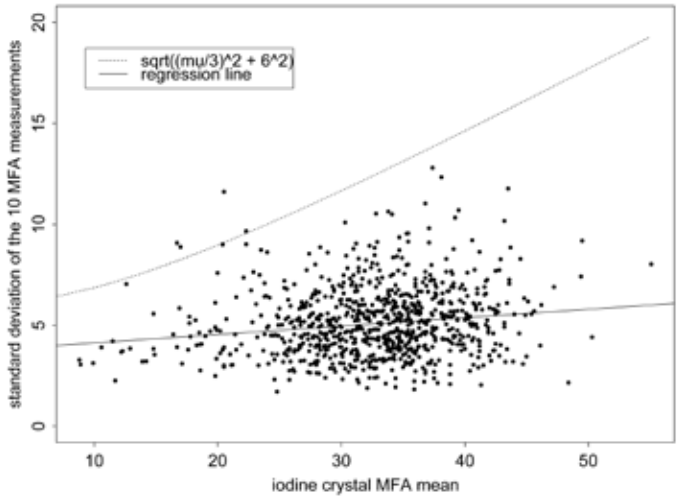

Abstract

In this paper we raise three technical concerns about Evans's 1999 *Appita Journal* "variance approach" to estimating microfibril angle. The first concern is associated with the approximation of the variance of an X-ray intensity half-profile by a function of the microfibril angle and the natural variability of the microfibril angle, $S^2 \approx \mu^2/2 + \sigma^2$. The second concern is associated with the approximation of the natural variability of the microfibril angle by a function of the microfibril angle, $\sigma^2 \approx f(\mu)$. The third concern is associated with the fact that the variance approach was not designed to handle tilt in the fiber orientation. All three concerns are associated with potential biases in microfibril angle estimates. We raise these three concerns so that other researchers interested in understanding, implementing, or extending the variance approach or in comparing the approach to other methods of estimating MFA will be aware of them.

Keywords: SilviScan, microfibril angle, bias, cell cross-section

October 2010

Verrill, Steve P.; Kretschmann, David E.; Herian, Victoria L.; Wiemann, Michael. 2010. Concerns about a variance approach to the x-ray diffractometric estimation of microfibril angle in wood. Research Paper FPL-RP-658. Madison, WI: U.S. Department of Agriculture, Forest Service, Forest Products Laboratory. 92 p.

A limited number of free copies of this publication are available to the public from the Forest Products Laboratory, One Gifford Pinchot Drive, Madison, WI 53726–2398. This publication is also available online at www.fpl.fs.fed.us. Laboratory publications are sent to hundreds of libraries in the United States and elsewhere.

The Forest Products Laboratory is maintained in cooperation with the University of Wisconsin.

Contents

Concerns about a Variance Approach to the X-ray Diffractometric Estimation of Microfibril Angle in Wood

Steve P. Verrill, Mathematical Statistician
David E. Kretschmann, Research General Engineer
Victoria L. Herian, Statistician
Michael Wiemann, Wood Anatomist
Forest Products Laboratory, Madison, Wisconsin

Harry A. Alden, Professor of Botany
College of Southern Maryland

1 Introduction

Microfibril angle (MFA) is the angle between the direction of crystalline cellulose fibrils in the cell wall and the longitudinal direction of the cell. There is a strong belief that the MFA of the S2 layer of the woody cell wall is a critical factor in the mechanical behavior of wood (Megraw 1986). The S2 MFA appears to have a significant influence on the tensile strength, stiffness, and shrinkage of wood (Harris and Meylan 1965, Cave and Walker 1994, Evans and Ilic 2001). Thus, rapid estimation of MFA from the scanning of cores has been developed as a method for comparing and improving silvicultural practices, and as a technique for identifying superior trees.

Evans (1999) provides the theoretical justification for a "variance approach" to estimating MFA from X-ray diffraction patterns. In this paper we raise concerns about three aspects of that approach:

1. We believe that the justification for the base approximation

$$S^2 \approx \mu^2/2 + \sigma^2$$

   is not strong. (Here, μ denotes the MFA, σ denotes the natural variability of the MFA, and S^2 is defined in Section 2.)

2. An implementor of the approach must choose a function of μ with which to model σ. In the 1999 paper, Evans proposed the general model

$$\sigma^2 = (k \times \mu)^2 + \sigma_{\text{add}}^2$$

   and suggested that 1/3 and 6 might be reasonable choices for k and σ_{add}. We demonstrate that biases in the MFA estimate can be sensitive to the choice of the model for σ^2.

3. The 1999 variance approach was not designed to handle fiber tilt. We show that the method can perform poorly in the presence of tilt. (We note that some implementors of the variance approach have apparently developed extensions to the method that are intended to handle tilt. However, these methods have not yet been detailed in the open literature.)

We raise these three concerns so that other researchers interested in understanding, implementing, or extending the variance approach or in comparing the approach to other methods of estimating MFA will be aware of them.

2 The Variance Approach

Evans (1999) proposed the variance approach to estimating MFA and gave a detailed description of the method. Here we give a quick synopsis.

The procedure is based on X-ray diffraction techniques. The radial wall of a machined core is irradiated by a 0.2-mm-diameter X-ray beam, which produces a diffraction pattern on a back plane. In general, due to reflections from the 002 crystallographic planes in the cellulose microfibrils, two back plane bright spots are produced per wood cell face. Thus, cells with rectangular cross sections yield 8 back plane bright spots while those with hexagonal cross sections produce 12 bright spots. These bright spot patterns are broadened by (among other factors) MFA variability and variabilities in cell rotation and tilt. These broadened intensity patterns can be evaluated along the 2θ circle on the back plane (where θ is the Bragg angle). In Figure 1 we provide an example of such an intensity profile. These profiles contain left and right halves that are more or less symmetric, depending on wood cell rotation and tilt.

Evans (1999) argued that

$$S^2 \approx \mu^2/2 + \sigma^2 \tag{1}$$

where S^2 is the variability of either of the profile halves, μ is MFA, and σ is the variability of the MFA angle in the path of the beam. Evans proposed the additional approximation

$$\sigma^2 \approx f(\mu) \tag{2}$$

for some function f.

Taken together, approximations (1) and (2) yield

$$S^2 \approx \mu^2/2 + f(\mu) \tag{3}$$

which, in principle, can be solved for μ. To implement this procedure in practice requires a detailed assumption about $f(\mu)$.

Evans (1999) suggested that σ^2 could be replaced by

$$f(\mu) = \sigma^2_{\text{mult}} + \sigma^2_{\text{add}} = (k \times \mu)^2 + \sigma^2_{\text{add}}$$

Evans went on to suggest that reasonable values for k might be 1/4 or 1/5 or Cave's (1966) 1/3, and a reasonable value for σ_{add} might "lie in the range 6 – 10" degrees. He further stated that (as of 1999) he used $k = 1/3$ and $\sigma_{\text{add}} = 6$. In a personal communication (Evans 2008), he stated that he continued to use

$$\sigma^2 \approx f(\mu) = (\mu/3)^2 + 6^2 \tag{4}$$

Combining approximations (1) and (4), we obtain (Evans' (1999) equation [34])

$$\sqrt{18/11}\sqrt{S^2 - 6^2} \approx \mu \tag{5}$$

This is the MFA estimate that we evaluated in our simulations. Other variance approach estimates would be obtained if other values for $f(\mu)$ were used.

We have developed analytical and simulation tools that permit us to evaluate the quality of variance approach estimates. In the next section we describe our simulation tools, and report the results of simulation experiments that were performed with these tools. These experiments help us identify conditions under which the 1999 algorithm does not perform well.

In Section 4 we look at the theoretical basis for approximation (1), and identify two weaknesses in its derivation. In Section 5, we evaluate the biases that can occur when wood cells are

tilted. In Section 6 we identify good experimental practices that new implementors of the approach can employ to guard against poor performance. We also identify naturally occurring sources of variability that can cause problems for the unmodified 1999 algorithm, and that cannot be easily circumvented. In Section 7 we consider approximation (2) and biases that can occur when the approximation is inadequate.

3 Our Simulation Tools and Results

In the course of developing MFA X-ray diffraction techniques (Verrill *et al.* 2001, 2006, 2011), we have developed computational tools that permit us to calculate the backplane locations of the unbroadened bright spots for rectangular and hexagonal wood cell cross sections and many MFA/rotation/tilt combinations. Our methods are based on extensions of an equation first derived by Cave (1966). For rectangular cross sections, the techniques are described in appendix A of Verrill *et al.* (2006). For hexagonal cross sections, the techniques are described in Appendix A of the current paper. We have made use of these methods to evaluate the performance of the variance approach algorithm. Under the assumption of Gaussian MFA variability, and given the standard deviation of the Gaussian distribution (we use approximation (4) to obtain the value for the MFA variance), we perform Monte Carlo draws from the MFA distribution, and then calculate the corresponding azimuthal coordinates of the bright spots on the back plane.

Given 10,000 Monte Carlo draws, we obtain back-plane X-ray intensity profiles. (In, for example, the rectangular case, each draw of an MFA yields the angular locations of eight bright spots on the backplane of the X-ray apparatus. See appendix A of Verrill *et al.* (2006) for details. These angles are accumulated in a frequency diagram (histogram) over the 10,000 draws, and this diagram constitutes the simulated X-ray intensity profile.) We can use these profiles to calculate variance approach estimates of the MFAs and then compare them to the true generating MFAs. This permits us to estimate the biases associated with the variance approach. In addition, we can break the variability of the profile into between peak (in the rectangular case there are eight intensity peaks associated with the mean locations of the eight bright spots) and within peak portions and thus analyze the quality of the approximations that lead to Evans's (1999) equation [29].

We can also calculate the standard deviations associated with the peaks and compare these to the values obtained from Evans's equation [14].

The FORTRAN code that forms the basis for these simulations can be found at `http://www1.fpl.fs.fed.us/varapp_sim.html`.

The results from these simulations are reported in Tables 1 – 50. These tables are so extensive that they are not included in this report. Instead, they can be viewed and/or downloaded at `http://www1.fpl.fs.fed.us/varapp_tables.html`. We do give detailed descriptions of the tables in Appendix B. The biases in the variance approach estimates are reported in Tables 21 – 25 (rectangular cross-sections) and Tables 46 – 50 (hexagonal cross-sections). The biases are plotted in Figures 2 – 29.

For larger cell tilts and larger MFAs, these biases are significant. For example, for a rectangular cross-section, a 15 degree rotation, 20 degree tilt, and 40 degree MFA, the full-profile bias (using both sets of peaks)[1] is 5.9 degrees, a 15% upward bias. The left half-profile bias (using only the left set of peaks) is 10.1 degrees, a 25% bias. For a hexagonal cross-section, a 0 degree rotation, 20 degree tilt, and 40 degree MFA, the bias (both full-profile and half-profile) is 7.1 degrees, an 18% bias. In general, biases increase as tilt and MFA increase.

[1] S^2 in (1) is replaced by $(S_{\mathrm{L}}^2 + S_{\mathrm{R}}^2)/2$ where S_{L}^2 is the left half-profile variance and S_{R}^2 is the right half-profile variance.

As part of a more general simulation study, Sarén and Serimaa (2006) approximated the bias in the variance approach estimate of MFA for $\mu = 10$, and tilt = 2, 5, 10, 20, and 45 degrees. Their estimated bias values are larger than ours.

We note that our simulations are not complete. Our methods permit a tilt of the original z axis of a cell toward the x axis followed by a rotation around the original z axis (see Figure 30). This permits the longitudinal axis of the cell to point in any direction, but it does not permit free rotation of the cell around that axis. We were led to this model by physical considerations associated with our X-ray apparatus (Verrill *et al.*, 2006). However, our model does not cover all possible configurations. Further, in reality, cell cross sections are mixtures of quadrilateral, pentagonal, hexagonal, elliptical, and other forms. (And we have modeled only regular hexagons.) In addition, in some circumstances, tangential and radial cell walls can differ significantly in thickness. In such circumstances, bright spots associated with thicker walls should be accentuated. In the current simulation, we have assumed that cell walls are equal in thickness. Still, for the purposes of this paper, our simulations are sufficient to highlight possible problems with the 1999 algorithm.

4 Problems with Several of the Variance Approach Approximations

The biases in the variance approach estimates result from approximations that were made in the course of the method's development, and from the fact that the variance approach algorithm was not designed to handle tilt. In this section we focus on approximation (1). In the next section we focus on tilt. In Section 7 we focus on approximation (2).

In this section we revisit a portion of the theoretical development in Evans (1999). We will focus on equations [14] – [29] of that paper.

Evans assumes that a wood cell has J faces at angles $90 + \alpha_0 + 2\pi j/J$, $j = 0, \ldots, J-1$, to the incoming X-ray beam (so α_0 is the rotation of the front face away from perpendicular to the incoming beam). He further assumes (his equation [12]) that the contribution of the jth face to the (left or right half of the) back plane intensity profile is

$$I_j = \frac{1}{\sqrt{2\pi}} \frac{1}{\delta_j} \exp\left((\phi - \phi_j)^2/(2\delta_j^2)\right) \tag{6}$$

where ϕ denotes azimuthal angle, ϕ_j is the bright spot associated with the jth face for the half-profile (left or right) under consideration, and δ_j is the standard deviation of the broadened peak associated with the jth bright spot.

This normality assumption is presumably only approximately appropriate. Peura *et al.* (2005, 2008a,b) and Sarén *et al.* (2001) found that MFA distributions both within single cells and across cells in a growth ring are right skewed. (They restricted their attention to earlywood.) We have found (see, for example, Figure 31) that even if the generating MFA distribution for a face is normal, in general the resulting back plane intensity distribution associated with that face is not. However, as we will see below, the normality assumption is not needed for the development of a variance approach to MFA estimation.

Given Equation (6), Evans notes that the mean bright spot location associated with the left or right back plane half-profile under consideration is (his equation [17])

$$\bar{\phi} \equiv \sum_{j=0}^{J-1} \int_{-\infty}^{\infty} \phi I_j / J d\phi \tag{7}$$

The variance of the half-profile is (his equation [16])

$$S^2 \equiv \sum_{j=0}^{J-1} \int_{-\infty}^{\infty} (\phi - \bar{\phi})^2 I_j d\phi / J \tag{8}$$

Evans makes an argument in his equations [18] through [25] that yields

$$S^2 = \sum_{j=0}^{J-1} (\phi_j - \pi/2)^2 / J + \sum_{j=0}^{J-1} \delta_j^2 / J \tag{9}$$

Here we present a standard statistical argument that yields a similar conclusion:

Suppose that, for a given half-profile (left or right), $y_{i1}, \ldots, y_{iJ}$ are the bright spot locations associated with a draw of an MFA from the assumed MFA distribution (Evans assumes a distribution with mean μ and variance σ^2). Note that in cases of large MFA/tilt, a y_{ij} might be missing. That is, there might be no reflections from a face.

Assume that there are n draws from the MFA distribution and that there are n_j y_{ij}'s for $j = 1, \ldots, J$. For many tilt, rotation, MFA combinations, we will have $n_1 = \ldots = n_J = n$. But in some cases, because of the lack of reflections from a face in some draws, we will have $n_j < n$ for some j.

Define

$$\bar{y}_{\cdot j} \equiv \sum_{i=1}^{n_j} y_{ij} / n_j$$

This is the mean bright spot location for the jth peak in the half-profile.

The mean bright spot location for the half-profile will be

$$\bar{y}_{\cdot\cdot} \equiv \sum_{j=1}^{J} n_j \bar{y}_{\cdot j} / n_{\text{tot}}$$

where $n_{\text{tot}} = n_1 + \ldots + n_J$.

The variance of the bright spot locations around this mean will be

$$\begin{aligned}
S^2 &\equiv \sum_{j=1}^{J} \sum_{i=1}^{n_j} \left(y_{ij} - \bar{y}_{\cdot\cdot}\right)^2 / n_{\text{tot}} \\
&= \sum_{j=1}^{J} \sum_{i=1}^{n_j} \left(y_{ij} - \bar{y}_{\cdot j} + \bar{y}_{\cdot j} - \bar{y}_{\cdot\cdot}\right)^2 / n_{\text{tot}} \\
&= \sum_{j=1}^{J} \sum_{i=1}^{n_j} \left((y_{ij} - \bar{y}_{\cdot j})^2 + 2 \times (y_{ij} - \bar{y}_{\cdot j})(\bar{y}_{\cdot j} - \bar{y}_{\cdot\cdot}) + (\bar{y}_{\cdot j} - \bar{y}_{\cdot\cdot})^2\right) / n_{\text{tot}} \\
&= \sum_{j=1}^{J} \left(\sum_{i=1}^{n_j} (y_{ij} - \bar{y}_{\cdot j})^2 + 2 \times (\bar{y}_{\cdot j} - \bar{y}_{\cdot\cdot}) \sum_{i=1}^{n_j} (y_{ij} - \bar{y}_{\cdot j}) + \sum_{i=1}^{n_j} (\bar{y}_{\cdot j} - \bar{y}_{\cdot\cdot})^2 \right) / n_{\text{tot}} \\
&= \sum_{j=1}^{J} \left(\sum_{i=1}^{n_j} (y_{ij} - \bar{y}_{\cdot j})^2 + 2 \times (\bar{y}_{\cdot j} - \bar{y}_{\cdot\cdot}) \times 0 + \sum_{i=1}^{n_j} (\bar{y}_{\cdot j} - \bar{y}_{\cdot\cdot})^2 \right) / n_{\text{tot}} \\
&= \sum_{j=1}^{J} \left(\sum_{i=1}^{n_j} (y_{ij} - \bar{y}_{\cdot j})^2 + n_j \left(\bar{y}_{\cdot j} - \bar{y}_{\cdot\cdot}\right)^2 \right) / n_{\text{tot}}
\end{aligned}$$

$$= \sum_{j=1}^{J}(n_j - 1)s_j^2/n_{\text{tot}} + \sum_{j=1}^{J} n_j \left(\bar{y}_{\cdot j} - \bar{y}_{\cdot\cdot}\right)^2 / n_{\text{tot}} \tag{10}$$

where

$$s_j^2 \equiv \sum_{i=1}^{n_j} \left(y_{ij} - \bar{y}_{\cdot j}\right)^2 / (n_j - 1)$$

is the sample standard deviation of the jth peak.

This corresponds to Evans's equation [25]. (Our first term, the mean within peak sum of squares, corresponds to his second. Our second term, the mean between peak sum of squares, corresponds to his first.) However, we do not assume that the expectation of the jth distribution is the jth bright spot location; we do not conclude that the average of the expectations of the distributions for the j faces is a constant ($\pi/2$ for the right half-profile in his coordinate system); and we handle the case of non-reflection.

Evans argues that the first term on the right hand side (RHS) of Equation (10) can be approximated by $\sigma^2/\cos(\mu)$, where μ is the MFA and σ^2 is the variability of the MFA. He also argues that the second term on the RHS of Equation (10) can be approximated by $\mu^2/2$. These approximations are flawed and can lead to biased MFA estimates.

Consider the first term on the RHS of Equation (10). To approximate it, Evans makes use of his equation [14][2]. His equation [14] can yield seriously inflated estimates of δ_j. This can be established heuristically, by simulation, and analytically.

To understand the heuristic explanation, consider Figure 32. It provides the locations of the eight bright spots on the back plane for a cell with rectangular cross section in the no rotation, no tilt case. It is clear from this figure that as MFA varies, the locations of the bright spots associated with the front and back faces of the wood cell vary much more than do the locations of the bright spots associated with the right and left faces. However, as Evans notes, his equation [14] predicts that the bright spots associated with the right and left faces will be broadened *more* than the bright spots associated with the front and back faces.

Our simulation estimates of the variabilities of each of the broadened bright spots are reported in Tables 6 – 10 and 31 – 35, and support our heuristic understanding. Estimates of the δ_j's based on Evans's equation [14] frequently significantly exceed the simulation estimates.

Finally, it is possible to obtain analytic estimates of the δ_j's. This approach is described in Appendix C of this paper. It is based on a Taylor series approximation and will be most accurate for smaller MFAs. These analytic estimates of the δ_j's are also reported in Tables 6 – 10 and 31 – 35, and they agree with our simulation estimates for smaller MFAs.

The resulting upward bias in $\sigma^2/\cos(\mu)$ as an estimate of $\sum_{j=1}^{J}(n_j - 1)s_j^2/n_{\text{tot}}$ is reported in Tables 11 – 15 and 36 – 40. This bias can be quite large. For example, for a rectangular cell cross section, 0 degree rotation, and 0 degree tilt, the percent bias ranges from 89% to 123% as MFA ranges from 2 degrees to 55 degrees. For a hexagonal cell cross section, 0 degree rotation, and 0 degree tilt, the percent bias ranges from 95% to 39% as MFA ranges from 2 degrees to 55 degrees.

Now consider the second term on the RHS of Equation (10). Evans argues that it is approximately equal to $\mu^2/2$. (It might be argued that the term Evans is approximating, $\sum_{j=1}^{J}(\phi_j - \bar{\phi})^2/J$, differs from our $\sum_{j=1}^{J} n_j(\bar{y}_{\cdot j} - \bar{y}_{\cdot\cdot})^2/n_{\text{tot}}$. However, in our simulations we show that $\mu^2/2$ is also a

[2]His equation [14] is $\delta_j = \sigma \sec(\mu \sin(\alpha_j - \theta))$ where θ is the Bragg angle, δ_j is the standard deviation of the jth intensity peak in the half-profile, μ is the mean of the MFA distribution, σ is the standard deviation of the MFA distribution, and for the jth face of the cell, $j = 0, 1, \ldots J-1$, $\alpha_j = \alpha_0 + 2\pi j/J$ where α_0 is the rotation of the front face of the cell away from perpendicular to the incoming X-ray beam. (Thus, $\alpha_0 = 0$ for a front face that is perpendicular to the incoming X-ray beam.)

poor approximation to $\sum_{j=1}^{J}(\phi_j - \bar{\phi})^2/J$.) In fact, $\mu^2/2$ almost always underestimates the second term on the RHS of Equation (10), sometimes severely. Again, it is possible to obtain an intuitive feel for this underestimation. It is well known (see, for example, Cave 1966, or Verrill *et al.* 2006) that for cells with rectangular cross section in the no rotation, no tilt case, the azimuthal angles (in our coordinate system[3]) of the bright spot locations for the front and back faces in the left half-profile are $-\mu$ and μ, and the azimuthal angle of the center of the bright spots is 0. Thus we would expect that

$$\sum_{j=1}^{J} n_j(\bar{y}_{\cdot j} - \bar{y}_{\cdot\cdot})^2/n_{\text{tot}}$$

is at least equal to

$$((-\mu - 0)^2 + (\mu - 0)^2)/4 = \mu^2/2$$

However, as we can see from Figure 32, the bright spots associated with the right and left faces are symmetric around 0 and not equal to 0. Thus,

$$\sum_{j=1}^{J} n_j(\bar{y}_{\cdot j} - \bar{y}_{\cdot\cdot})^2/n_{\text{tot}}$$

is inflated above $\mu^2/2$ by approximately the amount $\phi_{RL}^2/2$ where the bright spots associated with the right and left faces are located at $\pm\phi_{RL}$ (for the left half-profile). In Tables 16 – 20 and 41 – 45 we supplement this heuristic argument with simulation results that indicate that $\mu^2/2$ can seriously underestimate the second term on the RHS of (10). For example, for a rectangular cross section, 45 degree rotation, and 0 degree tilt, the percent biases range from -5% to -35% as MFA ranges from 2 degrees to 55 degrees. For a hexagonal cross section, 0 degree rotation, and 0 degree tilt, the percent biases range from -7% to -30% as MFA ranges from 2 degrees to 55 degrees.

We note that there are two additional indications that the theory that leads to Equation (1) is not fully satisfactory. First, the theory draws no distinction between the left half-profile (LHP) and the right half-profile (RHP). That is, according to the theory, it should not matter whether the S^2 used in Equation (1) is the variance of the LHP, the variance of the RHP, or their average. However, it does matter. For example, for a rectangular cross section, 0 degree tilt, 15 degree rotation (Table 21), there is a 4.1 degree difference between the LHP and RHP biases for a 40 degree MFA, and a 10.5 degree difference for a 50 degree MFA. Second, in the final approximation for S^2, cell rotation is not included as a predictor. That is, according to the theory, the rotation of the cell should not matter. However, it does matter. For example (see Table 21), for a rectangular cross section, 0 degree tilt, and an MFA of 40 degrees, as the rotation increases from 0 degrees to 45 degrees, the MFA bias increases from $-.1$ degrees to 4 degrees. For an MFA of 50 degrees, as the rotation increases from 0 degrees to 45 degrees, the MFA bias increases from 1.7 degrees to 9.2 degrees.

The net result of the variance approach's overestimate (in general) of the first term on the RHS of (10) and its underestimate (in general) of the second term on the RHS of (10) is that as MFA increases, the bias in the variance approach estimate of MFA increases. See Tables 21 – 25 and 46 – 50 and Figures 2 through 29. For rectangular cross sections, in the no cell rotation, no tilt case, the bias is always reasonable. (In our simulation the bias increased from -2 degrees to 1.8 degrees

[3]In our 2006 paper we define $\phi = 0$ to correspond to the eastern direction on the back plane (as does Cave, 1966). Evans takes the northern direction as $\phi = 0$. In our coordinate system the center of the left intensity half-profile (corresponding to the right side of the back plane) will tend to be located near our $\phi = 0$ and the center of the right intensity half-profile (corresponding to the left side of the back plane) will tend to be located near our $\phi = \pi$. In Evans's coordinate system these centers will be at approximately $-\pi/2$ and $+\pi/2$.

as MFA increased from 2 to 55 degrees.) However, in other cases, it is not. For example, for a rectangular cross section, a 15 degree rotation, 20 degree tilt, and 40 degree MFA, the full-profile bias is 5.9 degrees, a 15% upward bias. The left half-profile bias (using only the left set of peaks) is 10.1 degrees, a 25% bias. For a hexagonal cross section, a 0 degree rotation, 20 degree tilt, and 40 degree MFA, the bias (both full-profile and half-profile) is 7.1 degrees, an 18% bias.

However, the variance approach was not designed to handle tilt. Thus, to be fair to it, in this section we should focus only on the biases in those cases in which tilt was set to 0 degrees. As can be seen in Table 21 and Figures 2 – 8, in the 0 tilt case, for rectangular cross sections and true MFAs between 2 and 55 degrees, the full-profile biases increase as MFA increases, do not exceed 11.7 degrees in absolute value, and are largest for a rotation of 45 degrees. Further, it could be argued that the only "significant" biases are associated with MFAs that are 40 degrees or larger.

5 Effect of Tilt

As noted above, the variance approach was not designed to handle tilt. Evans (1999) writes:

> If the fibre axis is not perpendicular to the X-ray beam, the azimuthal diffraction profile is distorted and MFA is overestimated. Simple methods for the determination of the direction of the fibre axis from the diffraction pattern, and for the correction of the MFA will be presented in a future paper.

Buksnowitz *et al.* (2008) states that "X-ray diffractometry has long been used to estimate grain angle" and it references Evans *et al.* (1996, 1999, 2000). Evans *et al.* (2000) states that "we measure the distortion [in the diffraction pattern] to correct the MFA results for the effects of fibre tilt in the beam direction ... A description of the method will be presented in a future report." It also states that the "relative orientations of the fibres within the samples were measured using X-ray diffractometry (R. Evans, manuscript in preparation)." Thus, Evans and others claim to have developed extensions to the variance approach algorithm that permit tilt to be properly handled. However, no paper has yet appeared in the literature that details these methods.

In the absence of publicly available algorithms for correcting the variance approach method for tilt, it is worthwhile to investigate the effect of tilt on the bias in the estimates. In Tables 21 – 25 and 46 – 50, and Figures 2 – 8 and 16 – 22, we see that the bias in full-profile variance approach estimates increases as tilt increases and that it can be quite large. We present a subset of these biases in Tables 51 and 52. These biases are among the worst that appear in the full set of tables.

We note that other diffractometric methods of estimating MFA are also likely to perform poorly in the presence of larger tilt if they are not corrected for tilt.

tilt	rotation	MFA	bias
20.0	30.0	2.0	-2.0
20.0	30.0	10.0	-0.9
20.0	30.0	20.0	0.8
20.0	30.0	30.0	2.8
20.0	30.0	40.0	6.6
20.0	30.0	50.0	11.9
20.0	30.0	55.0	15.1
30.0	15.0	2.0	-2.0
30.0	15.0	10.0	0.4
30.0	15.0	20.0	2.5
30.0	15.0	30.0	6.2
30.0	15.0	40.0	12.0
30.0	15.0	50.0	19.2
30.0	15.0	55.0	23.2
40.0	15.0	2.0	-2.0
40.0	15.0	10.0	2.6
40.0	15.0	20.0	6.4
40.0	15.0	30.0	13.0
40.0	15.0	40.0	21.4
40.0	15.0	50.0	28.7
40.0	15.0	55.0	31.7

Table 51: Selected full-profile biases in the variance approach estimates for a rectangular cross section. These are examples of some of the worst biases. Lower tilts will yield lower biases. See Tables 21 – 25 for a complete set of tables.

tilt	rotation	MFA	bias
20.0	0.0	2.0	-2.0
20.0	0.0	10.0	-0.7
20.0	0.0	20.0	0.8
20.0	0.0	30.0	3.2
20.0	0.0	40.0	7.1
20.0	0.0	50.0	12.8
20.0	0.0	55.0	16.1
30.0	0.0	2.0	-2.0
30.0	0.0	10.0	0.8
30.0	0.0	20.0	3.2
30.0	0.0	30.0	7.2
30.0	0.0	40.0	13.0
30.0	0.0	50.0	19.6
30.0	0.0	55.0	22.7
40.0	0.0	2.0	-0.5
40.0	0.0	10.0	3.0
40.0	0.0	20.0	7.7
40.0	0.0	30.0	15.0
40.0	0.0	40.0	22.6
40.0	0.0	50.0	29.3
40.0	0.0	55.0	31.2

Table 52: Selected full-profile biases in the variance approach estimates for a hexagonal cross section. These are examples of some of the worst biases. Lower tilts will yield lower biases. See Tables 46 – 50 for a complete set of tables.

6 Sources of Rotation and Tilt

There are two sources of non-nominal tilts and rotations. One stems from faulty specimen preparation and this source can be minimized by proper quality control. The second source is associated with natural variability and is much more difficult to control.

In Figure 33 we illustrate sample preparation problems that can be controlled. First (Figure 33a), cores that are not perfectly radial (assuming a perfectly cylindrical tree) lead effectively to wood cell rotations. Second (Figure 33b), cores that are not perfectly horizontal lead effectively to α wood cell tilts (see Figure 34b for a definition of α). Third (Figure 33c), cores that are not correctly finished can lead to β wood cell tilts (see Figure 34b for a definition of β). Fourth (Figure 33d,e,f), finished cores that are not properly aligned in the X-ray apparatus can yield rotations and tilts. (We note that in the absence of accompanying wood cell rotations, α tilts simply rotate the back plane pattern and might not yield significantly biased estimates of MFA. See Figures 8 and 15.) In order for their measurements to be valid, developers of systems that make use of an unmodified variance approach algorithm need to develop quality control procedures that minimize tilt.

In Figure 34, we illustrate natural variability problems that are more difficult to control. In Figure 34a, we illustrate the fact that non-cylindrical growth can yield cell rotations even when cores are perfectly radial. Figure 34b illustrates potential, naturally occurring wood cell tilts.

Sarén *et al.* (2006) found that in Norway spruce the α tilt in Figure 34b tended to gradually increase from small negative angles (-6 to 0 degrees) near the pith towards small positive angles (0 to 6 degrees) near the bark, and that the β tilt (spiral grain) can be cyclical with absolute values ranging from 0 to 30 degrees. Buksnowitz *et al.* (2008) have found that in Norway spruce the β tilt can vary from -11 to $+12$ degrees. For *Eucalyptus nitens* (H. Deane & Maiden) Maiden trees, Evans *et al.* (2000) report a "standard deviation of fibre axial orientation" that ranges from approximately 13 to 16.5 degrees. Given that their fiber axial orientation included both "roll" (α) and "pitch" (β), it is unclear how "standard deviation of fibre axial orientation" was calculated. However, it appears that the β range could have been quite large. (They remark that "Fibre pitch variation was consistently greater than roll variation.") Gindl and Teischinger (2002) studied blocks from 12 larch trees and found spiral grain angles that ranged from 0 to 40 degrees. Angles between 0 and 5 degrees were most common, but angles above 20 degrees were not uncommon. See their Figure 2. (However, the authors note that the "material was selected specifically to represent an optimum variability of grain angle.") Northcott (1957) found spiral grain angles that varied from -16 to $+19$ degrees in Douglas-fir. Houkal (1982) found that the absolute value of spiral grain ranged from 0 to 16 degrees in *Pinus oocarpa* Schiede ex Schltdl. Martley (1920) studied 19 Indian hardwoods and found spiral grain angles that varied from -33 to $+35$ degrees. Noskowiak (1963) observed spiral grain angles as high as 40 degrees in mature foxtail pine (*Pinus balfouriana* Grev. and Balf.).

We have performed exploratory studies (described in detail in Appendix H) that indicate that in samples from *Pinus lambertiana* Dougl. and *Pinus monticola* Dougl. ex D. Don., the natural variability in cell *rotation* has mean roughly equal to 0 degrees and standard deviation roughly equal to 5 degrees. In a sample of 220 cells from *Pinus lambertiana*, the range of rotations was from -17 degrees to $+15$ degrees. In a sample of 243 cells from *Pinus monticola*, the range of rotations was from -25 degrees to $+14$ degrees. We observed no trend in mean rotation as we progressed from pith to bark.

In this study we also found that cells were primarily quadrilateral (40.2%), hexagonal (34.1%), elliptical (16.8%), and pentagonal (8.6%) in cross section. (Earlywood percentages differ from latewood percentages. See Appendix H.)

Also note that for hexagonal cells viewed from the tangential face, the default rotation is 0, while for hexagonal cells viewed from the radial face, the default rotation is 30 degrees.

7 Estimating σ^2 as a function of MFA

As noted in Section 2, the variance approach is based on two approximations. First,

$$S^2 \approx \mu^2/2 + \sigma^2 \tag{11}$$

where μ denotes the MFA and σ^2 denotes the natural variability of the MFA. Second,

$$\sigma^2 \approx f(\mu) \tag{12}$$

for some function f. Combining the two approximations, we obtain

$$S^2 \approx \mu^2/2 + f(\mu)$$

and we can, at least in principle, solve for μ.

In Sections 4 and 5, we established in our simulations that approximation (11) can lead to significantly biased estimates of μ even if we know exactly the best f in approximation (12). (In our simulations we knew that the generating variance of the MFAs was $\sigma^2 = (\mu/3)^2 + 6^2$.)

In this section, we discuss possible choices for $f(\mu)$ and demonstrate that, as one would expect, additional biases can occur if the f that one chooses for a variance approach analysis does not match the generating $f(\mu)$.

As noted in Section 2, Evans (1999, 2008) suggested that σ^2 could be replaced by

$$\sigma^2 \approx f(\mu) = (\mu/3)^2 + 6^2 \tag{13}$$

What is the source of approximation (13)?

Cave (1966) found that he could obtain a good match between X-ray and iodine stain estimates of microfibril angle if he took

$$\sigma^2 = (\mu/3)^2$$

Evans (1999) noted that the MFA variance was non-zero even when the MFA was approximately equal to zero. This led him to propose the addition of a constant to $(\mu/3)^2$. He argued that experience suggests that 6^2 is a reasonable value for this constant. Thus, approximation (13) is empirical rather than theoretical in nature.

Is there evidence for other forms of $f(\mu)$?

In a personal communication, Evans (2009) wrote: "It should be noted that there are cases in which residual variance decreases with increasing microfibril angle (when compression wood forms, the microfibril angle is high but its variability tends to be lower than in normal wood — unpublished.)"

Cave and Robinson (1998) report results for seven specimens in which their estimates of MFA ranged from 1 degree to 29 degrees while their estimates of σ ranged from 10 to 14 degrees (11 degrees for the 1 degree MFA, 12 degrees for the 29 degree MFA). This suggests that σ does not depend upon μ.

Donaldson (1998) finds that ring number (1, 5, 10, 15) has no effect on microfibril angle range in tracheid samples of size 25 in radiata pine. Because microfibril angle tends to decline as ring number increases, and population standard deviation is proportional to sample range (for samples of constant size), this suggests that σ does not decrease as μ decreases.

Alden and Kretschmann (reported in Verrill *et al.* 2011) used iodine crystallization techniques to obtain optical estimates of microfibril angle from 833 prepared slides. Each slide contained cells obtained from the earlywood or the latewood of a single ring. The first eight rings from two bolts from each of two trees at each of 26 loblolly pine plantations were evaluated in the study. Alden and Kretschmann measured 10 microfibril angles on each slide. In Figure 35 we plot the standard deviations of the 10 replicates versus the means of the 10 replicates for all 833 slides. We also plot the $\sigma = \sqrt{(\mu/3)^2 + 6^2}$ line in the figure, and the regression line through Alden and Kretschmann's data. There is a clear discrepancy. Of course, the variability encountered by X-ray devices can be associated with many hundreds of cells so it would be reasonable for it to be inflated above that measured on the surface of a specimen. Note, however, the lack of a significant increase in σ as a function of μ in Alden and Kretschmann's data. The slope coefficient in the regression is only 0.04 (with a standard error of 0.009).

Peura *et al.* (2008a) used synchrotron X-ray microdiffraction to investigate the distribution of microfibril angle in single cells. In Figure 36 we plot the standard deviations (calculated as 0.425 times their full width at half maximum (FWHM) values) versus the mode values for the 17 samples in their table 3. We also plot the $\sigma = \sqrt{(\mu/3)^2 + 6^2}$ line in the figure, and the regression line through the Peura *et al.* data. In this case, it appears that approximation (13) underestimates σ, especially given that the standard deviations plotted in Figure 36 are from single cells. On the other hand, there is some support for the idea that σ increases as MFA increases. The slope coefficient for the regression line in the figure is 0.19 (with a standard error of 0.08).

What kinds of bias can occur if Equation (11) holds but Equation (13) does not? For purposes of illustration, we consider three alternative models. We do not claim that we have strong evidence for any of these models. However, Alden and Kretschmann's results are in accord with Model 1, Cave and Robinson (1998) is in accord with Model 2, and Peura *et al.* (2008a) is in accord with Model 3. Our main point is that given the dependence of the bias in the variance approach estimate on the true form for σ^2, it would be reasonable for implementors of the approach to carefully investigate this relationship. If implementors have already done so, and have developed alternative methods for approximating σ^2 by a function of MFA, we encourage them to publish their new algorithms. This would be useful to other potential implementors.

It is possible that there is no single f that satisfies approximation (12) for all data sets. In this case, in order to apply the variance approach, one would first have to calibrate each new data source with, for example, an optical method. That is, one would have to use optical methods to determine an f that satisfied (12) for the data source.

Model 1: $\sigma = 5$

In this case we have

$$\hat{\mu} = \sqrt{18/11}\sqrt{S^2 - 6^2} = \sqrt{18/11}\sqrt{\mu^2/2 + 5^2 - 6^2}$$

The biases and percent biases in this case are reported in Table 53.

true mfa (μ)	estimated mfa ($\hat{\mu}$)	bias ($\hat{\mu} - \mu$)	percent bias
5	1.57	-3.43	-68.67
10	7.99	-2.01	-20.11
15	12.89	-2.11	-14.08
20	17.59	-2.41	-12.07
25	22.21	-2.79	-11.15
30	26.80	-3.20	-10.66
35	31.37	-3.63	-10.36
40	35.93	-4.07	-10.17
45	40.48	-4.52	-10.04
50	45.03	-4.97	-9.95
55	49.57	-5.43	-9.88
60	54.11	-5.89	-9.82

Table 53: Biases when $S^2 = \mu^2/2 + \sigma^2$, $\sigma^2 = 5^2$, and we incorrectly assume $\sigma^2 = (\mu/3)^2 + 6^2$

Model 2: $\sigma = 12$

In this case we have

$$\hat{\mu} = \sqrt{18/11}\sqrt{S^2 - 6^2} = \sqrt{18/11}\sqrt{\mu^2/2 + 12^2 - 6^2}$$

The biases and percent biases in this case are reported in Table 54.

true mfa (μ)	estimated mfa ($\hat{\mu}$)	bias ($\hat{\mu} - \mu$)	percent bias
5	14.04	9.04	180.84
10	16.08	6.08	60.79
15	19.00	4.00	26.63
20	22.45	2.45	12.25
25	26.23	1.23	4.93
30	30.22	0.22	0.72
35	34.34	-0.66	-1.90
40	38.55	-1.45	-3.63
45	42.82	-2.18	-4.84
50	47.14	-2.86	-5.72
55	51.49	-3.51	-6.37
60	55.88	-4.12	-6.87

Table 54: Biases when $S^2 = \mu^2/2 + \sigma^2$, $\sigma^2 = 12^2$, and we incorrectly assume $\sigma^2 = (\mu/3)^2 + 6^2$

Model 3: $\sigma = 8 + \mu/5$

In this case we have

$$\hat{\mu} = \sqrt{18/11}\sqrt{S^2 - 6^2} = \sqrt{18/11}\sqrt{\mu^2/2 + (8 + \mu/5)^2 - 6^2}$$

The biases and percent biases in this case are reported in Table 55.

true mfa (μ)	estimated mfa ($\hat{\mu}$)	bias ($\hat{\mu} - \mu$)	percent bias
5	9.70	4.70	94.00
10	13.66	3.66	36.58
15	17.98	2.98	19.85
20	22.45	2.45	12.25
25	27.00	2.00	8.00
30	31.59	1.59	5.31
35	36.22	1.22	3.47
40	40.85	0.85	2.14
45	45.51	0.51	1.12
50	50.17	0.17	0.33
55	54.83	-0.17	-0.30
60	59.51	-0.49	-0.82

Table 55: Biases when $S^2 = \mu^2/2 + \sigma^2$, $\sigma = 8 + \mu/5$, and we incorrectly assume $\sigma^2 = (\mu/3)^2 + 6^2$

8 Summary

We have raised concerns about three aspects of the variance approach to estimating microfibril angle.

First, the approach is based on the approximations $S_1^2 \approx \mu^2/2$ and $S_2^2 \approx \sigma^2/\cos(\mu)$ where S_1^2 is the mean between peak sum of squares and S_2^2 is the mean within peak sum of squares. As we saw in Section 4, the biases in these approximations can be quite large, but to some extent they cancel. Thus, for 0 degree tilts, the maximum full-profile bias that we found for MFAs between 2 and 55 degrees was 11.7 degrees.

Second, in Section 5 we noted that the variance approach was not designed to handle tilt, and, consequently, in the presence of tilt, the method can yield estimates that are highly biased. (We also noted that there may be algorithmic fixes for this, but that they have not yet appeared in the literature.)

Third, as we saw in Section 7, there is some doubt about a proper model for σ^2. One model proposed by Evans in the 1999 paper was $\sigma^2 = (\mu/3)^2 + 6^2$. In Section 7, we considered three other models that have some data support and found that there can be large (percent) biases if one of these models is true but $\sigma^2 = (\mu/3)^2 + 6^2$ is assumed. This suggests that in order to apply the variance approach in a new situation, it might be necessary to use optical methods to first determine an appropriate f in the approximation $\sigma^2 \approx f(\mu)$.

On the other hand, it is important to keep these concerns in perspective. In our simulations we found that if approximation (4) holds and is used, and if tilts are restricted to 10 degrees or less, and MFAs are restricted to 40 degrees or less, the biases in MFA estimates increase with MFA and do not exceed 4.6 degrees in absolute value.

We raise the three concerns so that other researchers interested in understanding, implementing, or extending the variance approach or in comparing the approach to other methods of estimating MFA will be aware of them.

9 Acknowledgments

The authors gratefully acknowledge the very valuable comments and suggestions of the reviewers.

10 References

Buksnowitz, C., Müller, U., Evans, R., Teischinger, A., and Grabner, M. (2008). "The potential of SilviScan's X-ray diffractometry method for the rapid assessment of spiral grain in softwood, evaluated by goniometric measurements." *Wood Sci Technol.* **42**. Pages 95-102.

Cave, I.D. (1966). "X-ray measurement of microfibril angle." *Forest Products Journal.* **16**(10). Pages 37-42.

Cave, I.D., and Robinson, W. (1998). "Interpretation of (002) diffraction arcs by means of a minimalist model." *Microfibril Angle in Wood.* B.G. Butterfield editor. International Association of Wood Anatomists. University of Canterbury. New Zealand. Pages 108-115.

Cave, I.D. and Walker, J.C.F. (1994). "Stiffness of wood in fast-grown plantation softwoods: the influence of microfibril angle." *Forest Products Journal.* **44**(5). Pages 43-48.

Donaldson, L.A. (1998). "Between-tracheid variability of microfibril angles in radiata pine." *Microfibril Angle in Wood.* B.G. Butterfield editor. International Association of Wood Anatomists. University of Canterbury. New Zealand. Pages 206-224.

Evans, R.E. (1999). "A variance approach to the X-ray diffractometric estimation of microfibril angle in wood." *Appita Journal.* **52**(4). Pages 283-289,294.

Evans, R.E. (2008). Personal communication.

Evans, R.E. (2009). Personal communication.

Evans, R.E. and Illic, J. (2001). "Rapid prediction of wood stiffness from microfibril angle and density." *Forest Products Journal.* **51**. Pages 53-57.

Evans, R., Stuart, S.A., and Van der Touw, J. (1996). "Microfibril angle scanning of increment cores by X-ray diffractometry." *Appita Journal.* **49**(6). Pages 411-414.

Evans, R., Hughes, M., and Menz, D. (1999). "Microfibril angle variation by scanning X-ray diffractometry." *Appita Journal.* **52**(5). Pages 363-367.

Evans, R., Stringer, S., and Kibblewhite, R.P. (2000). "Variation of microfibril angle, density and fibre orientation in twenty-nine Eucalyptus nitens trees." *Appita Journal.* **53**(5). Pages 450-457.

Gindl, W. and Teischinger, A. (2002). "The potential of Vis- and NIR-spectroscopy for the nondestructive evaluation of grain-angle in wood." *Wood and Fiber Science* **34**(4). Pages 651-656.

Harris, J.M. and Meylan, B.A. (1965). "The influence of microfibril angle on longitudinal and tangential shrinkage in *Pinus radiata*." *Holzforschung.* **19**(5). Pages 144-153.

Houkal, D. (1982). "Spiral grain in *Pinus Oocarpa*." *Wood and Fiber Science.* **14**(4). Pages 320-330.

Martley, J.F. (1920). "Double cross grain." *Annals Appl. Biol.* **7**(2,3). Pages 224-268.

Megraw, R.A. (1986). "Wood quality factors in loblolly pine: the influence of tree age, position in the tree, and cultural practice on wood specific gravity, fiber length and fibril angle." TAPPI Press. Pages 1-88.

Northcott, P.L. (1957). "Is spiral grain the normal growth pattern?" *For. Chron.* **33**(4). Pages 335-352.

Noskowiak, A.F. (1963). "Spiral Grain in Trees . . . A Review." *Forest Products Journal.* Pages 266-275.

Peura, M., Müller, M., Serimaa, R., M., Vainio, U., Sarén, M., Saranpää, P., and Burghammer, M. (2005). "Structural studies of single wood cell walls by synchrotron X-ray microdiffraction and polarised light microscopy." *Nuclear Instruments and Methods in Physics Research B.* **238**. Pages 16-20.

Peura, M., Müller, M., Vainio, U., Sarén, M., Saranpää, P., and Serimaa, R. (2008a). "X-ray microdiffraction reveals the orientation of cellulose microfibrils and the size of cellulose crystallites in single Norway spruce tracheids." *Trees.* **22**. Pages 49-61.

Peura, M., Sarén, M., Laukkanen, J., Nygard, K., Andersson, S., Saranpää, P., Paakkari, T., Hämäläinen, K., and Serimaa, R. (2008b). "The elemental composition, the microfibril angle distribution and the shape of the cell cross-section in Norway spruce xylem." *Trees.* **22**. Pages 499-510.

Sarén, M. and Serimaa, R. (2006). "Determination of microfibril angle distribution by X-ray diffraction," *Wood Sci Technol*, **40**. Pages 445-460.

Sarén, M., Serimaa, R., Andersson, S., Paakkari, T., Saranpää, P., and Pesonen, E. (2001). "Structural Variation of Tracheids in Norway Spruce (*Picea abies* [L.] Karst.)," *Journal of Structural Biology*, **136**. Pages 101-109.

Sarén, M., Serimaa, R., and Tolonen, Y. (2006). "Determination of fiber orientation in Norway spruce using X-ray diffraction and laser scattering," *Holz als Roh- und Werkstoff*, **64**. Pages 183-188.

Verrill, S.P., Kretschmann, D.E., and Herian, V.L. (2001). JMFA — A graphically interactive Java program that fits microfibril angle X-ray diffraction data. Res. Note FPL-RN-0283. Madison, WI: U.S. Department of Agriculture, Forest Service, Forest Products Laboratory. 44 p.

Verrill, S.P., Kretschmann, D.E., and Herian, V.L. (2006). JMFA 2 — A graphically interactive Java program that fits microfibril angle X-ray diffraction data. Res. Paper 635. Madison, WI: U.S. Department of Agriculture, Forest Service, Forest Products Laboratory. 70 p.

Verrill, S.P., Kretschmann, D.E., Herian, V.L., and Alden, H. (2011). JMFA 3 — A graphically interactive Java program that fits microfibril angle X-ray diffraction data. Manuscript in preparation.

11 Appendix A — An Extension to Cave's Equation

Cave (1966) derived an equation for the locations of the spots of high X-ray intensity on the back plane of the X-ray apparatus. This equation applies to cells with rectangular cross sections. It does not account for cell tilt. See the appendix to Verrill *et al.* (2001) for a detailed derivation of Cave's equation. In appendix A of Verrill *et al.* (2006) we extended Cave's analysis to the case in which the cell can be tilted. Here we extend it to include a tilted, rotated cell of hexagonal cross section.

11.1 Microfibril Directions

To derive the six equations (one for each of the cell's six sides) we first need the microfibril angle directions. Let θ denote the Bragg angle (11.35 degrees for light of wavelength 1.54 angstroms), μ denote the microfibril angle, η denote the tilt of the vertical axis in the wood cell down toward the positive x axis, α equal 90 degrees plus the counterclockwise rotation of the cell around the original z axis (after the tilt), and ϕ equal the angle (measured counterclockwise from the east) of the bright spot on the "2θ circle" on the back plane. See Figures 30, 37, and 38.

11.1.1 Front Face

See Figure 39 for our definition of the front, right 1, right 2, back, left 1, and left 2 faces of a cell with a hexagonal cross section.

Before tilt and rotation, the direction of a microfibril on the front face is

$$\begin{pmatrix} 0 \\ \sin(\mu) \\ \cos(\mu) \end{pmatrix}$$

After a tilt of the top of the cell down toward the positive x axis, the direction becomes

$$\begin{pmatrix} \cos(\mu)\sin(\eta) \\ \sin(\mu) \\ \cos(\mu)\cos(\eta) \end{pmatrix}$$

Now, the mathematical tranformation that corresponds to a physical rotation through angle rot of the cell about the original z axis is the matrix

$$\begin{pmatrix} \cos(-\text{rot}) & \sin(-\text{rot}) & 0 \\ -\sin(-\text{rot}) & \cos(-\text{rot}) & 0 \\ 0 & 0 & 1 \end{pmatrix}$$

which equals

$$\begin{pmatrix} \sin(\alpha) & \cos(\alpha) & 0 \\ -\cos(\alpha) & \sin(\alpha) & 0 \\ 0 & 0 & 1 \end{pmatrix}$$

where $\alpha = \pi/2 + \text{rot}$.

Thus the direction of the microfibril angle after tilt and rotation is

$$\mathbf{b} = \begin{pmatrix} \sin(\alpha) & \cos(\alpha) & 0 \\ -\cos(\alpha) & \sin(\alpha) & 0 \\ 0 & 0 & 1 \end{pmatrix} \begin{pmatrix} \cos(\mu)\sin(\eta) \\ \sin(\mu) \\ \cos(\mu)\cos(\eta) \end{pmatrix} = \begin{pmatrix} \sin(\alpha)\cos(\mu)\sin(\eta) + \cos(\alpha)\sin(\mu) \\ -\cos(\alpha)\cos(\mu)\sin(\eta) + \sin(\alpha)\sin(\mu) \\ \cos(\mu)\cos(\eta) \end{pmatrix} \tag{14}$$

11.1.2 Right 1 Face

Before tilt, the direction of a microfibril on the right 1 face is

$$\begin{pmatrix} \cos(-60) & \sin(-60) & 0 \\ -\sin(-60) & \cos(-60) & 0 \\ 0 & 0 & 1 \end{pmatrix} \begin{pmatrix} 0 \\ \sin(\mu) \\ \cos(\mu) \end{pmatrix} = \begin{pmatrix} \frac{-\sqrt{3}}{2}\sin(\mu) \\ \frac{1}{2}\sin(\mu) \\ \cos(\mu) \end{pmatrix}$$

After a tilt of the top of the cell down toward the positive x axis through an angle η, the direction becomes

$$\begin{pmatrix} \cos(\eta) & 0 & \sin(\eta) \\ 0 & 1 & 0 \\ -\sin(\eta) & 0 & \cos(\eta) \end{pmatrix} \begin{pmatrix} \frac{-\sqrt{3}}{2}\sin(\mu) \\ \frac{1}{2}\sin(\mu) \\ \cos(\mu) \end{pmatrix} = \begin{pmatrix} \frac{-\sqrt{3}}{2}\sin(\mu)\cos(\eta) + \cos(\mu)\sin(\eta) \\ \frac{1}{2}\sin(\mu) \\ \frac{\sqrt{3}}{2}\sin(\mu)\sin(\eta) + \cos(\mu)\cos(\eta) \end{pmatrix}$$

The direction of the microfibril angle after tilt and rotation is thus

$$\begin{aligned} \mathbf{b} &= \begin{pmatrix} \sin(\alpha) & \cos(\alpha) & 0 \\ -\cos(\alpha) & \sin(\alpha) & 0 \\ 0 & 0 & 1 \end{pmatrix} \begin{pmatrix} \frac{-\sqrt{3}}{2}\sin(\mu)\cos(\eta) + \cos(\mu)\sin(\eta) \\ \frac{1}{2}\sin(\mu) \\ \frac{\sqrt{3}}{2}\sin(\mu)\sin(\eta) + \cos(\mu)\cos(\eta) \end{pmatrix} \\ &= \begin{pmatrix} \frac{-\sqrt{3}}{2}\sin(\alpha)\sin(\mu)\cos(\eta) + \sin(\alpha)\cos(\mu)\sin(\eta) + \frac{1}{2}\cos(\alpha)\sin(\mu) \\ \frac{\sqrt{3}}{2}\cos(\alpha)\sin(\mu)\cos(\eta) - \cos(\alpha)\cos(\mu)\sin(\eta) + \frac{1}{2}\sin(\alpha)\sin(\mu) \\ \frac{\sqrt{3}}{2}\sin(\mu)\sin(\eta) + \cos(\mu)\cos(\eta) \end{pmatrix} \end{aligned} \tag{15}$$

11.1.3 Right 2 Face

Before tilt, the direction of a microfibril on the right 2 face is

$$\begin{pmatrix} \cos(-120) & \sin(-120) & 0 \\ -\sin(-120) & \cos(-120) & 0 \\ 0 & 0 & 1 \end{pmatrix} \begin{pmatrix} 0 \\ \sin(\mu) \\ \cos(\mu) \end{pmatrix} = \begin{pmatrix} \frac{-\sqrt{3}}{2}\sin(\mu) \\ -\frac{1}{2}\sin(\mu) \\ \cos(\mu) \end{pmatrix}$$

After a tilt of the top of the cell down toward the positive x axis through an angle η, the direction becomes

$$\begin{pmatrix} \cos(\eta) & 0 & \sin(\eta) \\ 0 & 1 & 0 \\ -\sin(\eta) & 0 & \cos(\eta) \end{pmatrix} \begin{pmatrix} \frac{-\sqrt{3}}{2}\sin(\mu) \\ -\frac{1}{2}\sin(\mu) \\ \cos(\mu) \end{pmatrix} = \begin{pmatrix} \frac{-\sqrt{3}}{2}\sin(\mu)\cos(\eta) + \cos(\mu)\sin(\eta) \\ -\frac{1}{2}\sin(\mu) \\ \frac{\sqrt{3}}{2}\sin(\mu)\sin(\eta) + \cos(\mu)\cos(\eta) \end{pmatrix}$$

The direction of the microfibril angle after tilt and rotation is thus

$$\begin{aligned} \mathbf{b} &= \begin{pmatrix} \sin(\alpha) & \cos(\alpha) & 0 \\ -\cos(\alpha) & \sin(\alpha) & 0 \\ 0 & 0 & 1 \end{pmatrix} \begin{pmatrix} \frac{-\sqrt{3}}{2}\sin(\mu)\cos(\eta) + \cos(\mu)\sin(\eta) \\ -\frac{1}{2}\sin(\mu) \\ \frac{\sqrt{3}}{2}\sin(\mu)\sin(\eta) + \cos(\mu)\cos(\eta) \end{pmatrix} \\ &= \begin{pmatrix} \frac{-\sqrt{3}}{2}\sin(\alpha)\sin(\mu)\cos(\eta) + \sin(\alpha)\cos(\mu)\sin(\eta) - \frac{1}{2}\cos(\alpha)\sin(\mu) \\ \frac{\sqrt{3}}{2}\cos(\alpha)\sin(\mu)\cos(\eta) - \cos(\alpha)\cos(\mu)\sin(\eta) - \frac{1}{2}\sin(\alpha)\sin(\mu) \\ \frac{\sqrt{3}}{2}\sin(\mu)\sin(\eta) + \cos(\mu)\cos(\eta) \end{pmatrix} \end{aligned} \tag{16}$$

11.1.4 Back Face

Before tilt and rotation, the direction of a microfibril on the back face is

$$\begin{pmatrix} 0 \\ -\sin(\mu) \\ \cos(\mu) \end{pmatrix}$$

After a tilt of the top of the cell down toward the positive x axis, the direction becomes

$$\begin{pmatrix} \cos(\mu)\sin(\eta) \\ -\sin(\mu) \\ \cos(\mu)\cos(\eta) \end{pmatrix}$$

The direction of the microfibril angle after tilt and rotation is thus

$$\mathbf{b} = \begin{pmatrix} \sin(\alpha)\cos(\mu)\sin(\eta) - \cos(\alpha)\sin(\mu) \\ -\cos(\alpha)\cos(\mu)\sin(\eta) - \sin(\alpha)\sin(\mu) \\ \cos(\mu)\cos(\eta) \end{pmatrix} \tag{17}$$

11.1.5 Left 1 Face

Before tilt, the direction of a microfibril on the left 1 face is

$$\begin{pmatrix} \cos(-240) & \sin(-240) & 0 \\ -\sin(-240) & \cos(-240) & 0 \\ 0 & 0 & 1 \end{pmatrix} \begin{pmatrix} 0 \\ \sin(\mu) \\ \cos(\mu) \end{pmatrix} = \begin{pmatrix} \frac{\sqrt{3}}{2}\sin(\mu) \\ -\frac{1}{2}\sin(\mu) \\ \cos(\mu) \end{pmatrix}$$

After a tilt of the top of the cell down toward the positive x axis through an angle η, the direction becomes

$$\begin{pmatrix} \cos(\eta) & 0 & \sin(\eta) \\ 0 & 1 & 0 \\ -\sin(\eta) & 0 & \cos(\eta) \end{pmatrix} \begin{pmatrix} \frac{\sqrt{3}}{2}\sin(\mu) \\ -\frac{1}{2}\sin(\mu) \\ \cos(\mu) \end{pmatrix} = \begin{pmatrix} \frac{\sqrt{3}}{2}\sin(\mu)\cos(\eta) + \cos(\mu)\sin(\eta) \\ -\frac{1}{2}\sin(\mu) \\ -\frac{\sqrt{3}}{2}\sin(\mu)\sin(\eta) + \cos(\mu)\cos(\eta) \end{pmatrix}$$

The direction of the microfibril angle after tilt and rotation is thus

$$\begin{aligned} \mathbf{b} &= \begin{pmatrix} \sin(\alpha) & \cos(\alpha) & 0 \\ -\cos(\alpha) & \sin(\alpha) & 0 \\ 0 & 0 & 1 \end{pmatrix} \begin{pmatrix} \frac{\sqrt{3}}{2}\sin(\mu)\cos(\eta) + \cos(\mu)\sin(\eta) \\ -\frac{1}{2}\sin(\mu) \\ -\frac{\sqrt{3}}{2}\sin(\mu)\sin(\eta) + \cos(\mu)\cos(\eta) \end{pmatrix} \\ &= \begin{pmatrix} \frac{\sqrt{3}}{2}\sin(\alpha)\sin(\mu)\cos(\eta) + \sin(\alpha)\cos(\mu)\sin(\eta) - \frac{1}{2}\cos(\alpha)\sin(\mu) \\ -\frac{\sqrt{3}}{2}\cos(\alpha)\sin(\mu)\cos(\eta) - \cos(\alpha)\cos(\mu)\sin(\eta) - \frac{1}{2}\sin(\alpha)\sin(\mu) \\ -\frac{\sqrt{3}}{2}\sin(\mu)\sin(\eta) + \cos(\mu)\cos(\eta) \end{pmatrix} \end{aligned} \tag{18}$$

11.1.6 Left 2 Face

Before tilt, the direction of a microfibril on the left 2 face is

$$\begin{pmatrix} \cos(-300) & \sin(-300) & 0 \\ -\sin(-300) & \cos(-300) & 0 \\ 0 & 0 & 1 \end{pmatrix} \begin{pmatrix} 0 \\ \sin(\mu) \\ \cos(\mu) \end{pmatrix} = \begin{pmatrix} \frac{\sqrt{3}}{2}\sin(\mu) \\ \frac{1}{2}\sin(\mu) \\ \cos(\mu) \end{pmatrix}$$

After a tilt of the top of the cell down toward the positive x axis through an angle η, the direction becomes

$$\begin{pmatrix} \cos(\eta) & 0 & \sin(\eta) \\ 0 & 1 & 0 \\ -\sin(\eta) & 0 & \cos(\eta) \end{pmatrix} \begin{pmatrix} \frac{\sqrt{3}}{2}\sin(\mu) \\ \frac{1}{2}\sin(\mu) \\ \cos(\mu) \end{pmatrix} = \begin{pmatrix} \frac{\sqrt{3}}{2}\sin(\mu)\cos(\eta) + \cos(\mu)\sin(\eta) \\ \frac{1}{2}\sin(\mu) \\ -\frac{\sqrt{3}}{2}\sin(\mu)\sin(\eta) + \cos(\mu)\cos(\eta) \end{pmatrix}$$

The direction of the microfibril angle after tilt and rotation is thus

$$\begin{aligned} \mathbf{b} &= \begin{pmatrix} \sin(\alpha) & \cos(\alpha) & 0 \\ -\cos(\alpha) & \sin(\alpha) & 0 \\ 0 & 0 & 1 \end{pmatrix} \begin{pmatrix} \frac{\sqrt{3}}{2}\sin(\mu)\cos(\eta) + \cos(\mu)\sin(\eta) \\ \frac{1}{2}\sin(\mu) \\ -\frac{\sqrt{3}}{2}\sin(\mu)\sin(\eta) + \cos(\mu)\cos(\eta) \end{pmatrix} \\ &= \begin{pmatrix} \frac{\sqrt{3}}{2}\sin(\alpha)\sin(\mu)\cos(\eta) + \sin(\alpha)\cos(\mu)\sin(\eta) + \frac{1}{2}\cos(\alpha)\sin(\mu) \\ -\frac{\sqrt{3}}{2}\cos(\alpha)\sin(\mu)\cos(\eta) - \cos(\alpha)\cos(\mu)\sin(\eta) + \frac{1}{2}\sin(\alpha)\sin(\mu) \\ -\frac{\sqrt{3}}{2}\sin(\mu)\sin(\eta) + \cos(\mu)\cos(\eta) \end{pmatrix} \end{aligned} \tag{19}$$

11.2 The Six Equations

There are two conditions that a 002 reflecting plane must meet to reflect a beam coming in along the x axis. First, $\mathbf{b}$ is in the 002 crystallographic planes of the cellulose crystals associated with the microfibrils so the normal, $\mathbf{p}$, to the 002 plane that succeeds in reflecting the beam must be perpendicular to $\mathbf{b}$. Second (the Bragg condition), the normal to the 002 reflecting plane must make a $90 - \theta$ angle to the x axis, where θ is the Bragg angle for the X-ray wavelength being used. Given these two conditions, we want to be able to determine the location at which the reflected beam intersects the back plane of the X-ray apparatus.

The second condition gives us

$$p_1 = \begin{pmatrix} 1 \\ 0 \\ 0 \end{pmatrix} \cdot \mathbf{p} = \cos(90 - \theta) = \sin(\theta) \tag{20}$$

We also have

$$p_1^2 + p_2^2 + p_3^2 = 1 \tag{21}$$

Making use of Equations (20) and (21), we obtain

$$p_2^2 + p_3^2 = \cos^2(\theta) \tag{22}$$

The first condition and Equation (20) give us

$$\begin{pmatrix} \sin(\theta) \\ p_2 \\ p_3 \end{pmatrix} \cdot \mathbf{b} = 0 \tag{23}$$

Thus the solutions for (p_2, p_3) will be the 0, 1, or 2 points represented by the intersection of line (23) with circle (22). Circle (22) has radius $\cos(\theta)$ and a point on circle (22) has form $(\cos(\phi)\cos(\theta), \sin(\phi)\cos(\theta))$ for some angle ϕ. That is,

$$\begin{aligned} p_2 &= \cos(\phi)\cos(\theta) \\ p_3 &= \sin(\phi)\cos(\theta) \end{aligned} \tag{24}$$

From Equations (23) and (24) and Equations (14) – (19), after dividing by $\cos(\theta)$, we obtain six versions of the equation

$$d_1 + d_2 \times \cos(\phi) + d_3 \times \sin(\phi) = 0 \tag{25}$$

(In the next section we relate the ϕ in Equations (24) and (25) to the angle (counterclockwise from the east) of the bright spot on the back plane.)

For the **front** face, we have

$$\begin{aligned} d_1 &= (\sin(\alpha)\cos(\mu)\sin(\eta) + \cos(\alpha)\sin(\mu))\tan(\theta) \\ d_2 &= -\cos(\alpha)\cos(\mu)\sin(\eta) + \sin(\alpha)\sin(\mu) \\ d_3 &= \cos(\mu)\cos(\eta) \end{aligned} \tag{26}$$

For the **right 1** face, we have

$$\begin{aligned} d_1 &= \left(\frac{-\sqrt{3}}{2}\sin(\alpha)\sin(\mu)\cos(\eta) + \sin(\alpha)\cos(\mu)\sin(\eta) + \frac{1}{2}\cos(\alpha)\sin(\mu)\right)\tan(\theta) \\ d_2 &= \frac{\sqrt{3}}{2}\cos(\alpha)\sin(\mu)\cos(\eta) - \cos(\alpha)\cos(\mu)\sin(\eta) + \frac{1}{2}\sin(\alpha)\sin(\mu) \\ d_3 &= \frac{\sqrt{3}}{2}\sin(\mu)\sin(\eta) + \cos(\mu)\cos(\eta) \end{aligned} \tag{27}$$

For the **right 2** face, we have

$$\begin{aligned} d_1 &= \left(\frac{-\sqrt{3}}{2}\sin(\alpha)\sin(\mu)\cos(\eta) + \sin(\alpha)\cos(\mu)\sin(\eta) - \frac{1}{2}\cos(\alpha)\sin(\mu)\right)\tan(\theta) \\ d_2 &= \frac{\sqrt{3}}{2}\cos(\alpha)\sin(\mu)\cos(\eta) - \cos(\alpha)\cos(\mu)\sin(\eta) - \frac{1}{2}\sin(\alpha)\sin(\mu) \\ d_3 &= \frac{\sqrt{3}}{2}\sin(\mu)\sin(\eta) + \cos(\mu)\cos(\eta) \end{aligned} \tag{28}$$

For the **back** face, we have

$$\begin{aligned} d_1 &= (\sin(\alpha)\cos(\mu)\sin(\eta) - \cos(\alpha)\sin(\mu))\tan(\theta) \\ d_2 &= -\cos(\alpha)\cos(\mu)\sin(\eta) - \sin(\alpha)\sin(\mu) \\ d_3 &= \cos(\mu)\cos(\eta) \end{aligned} \tag{29}$$

For the **left 1** face, we have

$$\begin{aligned} d_1 &= \left(\frac{\sqrt{3}}{2}\sin(\alpha)\sin(\mu)\cos(\eta) + \sin(\alpha)\cos(\mu)\sin(\eta) - \frac{1}{2}\cos(\alpha)\sin(\mu)\right)\tan(\theta) \\ d_2 &= -\frac{\sqrt{3}}{2}\cos(\alpha)\sin(\mu)\cos(\eta) - \cos(\alpha)\cos(\mu)\sin(\eta) - \frac{1}{2}\sin(\alpha)\sin(\mu) \\ d_3 &= -\frac{\sqrt{3}}{2}\sin(\mu)\sin(\eta) + \cos(\mu)\cos(\eta) \end{aligned} \tag{30}$$

For the **left 2** face, we have

$$\begin{aligned} d_1 &= \left(\frac{\sqrt{3}}{2}\sin(\alpha)\sin(\mu)\cos(\eta) + \sin(\alpha)\cos(\mu)\sin(\eta) + \frac{1}{2}\cos(\alpha)\sin(\mu)\right)\tan(\theta) \\ d_2 &= -\frac{\sqrt{3}}{2}\cos(\alpha)\sin(\mu)\cos(\eta) - \cos(\alpha)\cos(\mu)\sin(\eta) + \frac{1}{2}\sin(\alpha)\sin(\mu) \\ d_3 &= -\frac{\sqrt{3}}{2}\sin(\mu)\sin(\eta) + \cos(\mu)\cos(\eta) \end{aligned} \tag{31}$$

Now in each of the six cases we can use Equation (25) to solve for ϕ. For $\phi \in [0, \pi]$, (25) yields

$$d_1 + d_2 x = -d_3\sqrt{1 - x^2} \tag{32}$$

for $x = \cos(\phi)$. Squaring both sides and collecting terms, we obtain the quadratic equation

$$d_1^2 - d_3^2 + 2d_1 d_2 x + (d_2^2 + d_3^2)x^2 = 0$$

We then find the $\phi \in [0, \pi]$ for which $\cos(\phi) = x_{\text{sol}}$ where x_{sol} is a solution to the quadratic equation. Of course, for this to yield a ϕ there must be a solution to the quadratic equation and this solution must lie in $[-1, 1]$.

For $\phi \in [-\pi, 0]$, (25) yields

$$d_1 + d_2 x = d_3\sqrt{1 - x^2} \tag{33}$$

and the resulting quadratic equation is unchanged. In our computer program we check the (at most) two solutions for the $\phi \in [0, \pi]$ case against Equation (32) and the (at most) two solutions for the $\phi \in [-\pi, 0]$ case against Equation (33). If the total number of solutions is greater than two, then the program terminates with an error messsage. Note, however, that it is possible for there to be zero solutions. For example, if the MFA is 50 degrees, rotation is 0 degrees, and the tilt is 30 degrees, there will be no solutions for the left face (no plane containing the microfibril will be at a 11.35 degree angle to the incoming X-ray beam).

11.3 Relation between ϕ and the Angle (Counterclockwise from the East) of the Bright Spot on the Back Plane

Let us now consider the issue of where the reflected beam intersects the back plane. We know that the beam comes in along the x axis and reflects off a plane whose normal is given by Equations (20) and (24). Consider now a canonical situation in which a beam reflects off a plane with normal (0,0,1) (the z axis). In this case the direction vector of the reflected beam is the same as the direction vector of the incident beam except that the sign of the z coordinate is reversed.

To make use of this result, we first find the transform that takes the $\mathbf{p}$ vector to the z vector. This requires a rotation of $90 - \phi$ degrees of the z axis towards the y axis (to bring the z axis in line with the projection of $\mathbf{p}$ onto the y, z plane), followed by a rotation of θ degrees of the z axis towards the x axis (to bring the z axis into line with $\mathbf{p}$). These two rotations can be represented by the transform

$$T \equiv \begin{pmatrix} \cos(\theta) & 0 & -\sin(\theta) \\ 0 & 1 & 0 \\ \sin(\theta) & 0 & \cos(\theta) \end{pmatrix} \begin{pmatrix} 1 & 0 & 0 \\ 0 & \sin(\phi) & -\cos(\phi) \\ 0 & \cos(\phi) & \sin(\phi) \end{pmatrix}$$

One can check that

$$T(\mathbf{p}) = T \cdot \begin{pmatrix} \sin(\theta) \\ \cos(\phi)\cos(\theta) \\ \sin(\phi)\cos(\theta) \end{pmatrix} = \begin{pmatrix} 0 \\ 0 \\ 1 \end{pmatrix}$$

Now in the original coordinate system, the X-ray incident direction is

$$\begin{pmatrix} -1 \\ 0 \\ 0 \end{pmatrix}$$

In the coordinate system in which the $\mathbf{p}$ vector has been transformed to the z vector, this incident direction becomes

$$T \cdot \begin{pmatrix} -1 \\ 0 \\ 0 \end{pmatrix} = \begin{pmatrix} -\cos(\theta) \\ 0 \\ -\sin(\theta) \end{pmatrix}$$

so the beam reflects off in the

$$\begin{pmatrix} -\cos(\theta) \\ 0 \\ \sin(\theta) \end{pmatrix}$$

direction. Transformed back into the original coordinate system, this direction vector is

$$\begin{pmatrix} 1 & 0 & 0 \\ 0 & \sin(\phi) & -\cos(\phi) \\ 0 & \cos(\phi) & \sin(\phi) \end{pmatrix}^{-1} \begin{pmatrix} \cos(\theta) & 0 & -\sin(\theta) \\ 0 & 1 & 0 \\ \sin(\theta) & 0 & \cos(\theta) \end{pmatrix}^{-1} \begin{pmatrix} -\cos(\theta) \\ 0 \\ \sin(\theta) \end{pmatrix}$$

$$= \begin{pmatrix} -\cos(2\theta) \\ \cos(\phi)\sin(2\theta) \\ \sin(\phi)\sin(2\theta) \end{pmatrix}$$

We extend a beam in this direction to its intersection with a back plane that is perpendicular to the x axis and x_0 units behind the specimen by multiplying by a factor of $x_0/\cos(2\theta)$. Thus the

beam intersects the back plane at the point

$$\begin{pmatrix} -x_0 \\ \cos(\phi)\sin(2\theta)x_0/(\cos(2\theta)) \\ \sin(\phi)\sin(2\theta)x_0/(\cos(2\theta)) \end{pmatrix} = \begin{pmatrix} -x_0 \\ \cos(\phi)\tan(2\theta)x_0 \\ \sin(\phi)\tan(2\theta)x_0 \end{pmatrix}$$

Looking face on at the back plane, this is the point that is on the circle of radius $\tan(2\theta)x_0$ (the "2θ circle") and ϕ degrees in a counterclockwise direction from the y axis. So a ϕ that is a solution to Equation (25) is also the angle (counterclockwise from the east) of a point of maximum X-ray intensity.

12 Appendix B — The Simulation Tables

We describe Tables 1 through 50 in this appendix. The tables can be viewed and/or downloaded at `http://www1.fpl.fs.fed.us/varapp_tables.html`.

Tables 1 – 25 are associated with cells of rectangular cross section. Tables 26 – 50 are the corresponding tables for cells of hexagonal cross section.

For cells of rectangular cross section, Tables 1 through 5 list the 8 bright spot locations for tilts of 0, 10, 20, 30, and 40 degrees, rotations of 0, 15, 30, 45, 60, 75, and 90 degrees, and MFAs of 2, 10, 20, 30, 40, 50, and 55 degrees. Tables 26 through 30 list the corresponding information for the 12 bright spot locations generated by a hexagonal cross section. (In Appendices D – G we establish symmetries that permit us reasonably to restrict our simulation to the tilts and rotations considered.) These tables also list the corresponding mean bright spot locations, $\bar{\phi}$, for each of the two half-profiles. (If there is no tilt, these means are 0 degrees and 180 degrees.)

In the rectangular case, plots of bright spot locations for 0 and 15 degree tilts, 0, 10, 20, 22.5, 30, 40, 45, 50, 60, 67.5, 70, 80, and 90 degree rotations, and 10, 20, 30, 40, 50, and 60 degree MFAs are displayed in Figures 6 through 18 and 20 through 32 of Verrill *et al.* (2006).

In the hexagonal case, plots of bright spots for 0 and 20 degree tilts, 0, 15, 30, 45, 60, 75, and 90 degree rotations, and 10, 20, 30, 40, 50, and 55 degree MFAs appear as Figures 40 through 53 of the current paper.

Tables 6 – 25 and 31 – 50 are associated with the relation

$$S^2 = \sum_{j=1}^{J}(n_j - 1)s_j^2/n_{\text{tot}} + \sum_{j=1}^{J} n_j \left(\bar{y}_{\cdot j} - \bar{y}_{\cdot\cdot}\right)^2 /n_{\text{tot}} \tag{34}$$

that we developed in Section 5. Here

$$s_j^2 \equiv \sum_{i=1}^{n_j} \left(y_{ij} - \bar{y}_{\cdot j}\right)^2 /(n_j - 1)$$

is the standard deviation of the jth peak.

Recall that in our simulation we draw MFAs from a Gaussian distribution centered at μ with standard deviation given by $\sigma = \sqrt{(\mu/3)^2 + 6^2}$. The ith draw leads to bright spot locations $y_{ij}, j = 1, \ldots, J$ corresponding to $\phi_j, j = 1, \ldots, J$.

Tables 6 – 10 and 31 – 35 provide three estimates of the δ_j's — our simulation estimates (the s_j^2's), our "analytic" estimates (see Appendix C), and the estimates based on Evans's (1999) equation [14]. The tables provide these estimates for both the left and the right half-profiles. In both the rectangular and hexagonal cases, the tables demonstrate that Evans's equation [14] yields poor estimates of the δ_j's (even in the no-tilt, no-rotation case).

Tables 11 – 15 and 36 – 40 compare our $\sum_{j=1}^{J}(n_j-1)s_j^2/n_{\text{tot}}$ value with Evans's $\sigma^2/\cos(\mu)$, which is his approximation to his $\sum_{j=1}^{J}\delta_j^2/J$. Given the differences between our s_j^2's and the δ_j^2's from Evans's equation [14], we would expect significant differences between the $\sum_{j=1}^{J}(n_j-1)s_j^2/n_{\text{tot}}$ and $\sigma^2/\cos(\mu)$ values. A glance at the tables makes clear that the differences are indeed significant. It should also be noted that the Evans value, $\sum_{j=1}^{J}\delta_j^2/J$, does not depend on the half-profile, while, in fact, as can be seen from the tables, for non-zero rotations the mean within peak variability can differ significantly between the left and right half-profiles.

Tables 16 – 20 and 41 – 45 compare our $\sum_{j=1}^{J} n_j\left(\bar{y}_{\cdot j}-\bar{y}_{\cdot\cdot}\right)^2/n_{\text{tot}}$ (the SS1 column in the table) with Evans's $\mu^2/2$. We also compare $\sum_{j=1}^{J}(\phi_j-\bar{\phi})^2/J$ (the SS2 column), $\sum_{j=1}^{J}(\phi_j-0)^2/J$ (the SS3 column, left half-profile rows), and $\sum_{j=1}^{J}(\phi_j-\pi)^2/J$ (the SS3 column, right half-profile rows) with $\mu^2/2$. The Evans result consistently underestimates the other measures of between peak variability. Again, the Evans value does not depend on the half-profile, while, in fact, for non-zero rotations, the between peak variability can differ significantly between the left and right half-profiles.

Tables 21 – 25 and 46 – 50 list the biases in the variance approach estimate of MFA as a function of tilt, rotation, MFA, half-profile, and cell cross section. Plots of a subset of these results appear as Figures 2 through 29. It is important to note that the figures plot the biases in the case in which both half-profiles are used to estimate the MFA. If only a single half-profile is used, the biases can be significantly inflated (or deflated) depending upon the tilt, rotation, MFA, cross section, and half-profile. For example, from Table 21 we can see that for 0 tilt, 15 degree rotation, and a rectangular cross section, when the variabilities of the two half-profiles are averaged, the theoretical biases for MFAs 40, 50, and 55 are 1.2, 4.9, and 8.1. However, when only the variance of the left half-profile is used in the estimate, the corresponding biases are 3.2, 9.9, and 15.2.

One feature of these tables needs to be explained. The tables contain two super-columns labeled "theoretical" and "practical". The "practical" columns were calculated by assuming that the intensity between -90 degrees and 90 degrees on the back plane corresponds to the left half-profile and the intensity between 90 degrees and 270 degrees on the back plane corresponds to the right half-profile. (Here the 0 degree direction on the back plane is East and the positive azimuthal direction is counterclockwise.) The "theoretical" columns were obtained by determining the four (or six) ϕ_j's that corresponded to each of the two half-profiles, and then allocating the two bright points from a face in a draw to the appropriate peaks and thus the appropriate half-profiles. For small tilts and MFAs, the two approaches will yield the same results. However, for larger tilts and MFAs, broadened bright spots from an MFA draw can appear in the "wrong" half of the back plane. See, for example, Figure 53. For a tilt of 20 degrees and an MFA of 50, it is clear that the broadened peak of the bright spot that is at an angle of -70.7 degrees would be expected to be broadened in such a manner that part of its peak would lie below -90 degrees. For the "practical" estimate of S^2 the half-profile is truncated at -90 degrees (and at $+90$ degrees). For the "theoretical" estimate, the half-profile is not truncated.

We note a problem with the current implementation of our simulation. For very large MFAs (50 or 55 degrees in our simulation), it is possible for misallocations to be made. Our algorithm compares

$$ss_1 = (y_1-\phi_L)^2+(y_2-\phi_R)^2$$

and

$$ss_2 = (y_1-\phi_R)^2+(y_2-\phi_L)^2$$

where ϕ_L and ϕ_R are the unbroadened left and right half-profile bright spots for a particular face, and y_1, y_2 are the bright spots associated with that face for a particular draw of a broadened MFA.

If $ss_1 < ss_2$, our algorithm allocates y_1 to the ϕ_L peak and y_2 to the ϕ_R peak. If $ss_1 > ss_2$, it allocates y_1 to the ϕ_R peak and y_2 to the ϕ_L peak. This algorithm yields simulation s_j^2's that match analytic estimates of peak variabilities for smaller (and many larger) MFAs. It yields theoretical bias estimates that match practical bias estimates for smaller MFAs. However, for the highest MFA values, it yields larger bias estimates than does the practical approach. We expect that the practical approach will underestimate the true S^2 for larger MFAs as it truncates at -90 and 90 degrees (or, for the right half-profile, 90 and 270 degrees). Thus it is reasonable that the theoretical estimates of MFA will be larger than the practical for larger MFAs. However, it is also possible that, for larger MFAs, some of the positive bias of the theoretical MFA estimates is due to misallocations.

13 Appendix C — The Partial Derivative Approach to Estimating the Bright Spot Broadening Standard Deviations

As established in Appendix A, the defining equation for azimuthal angles is

$$d_1 + d_2\cos(\phi) + d_3\sin(\phi) = 0 \tag{35}$$

where ϕ is the azimuthal angle of a bright spot on the back plane (read counterclockwise from the east), and d_1, d_2, d_3 are known values that depend on the Bragg angle, MFA, cell face, rotation, and tilt.

Taking partial derivatives of both sides of this equation with respect to MFA we obtain

$$\frac{\partial d_1}{\partial \mu} + \frac{\partial d_2}{\partial \mu}\cos(\phi) + d_2(-\sin(\phi))\frac{\partial \phi}{\partial \mu} + \frac{\partial d_3}{\partial \mu}\sin(\phi) + d_3\cos(\phi)\frac{\partial \phi}{\partial \mu} = 0$$

or, solving for $\frac{\partial \phi}{\partial \mu}$,

$$\frac{\partial \phi}{\partial \mu} = \left(\frac{\partial d_1}{\partial \mu} + \frac{\partial d_2}{\partial \mu}\cos(\phi) + \frac{\partial d_3}{\partial \mu}\sin(\phi)\right) / \left(d_2\sin(\phi) - d_3\cos(\phi)\right) \tag{36}$$

Next, we have the Taylor series approximation

$$\phi(\mu) \approx \phi(\mu_0) + \frac{\partial \phi(\mu_0)}{\partial \mu} \times (\mu - \mu_0)$$

Assuming that μ is a random variable with mean μ_0 and standard deviation σ, this implies that

$$\mathrm{Var}(\phi(\mu)) \approx \left(\frac{\partial \phi(\mu_0)}{\partial \mu}\right)^2 \times \sigma^2 \tag{37}$$

Results (36) and (37) permit us to obtain an analytic estimate of the standard deviation associated with a bright spot.

To complete this approach, we need expressions for the partial derivatives of the four or six faces of the wood cell:

13.1 Rectangular Cross Section

13.1.1 Front Face

From result (26) we have

$$\frac{\partial d_1}{\partial \mu} = (-\sin(\alpha)\sin(\mu)\sin(\eta) + \cos(\alpha)\cos(\mu))\tan(\theta)$$

$$\begin{aligned}\frac{\partial d_2}{\partial \mu} &= \cos(\alpha)\sin(\mu)\sin(\eta) + \sin(\alpha)\cos(\mu) \\ \frac{\partial d_3}{\partial \mu} &= -\sin(\mu)\cos(\eta)\end{aligned} \tag{38}$$

13.1.2 Right Face

In Verrill *et al.* (2006) we established that for the right face,

$$\begin{aligned}d_1 &= -\sin(\alpha)\sin(\mu-\eta)\tan(\theta) \\ d_2 &= \cos(\alpha)\sin(\mu-\eta) \\ d_3 &= \cos(\mu-\eta)\end{aligned} \tag{39}$$

Thus,

$$\begin{aligned}\frac{\partial d_1}{\partial \mu} &= -\sin(\alpha)\cos(\mu-\eta)\tan(\theta) \\ \frac{\partial d_2}{\partial \mu} &= \cos(\alpha)\cos(\mu-\eta) \\ \frac{\partial d_3}{\partial \mu} &= -\sin(\mu-\eta)\end{aligned} \tag{40}$$

13.1.3 Back Face

From result (29) we have

$$\begin{aligned}\frac{\partial d_1}{\partial \mu} &= (-\sin(\alpha)\sin(\mu)\sin(\eta) - \cos(\alpha)\cos(\mu))\tan(\theta) \\ \frac{\partial d_2}{\partial \mu} &= \cos(\alpha)\sin(\mu)\sin(\eta) - \sin(\alpha)\cos(\mu) \\ \frac{\partial d_3}{\partial \mu} &= -\sin(\mu)\cos(\eta)\end{aligned} \tag{41}$$

13.1.4 Left Face

In Verrill *et al.* (2006) we established that for the left face,

$$\begin{aligned}d_1 &= \sin(\alpha)\sin(\mu+\eta)\tan(\theta) \\ d_2 &= -\cos(\alpha)\sin(\mu+\eta) \\ d_3 &= \cos(\mu+\eta)\end{aligned} \tag{42}$$

Thus,

$$\begin{aligned}\frac{\partial d_1}{\partial \mu} &= \sin(\alpha)\cos(\mu+\eta)\tan(\theta) \\ \frac{\partial d_2}{\partial \mu} &= -\cos(\alpha)\cos(\mu+\eta) \\ \frac{\partial d_3}{\partial \mu} &= -\sin(\mu+\eta)\end{aligned} \tag{43}$$

13.2 Hexagonal Cross Section

13.2.1 Front Face

See result (38) above.

13.2.2 Right 1 Face

From result (27) we have

$$\begin{aligned}
\frac{\partial d_1}{\partial \mu} &= \left(\frac{-\sqrt{3}}{2} \sin(\alpha)\cos(\mu)\cos(\eta) - \sin(\alpha)\sin(\mu)\sin(\eta) + \frac{1}{2}\cos(\alpha)\cos(\mu) \right) \tan(\theta) \\
\frac{\partial d_2}{\partial \mu} &= \frac{\sqrt{3}}{2} \cos(\alpha)\cos(\mu)\cos(\eta) + \cos(\alpha)\sin(\mu)\sin(\eta) + \frac{1}{2}\sin(\alpha)\cos(\mu) \qquad (44) \\
\frac{\partial d_3}{\partial \mu} &= \frac{\sqrt{3}}{2} \cos(\mu)\sin(\eta) - \sin(\mu)\cos(\eta)
\end{aligned}$$

13.2.3 Right 2 Face

From result (28) we have

$$\begin{aligned}
\frac{\partial d_1}{\partial \mu} &= \left(\frac{-\sqrt{3}}{2} \sin(\alpha)\cos(\mu)\cos(\eta) - \sin(\alpha)\sin(\mu)\sin(\eta) - \frac{1}{2}\cos(\alpha)\cos(\mu) \right) \tan(\theta) \\
\frac{\partial d_2}{\partial \mu} &= \frac{\sqrt{3}}{2} \cos(\alpha)\cos(\mu)\cos(\eta) + \cos(\alpha)\sin(\mu)\sin(\eta) - \frac{1}{2}\sin(\alpha)\cos(\mu) \qquad (45) \\
\frac{\partial d_3}{\partial \mu} &= \frac{\sqrt{3}}{2} \cos(\mu)\sin(\eta) - \sin(\mu)\cos(\eta)
\end{aligned}$$

13.2.4 Back Face

See result (41) above.

13.2.5 Left 1 Face

From result (30) we have

$$\begin{aligned}
\frac{\partial d_1}{\partial \mu} &= \left(\frac{\sqrt{3}}{2} \sin(\alpha)\cos(\mu)\cos(\eta) - \sin(\alpha)\sin(\mu)\sin(\eta) - \frac{1}{2}\cos(\alpha)\cos(\mu) \right) \tan(\theta) \\
\frac{\partial d_2}{\partial \mu} &= -\frac{\sqrt{3}}{2} \cos(\alpha)\cos(\mu)\cos(\eta) + \cos(\alpha)\sin(\mu)\sin(\eta) - \frac{1}{2}\sin(\alpha)\cos(\mu) \qquad (46) \\
\frac{\partial d_3}{\partial \mu} &= -\frac{\sqrt{3}}{2} \cos(\mu)\sin(\eta) - \sin(\mu)\cos(\eta)
\end{aligned}$$

13.2.6 Left 2 Face

From result (31) we have

$$\frac{\partial d_1}{\partial \mu} = \left(\frac{\sqrt{3}}{2} \sin(\alpha)\cos(\mu)\cos(\eta) - \sin(\alpha)\sin(\mu)\sin(\eta) + \frac{1}{2}\cos(\alpha)\cos(\mu) \right) \tan(\theta)$$

$$\frac{\partial d_2}{\partial \mu} = -\frac{\sqrt{3}}{2}\cos(\alpha)\cos(\mu)\cos(\eta) + \cos(\alpha)\sin(\mu)\sin(\eta) + \frac{1}{2}\sin(\alpha)\cos(\mu) \quad (47)$$

$$\frac{\partial d_3}{\partial \mu} = -\frac{\sqrt{3}}{2}\cos(\mu)\sin(\eta) - \sin(\mu)\cos(\eta)$$

14 Appendix D — The Effects of a Change in Tilt Sign or in Rotation Sign on the Pattern of Eight Bright Spots Associated with a Rectangular Cross Section

In appendix B of Verrill *et al.* (2006), we established the following eight claims.

14.1 A Change in Tilt Sign

Given a change in tilt sign, bright spot locations are reflected across the horizontal west to east line (see Figure 38). Also front, back IDs are exchanged, and right, left IDs are exchanged.

This effect is embodied in the following four claims.

Claim 1

If ϕ is a solution for a front bright spot under tilt η, then $-\phi$ is a solution for a back bright spot under tilt $-\eta$.

Claim 2

If ϕ is a solution for a back bright spot under tilt η, then $-\phi$ is a solution for a front bright spot under tilt $-\eta$.

Claim 3

If ϕ is a solution for a right bright spot under tilt η, then $-\phi$ is a solution for a left bright spot under tilt $-\eta$.

Claim 4

If ϕ is a solution for a left bright spot under tilt η, then $-\phi$ is a solution for a right bright spot under tilt $-\eta$.

14.2 A Change in Rotation Sign

Given a change in rotation sign, bright spot locations are reflected across the vertical south to north line (see Figure 38). Also front, back IDs are exchanged. Right, left IDs remain unchanged.

This effect is embodied in the following four claims.

Claim 5

If $\pi/2 - \beta$ is a solution for a front bright spot under rotation rot, then $\pi/2 + \beta$ is a solution for a back bright spot under rotation $-$rot.

Claim 6

If $\pi/2 - \beta$ is a solution for a back bright spot under rotation rot, then $\pi/2 + \beta$ is a solution for a front bright spot under rotation $-$rot.

Claim 7

If $\pi/2 - \beta$ is a solution for a right bright spot under rotation rot, then $\pi/2 + \beta$ is a solution for a right bright spot under rotation $-$rot.

Claim 8

If $\pi/2 - \beta$ is a solution for a left bright spot under rotation rot, then $\pi/2 + \beta$ is a solution for a left bright spot under rotation $-$rot.

15 Appendix E — The Effects of a Change in Tilt Sign or in Rotation Sign on the Pattern of 12 Bright Spots Associated with a Hexagonal Cross Section

15.1 A Change in Tilt Sign

Given a change in tilt sign, bright spot locations are reflected across the horizontal west to east line (see Figure 38). Also front and back IDs are exchanged, right 1 and left 1 IDs are exchanged, and right 2 and left 2 IDs are exchanged.

This effect is embodied in the following six claims.

Claim 9

If ϕ is a solution for a front bright spot under tilt η, then $-\phi$ is a solution for a back bright spot under tilt $-\eta$.

Claim 10

If ϕ is a solution for a back bright spot under tilt η, then $-\phi$ is a solution for a front bright spot under tilt $-\eta$.

Claim 11

If ϕ is a solution for a right 1 bright spot under tilt η, then $-\phi$ is a solution for a left 1 bright spot under tilt $-\eta$.

Claim 12

If ϕ is a solution for a left 1 bright spot under tilt η, then $-\phi$ is a solution for a right 1 bright spot under tilt $-\eta$.

Claim 13

If ϕ is a solution for a right 2 bright spot under tilt η, then $-\phi$ is a solution for a left 2 bright spot under tilt $-\eta$.

Claim 14

If ϕ is a solution for a left 2 bright spot under tilt η, then $-\phi$ is a solution for a right 2 bright spot under tilt $-\eta$.

Equations (26) – (31) can be used in a straightforward manner to establish these claims. Here, for the purposes of illustration, we establish Claim 11.

From Equations (25) and (27) we have

$$\begin{aligned}\left(\frac{-\sqrt{3}}{2}\sin(\alpha)\sin(\mu)\cos(\eta)+\sin(\alpha)\cos(\mu)\sin(\eta)+\frac{1}{2}\cos(\alpha)\sin(\mu)\right)\tan(\theta) \quad &+\\ \left(\frac{\sqrt{3}}{2}\cos(\alpha)\sin(\mu)\cos(\eta)-\cos(\alpha)\cos(\mu)\sin(\eta)+\frac{1}{2}\sin(\alpha)\sin(\mu)\right)\cos(\phi) \quad &+\\ \left(\frac{\sqrt{3}}{2}\sin(\mu)\sin(\eta)+\cos(\mu)\cos(\eta)\right)\sin(\phi) \quad &= \quad 0\end{aligned}$$

Multiplying this equation by -1 we obtain

$$\begin{aligned}\left(\frac{\sqrt{3}}{2}\sin(\alpha)\sin(\mu)\cos(\eta)-\sin(\alpha)\cos(\mu)\sin(\eta)-\frac{1}{2}\cos(\alpha)\sin(\mu)\right)\tan(\theta) \quad &+\\ \left(-\frac{\sqrt{3}}{2}\cos(\alpha)\sin(\mu)\cos(\eta)+\cos(\alpha)\cos(\mu)\sin(\eta)-\frac{1}{2}\sin(\alpha)\sin(\mu)\right)\cos(\phi) \quad &+\end{aligned}$$

$$\left(-\frac{\sqrt{3}}{2}\sin(\mu)\sin(\eta)-\cos(\mu)\cos(\eta)\right)\sin(\phi) \quad = \quad 0$$

or

$$\left(\frac{\sqrt{3}}{2}\sin(\alpha)\sin(\mu)\cos(-\eta)+\sin(\alpha)\cos(\mu)\sin(-\eta)-\frac{1}{2}\cos(\alpha)\sin(\mu)\right)\tan(\theta) \quad +$$
$$\left(-\frac{\sqrt{3}}{2}\cos(\alpha)\sin(\mu)\cos(-\eta)-\cos(\alpha)\cos(\mu)\sin(-\eta)-\frac{1}{2}\sin(\alpha)\sin(\mu)\right)\cos(-\phi) \quad +$$
$$\left(-\frac{\sqrt{3}}{2}\sin(\mu)\sin(-\eta)+\cos(\mu)\cos(-\eta)\right)\sin(-\phi) \quad = \quad 0$$

which is what we needed to establish (see Equations (25) and (30)).

15.2 A Change in Rotation Sign

Given a change in rotation sign, bright spot locations are reflected across the vertical south to north line (see Figure 38). Also front back IDs are exchanged, right 1 and right 2 IDs are exchanged, and left 1 and left 2 IDs are exchanged.

This effect is embodied in the following six claims.

Claim 15

If $\pi/2-\beta$ is a solution for a front bright spot under rotation rot, then $\pi/2+\beta$ is a solution for a back bright spot under rotation $-$rot.

Claim 16

If $\pi/2-\beta$ is a solution for a back bright spot under rotation rot, then $\pi/2+\beta$ is a solution for a front bright spot under rotation $-$rot.

Claim 17

If $\pi/2-\beta$ is a solution for a right 1 bright spot under rotation rot, then $\pi/2+\beta$ is a solution for a right 2 bright spot under rotation $-$rot.

Claim 18

If $\pi/2-\beta$ is a solution for a right 2 bright spot under rotation rot, then $\pi/2+\beta$ is a solution for a right 1 bright spot under rotation $-$rot.

Claim 19

If $\pi/2-\beta$ is a solution for a left 1 bright spot under rotation rot, then $\pi/2+\beta$ is a solution for a left 2 bright spot under rotation $-$rot.

Claim 20

If $\pi/2-\beta$ is a solution for a left 2 bright spot under rotation rot, then $\pi/2+\beta$ is a solution for a left 1 bright spot under rotation $-$rot.

Equations (26) – (31) can be used in a straightforward manner to establish these claims. Here, for the purposes of illustration, we establish Claim 17.

From Equations (25) and (27) we have (recall that $\alpha=\pi/2+\text{rot}$ so $\cos(\alpha)=-\sin(\text{rot})$ and $\sin(\alpha)=\cos(\text{rot})$)

$$\left(\frac{-\sqrt{3}}{2}\cos(\text{rot})\sin(\mu)\cos(\eta)+\cos(\text{rot})\cos(\mu)\sin(\eta)-\frac{1}{2}\sin(\text{rot})\sin(\mu)\right)\tan(\theta) \quad +$$

$$\left(-\frac{\sqrt{3}}{2}\sin(\text{rot})\sin(\mu)\cos(\eta)+\sin(\text{rot})\cos(\mu)\sin(\eta)+\frac{1}{2}\cos(\text{rot})\sin(\mu)\right)\sin(\beta) \quad + \tag{48}$$

$$\left(\frac{\sqrt{3}}{2}\sin(\mu)\sin(\eta)+\cos(\mu)\cos(\eta)\right)\cos(\beta) \quad = \quad 0$$

or

$$\left(\frac{-\sqrt{3}}{2}\cos(-\text{rot})\sin(\mu)\cos(\eta)+\cos(-\text{rot})\cos(\mu)\sin(\eta)+\frac{1}{2}\sin(-\text{rot})\sin(\mu)\right)\tan(\theta) \quad +$$

$$\left(-\frac{\sqrt{3}}{2}\sin(-\text{rot})\sin(\mu)\cos(\eta)+\sin(-\text{rot})\cos(\mu)\sin(\eta)-\frac{1}{2}\cos(-\text{rot})\sin(\mu)\right)\sin(-\beta) \quad +$$

$$\left(\frac{\sqrt{3}}{2}\sin(\mu)\sin(\eta)+\cos(\mu)\cos(\eta)\right)\cos(\beta) \quad = \quad 0$$

which is what we needed to establish (see Equations (25) and (28)).

16 Appendix F — The Effect of a Rotation Greater Than $\pi/2$ on the Pattern of Eight Bright Spots Associated with a Rectangular Cross Section

We note that we use some potentially confusing notation here. In Appendix E, $\pi/2-\beta$ and $\pi/2+\beta$ were examples of ϕ (azimuthal) values. In this appendix, we use them to reference rotation values.

The bright spot locations for an η tilt and a $\pi/2+\beta$ rotation are the same as the bright spot locations for a $-\eta$ tilt and a $-(\pi/2-\beta)$ rotation. Labels, however, do change — front and back bright spots exchange labels, and right and left bright spots exchange labels.

This effect is embodied in the following four claims.

Claim 21

If ϕ is a solution for a front bright spot under rotation $\pi/2+\beta$ and tilt η, then ϕ is a solution for a back bright spot under rotation $-(\pi/2-\beta)$ and tilt $-\eta$.

Claim 22

If ϕ is a solution for a back bright spot under rotation $\pi/2+\beta$ and tilt η, then ϕ is a solution for a front bright spot under rotation $-(\pi/2-\beta)$ and tilt $-\eta$.

Claim 23

If ϕ is a solution for a right bright spot under rotation $\pi/2+\beta$ and tilt η, then ϕ is a solution for a left bright spot under rotation $-(\pi/2-\beta)$ and tilt $-\eta$.

Claim 24

If ϕ is a solution for a left bright spot under rotation $\pi/2+\beta$ and tilt η, then ϕ is a solution for a right bright spot under rotation $-(\pi/2-\beta)$ and tilt $-\eta$.

Equations (15) through (19) in Verrill *et al.* (2006) can be used in a straightforward manner to establish these claims. Here, for the purposes of illustration, we establish Claim 21.

From equations (15) and (16) in Verrill *et al.* (2006) (the α in equation (16) equals $\pi/2$+rotation) and the facts that $\cos(\pi/2+\beta)=-\sin(\beta)$ and $\sin(\pi/2+\beta)=\cos(\beta)$, we have

$$(-\sin(\beta)\cos(\mu)\sin(\eta)-\cos(\beta)\sin(\mu))\tan(\theta) \quad +$$

$$\begin{aligned}(\cos(\beta)\cos(\mu)\sin(\eta) - \sin(\beta)\sin(\mu))\cos(\phi) &+ \\ \cos(\mu)\cos(\eta)\sin(\phi) &= 0\end{aligned}$$

or

$$\begin{aligned}(\sin(\beta)\cos(\mu)\sin(-\eta) - \cos(\beta)\sin(\mu))\tan(\theta) &+ \\ (-\cos(\beta)\cos(\mu)\sin(-\eta) - \sin(\beta)\sin(\mu))\cos(\phi) &+ \\ \cos(\mu)\cos(-\eta)\sin(\phi) &= 0\end{aligned}$$

or

$$\begin{aligned}(\cos(-(\pi/2-\beta))\cos(\mu)\sin(-\eta) + \sin(-(\pi/2-\beta))\sin(\mu))\tan(\theta) &+ \\ (\sin(-(\pi/2-\beta))\cos(\mu)\sin(-\eta) - \cos(-(\pi/2-\beta))\sin(\mu))\cos(\phi) &+ \\ \cos(\mu)\cos(-\eta)\sin(\phi) &= 0\end{aligned}$$

which is what we needed to establish.

17 Appendix G — The Effect of a Rotation Greater Than $\pi/2$ on the Pattern of 12 Bright Spots Associated with a Hexagonal Cross Section

We note that we use some potentially confusing notation here. In Appendix E, $\pi/2-\beta$ and $\pi/2+\beta$ were examples of ϕ (azimuthal) values. In this appendix, we use them to reference rotation values.

The bright spot locations for an η tilt and a $\pi/2+\beta$ rotation are the same as the bright spot locations for a $-\eta$ tilt and a $-(\pi/2-\beta)$ rotation. Labels, however, do change — front and back bright spots exchange labels, right 1 and left 1 bright spots exchange labels, and right 2 and left 2 bright spots exchange labels.

This effect is embodied in the following six claims.

Claim 25

If ϕ is a solution for a front bright spot under rotation $\pi/2+\beta$ and tilt η, then ϕ is a solution for a back bright spot under rotation $-(\pi/2-\beta)$ and tilt $-\eta$.

Claim 26

If ϕ is a solution for a back bright spot under rotation $\pi/2+\beta$ and tilt η, then ϕ is a solution for a front bright spot under rotation $-(\pi/2-\beta)$ and tilt $-\eta$.

Claim 27

If ϕ is a solution for a right 1 bright spot under rotation $\pi/2+\beta$ and tilt η, then ϕ is a solution for a left 1 bright spot under rotation $-(\pi/2-\beta)$ and tilt $-\eta$.

Claim 28

If ϕ is a solution for a left 1 bright spot under rotation $\pi/2+\beta$ and tilt η, then ϕ is a solution for a right 1 bright spot under rotation $-(\pi/2-\beta)$ and tilt $-\eta$.

Claim 29

If ϕ is a solution for a right 2 bright spot under rotation $\pi/2+\beta$ and tilt η, then ϕ is a solution for a left 2 bright spot under rotation $-(\pi/2-\beta)$ and tilt $-\eta$.

Claim 30

If ϕ is a solution for a left 2 bright spot under rotation $\pi/2+\beta$ and tilt η, then ϕ is a solution for a right 2 bright spot under rotation $-(\pi/2-\beta)$ and tilt $-\eta$.

Equations (25) – (31) can be used in a straightforward manner to establish these claims. Here, for the purposes of illustration, we establish Claim 27.

From Equations (25) and (48) and the facts that $\cos(\pi/2+\beta) = -\sin(\beta)$ and $\sin(\pi/2+\beta) = \cos(\beta)$, we have

$$\begin{aligned}\left(\frac{-\sqrt{3}}{2}(-\sin(\beta))\sin(\mu)\cos(\eta) + (-\sin(\beta))\cos(\mu)\sin(\eta) - \frac{1}{2}\cos(\beta)\sin(\mu)\right)\tan(\theta) \quad &+ \\ \left(-\frac{\sqrt{3}}{2}\cos(\beta)\sin(\mu)\cos(\eta) + \cos(\beta)\cos(\mu)\sin(\eta) + \frac{1}{2}(-\sin(\beta))\sin(\mu)\right)\cos(\phi) \quad &+ \\ \left(\frac{\sqrt{3}}{2}\sin(\mu)\sin(\eta) + \cos(\mu)\cos(\eta)\right)\sin(\phi) \quad &= \quad 0\end{aligned}$$

or

$$\begin{aligned}\left(\frac{\sqrt{3}}{2}\sin(\beta)\sin(\mu)\cos(-\eta) + \sin(\beta)\cos(\mu)\sin(-\eta) - \frac{1}{2}\cos(\beta)\sin(\mu)\right)\tan(\theta) \quad &+ \\ \left(\frac{\sqrt{3}}{2}(-\cos(\beta))\sin(\mu)\cos(-\eta) + (-\cos(\beta))\cos(\mu)\sin(-\eta) - \frac{1}{2}\sin(\beta)\sin(\mu)\right)\cos(\phi) \quad &+ \\ \left(-\frac{\sqrt{3}}{2}\sin(\mu)\sin(-\eta) + \cos(\mu)\cos(-\eta)\right)\sin(\phi) \quad &= \quad 0\end{aligned}$$

or

$$\begin{aligned}\Bigg(\frac{\sqrt{3}}{2}\cos(-(\pi/2-\beta))\sin(\mu)\cos(-\eta) + \cos(-(\pi/2-\beta))\cos(\mu)\sin(-\eta) \\ + \frac{1}{2}\sin(-(\pi/2-\beta))\sin(\mu)\Bigg)\tan(\theta) \quad &+ \\ \Bigg(\frac{\sqrt{3}}{2}\sin(-(\pi/2-\beta))\sin(\mu)\cos(-\eta) + \sin(-(\pi/2-\beta))\cos(\mu)\sin(-\eta) \\ - \frac{1}{2}\cos(-(\pi/2-\beta))\sin(\mu)\Bigg)\cos(\phi) \quad &+ \\ \left(-\frac{\sqrt{3}}{2}\sin(\mu)\sin(-\eta) + \cos(\mu)\cos(-\eta)\right)\sin(\phi) \quad &= \quad 0\end{aligned}$$

which is what we needed to establish.

18 Appendix H — Natural Variability in Cell Rotation

Because cell rotation affects the bias in variance approach MFA estimates, we wanted to perform a quick first look at the *natural* cell rotations that might be present in a sample. (We distinguish these

rotations from rotations that might be introduced in the course of the collection and preparation of a sample. See Figure 33.) We do not claim that our results are definitive.

The cross sections of two professionally prepared slides of gymnosperms were used to obtain micrographs. One of these was prepared from the wood of *Pinus lambertiana* Dougl., the other from the wood of *Pinus monticola* Dougl. ex D. Don. Serial micrographs were taken across the entire cross sections in the radial direction; the micrographs were printed, then taped together to produce a magnified image of a continuous radial strip. A micrograph was also taken of a stage micrometer to be used to determine final magnification. The micrographs were taken on an Olympus BX40 microscope with a Spot 2 Insight Firewire camera, using 10× oculars and objectives, and the images were stored in a computer file prior to printing.

The *Pinus lambertiana* slide was 6.7 mm wide (radial direction) and contained nine latewood rings, two of which appeared to be false rings. The *Pinus monticola* slide was 7.6 mm wide (radial direction) and contained six latewood rings. Although the slides were taken from mature portions of the stems, there was enough ring curvature to determine pith and bark sides of the slides. Comparing the wood micrographs with the stage micrometer micrograph gave a final printed magnification of 2300×.

Each micrograph was saved as a .tif file, resulting in 9 files for *Pinus lambertiana* and 10 files for *Pinus monticola*. Each micrograph had a slight overlap from the previous one to maintain a continuous line. The .tif files were then opened with SigmaScan Pro® software (`http://systat.us/sc/index.html`). A 20 by 20 grid was electronically overlayed on each image and used as a reference to locate individual cells and to measure cell rotation angles. The SigmaScan Pro software also opens a blank spreadsheet when measurements begin.

For each of the 19 images, 25 grid locations on the 20 by 20 grid were randomly chosen. The cells at the 25 locations were measured. The angle reported is the angle between the pith-side tangential face of the cell and a ray in the image. The angle measurements were made by clicking on the pith-side tangential face, dragging the mouse to the ray in a direction parallel to the face, clicking on the ray, and then moving toward the pith on the ray and clicking a third time. The angle measurement was then automatically generated and recorded in the spreadsheet.

The majority of the measurements were made by clicking on the closest ray to the right of the cell (assuming that one is looking radially from the pith to the bark), but when the location of the ray did not allow this, the measurement was made to the left. In this case, the final angle was obtained by subtracting the physical measurement from 180 degrees.

Earlywood and latewood were noted, as well as the shape of the cell being measured. Spreadsheets and images with overlaid angles were saved for each .tif file.

Because the sampling was uniform with respect to area, earlywood cells were sampled much more frequently than latewood cells. We analyzed the earlywood and latewood cells separately.

SAS® (`http://www.sas.com`) was used to analyze the data. There was no trend across the micrograph from pith to bark. The sample sizes, pooled means and standard deviations, and minimum and maximum rotation values for the two species and the two types of cells are provided in Tables 56 and 57. For both species, the earlywood angle data was nonnormal. For *lambertiana*, the latewood angle data was nonnormal.

Species	sample size	mean	standard deviation	minimum	maximum
lambertiana	197	87.7	5.60	72.9	104.9
monticola	220	88.5	4.06	65.2	103.8

Table 56: Angles between the tangential faces of cells and rays, earlywood

Species	sample size	mean	standard deviation	minimum	maximum
lambertiana	23	89.4	2.49	81.2	94.7
monticola	23	86.8	7.39	71.0	101.2

Table 57: Angles between the tangential faces of cells and rays, latewood

We also recorded the cross-sectional shapes of the cells. These are reported in Tables 58 and 59. Note the high incidence of hexagonal and quadrilateral cross sections in the earlywood cells, and the high incidence of ellipses (ovals) in the latewood cells.

Species	quadrilateral	pentagon	hexagon	ellipse	other
lambertiana	84	30	71	12	0
monticola	96	10	86	27	1

Table 58: Earlywood cross-sectional shapes

Species	quadrilateral	pentagon	hexagon	ellipse	other
lambertiana	2	0	0	21	0
monticola	4	0	1	18	0

Table 59: Latewood cross-sectional shapes

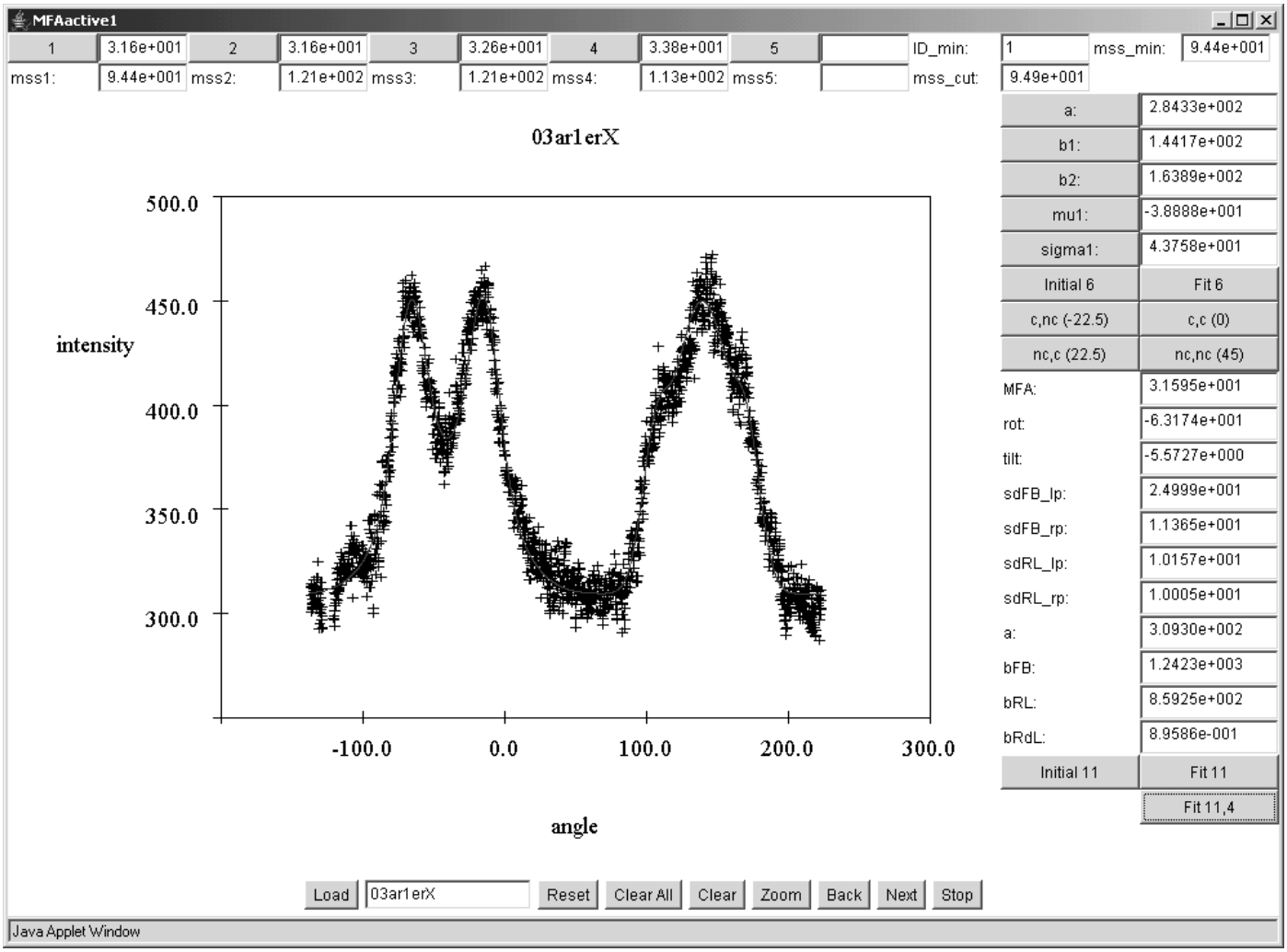

Figure 1: The double peaked half of the intensity profile corresponds (roughly) to the right half of the back plane. The single peaked half of the profile corresponds (roughly) to the left half of the back plane. In this case the X-ray apparatus was set up so that the minimum between the two halves of the profile would occur at 54.7 degrees rather than 90 degrees. For further explanation of the figure, see Figure 38 and the associated discussion in Verrill, Kretschmann, and Herian (2006).

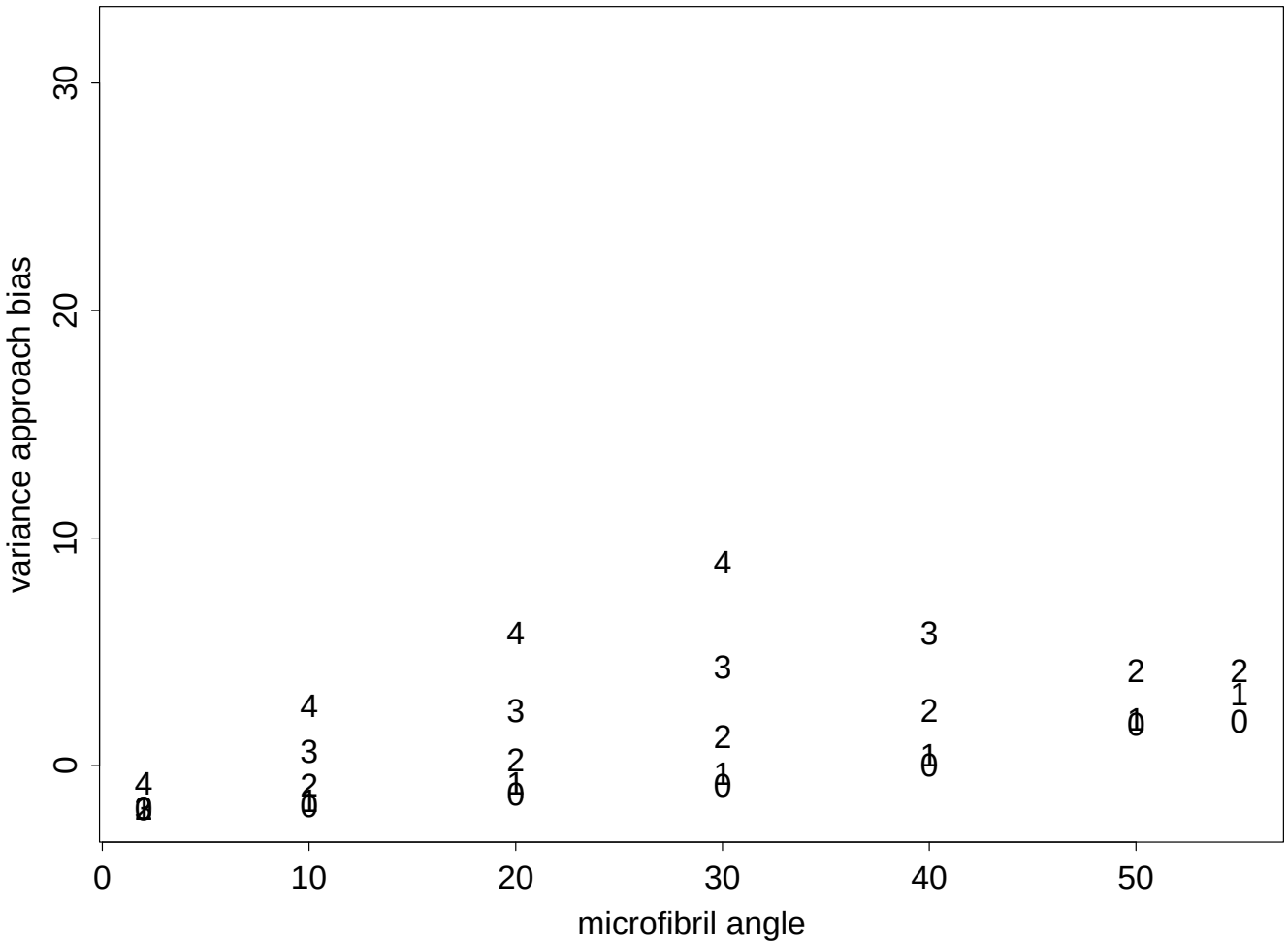

Figure 2: Variance approach bias versus true microfibril angle. **0 degree rotation**. 0 - 0 degree tilt. 1 - 10 degree tilt. 2 - 20 degree tilt. 3 - 30 degree tilt. 4 - 40 degree tilt. Theoretical biases. Profiles combined. Rectangular cell cross-section. Values are missing for 30 degree tilt, 50 and 55 degree MFAs, and 40 degree tilt, 40, 50, and 55 degree MFAs because there are no reflections from the left face in these cases.

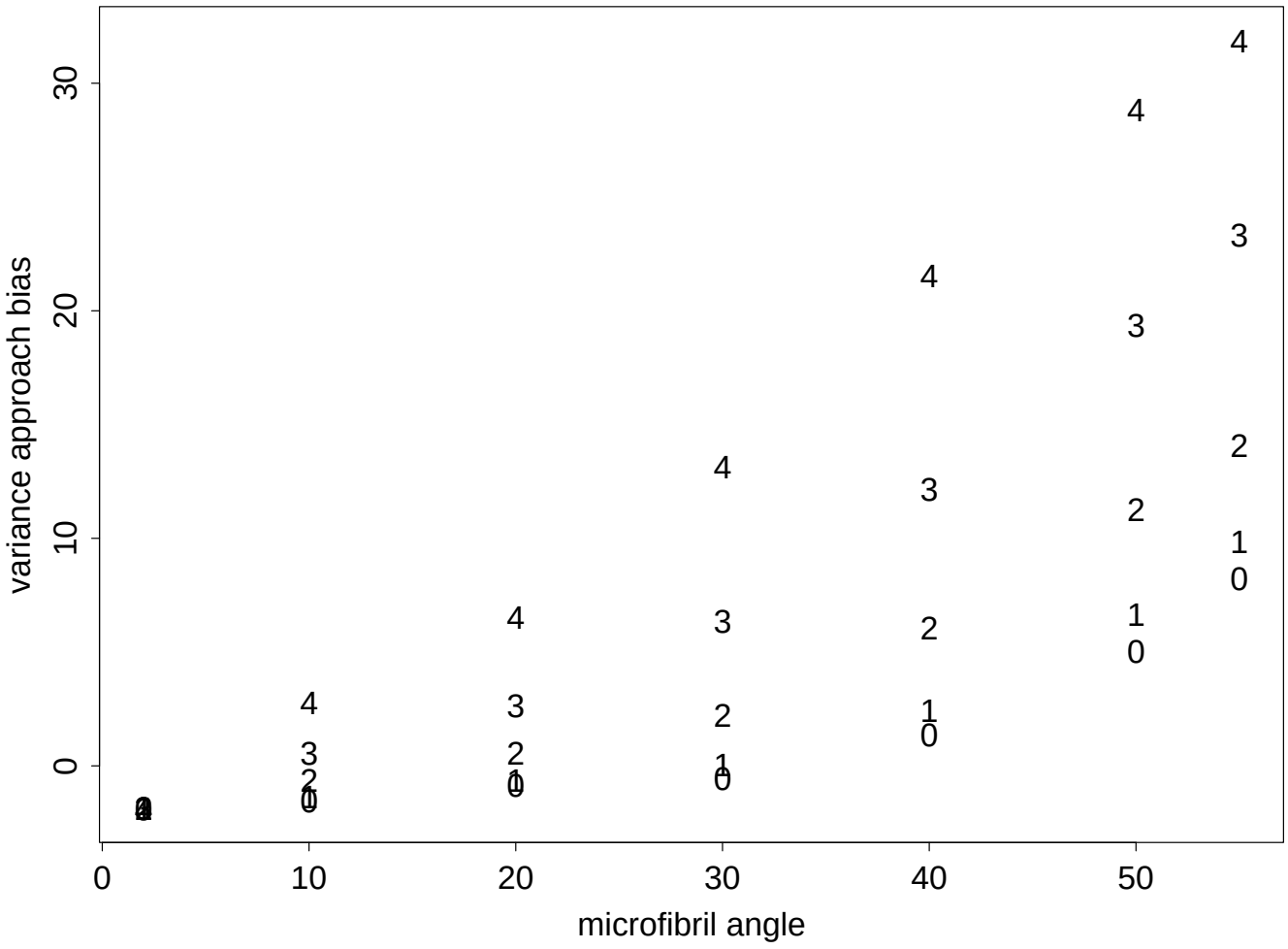

Figure 3: Variance approach bias versus true microfibril angle. **15 degree rotation**. 0 - 0 degree tilt. 1 - 10 degree tilt. 2 - 20 degree tilt. 3 - 30 degree tilt. 4 - 40 degree tilt. Theoretical biases. Profiles combined. Rectangular cell cross-section.

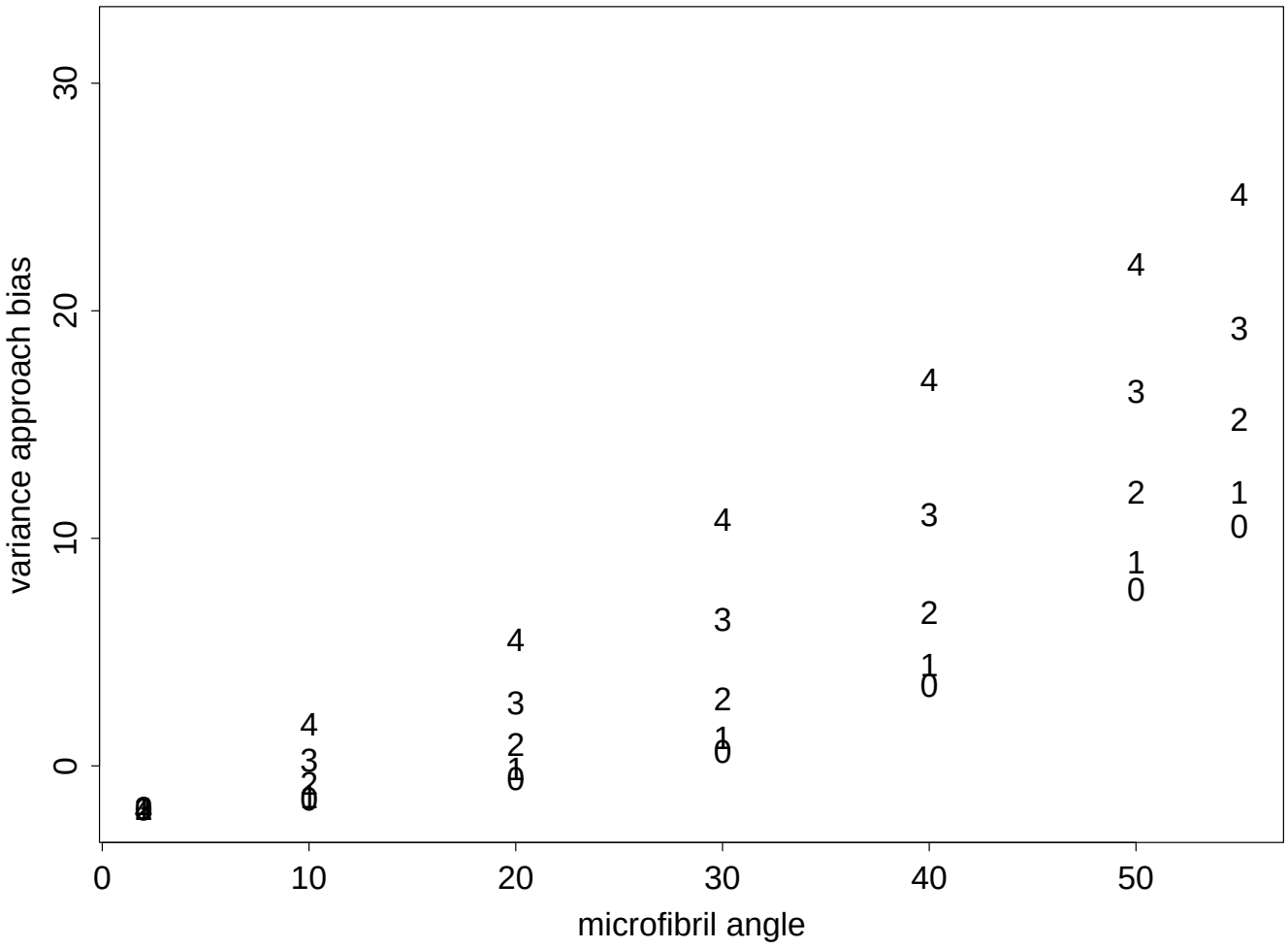

Figure 4: Variance approach bias versus true microfibril angle. **30 degree rotation**. 0 - 0 degree tilt. 1 - 10 degree tilt. 2 - 20 degree tilt. 3 - 30 degree tilt. 4 - 40 degree tilt. Theoretical biases. Profiles combined. Rectangular cell cross-section.

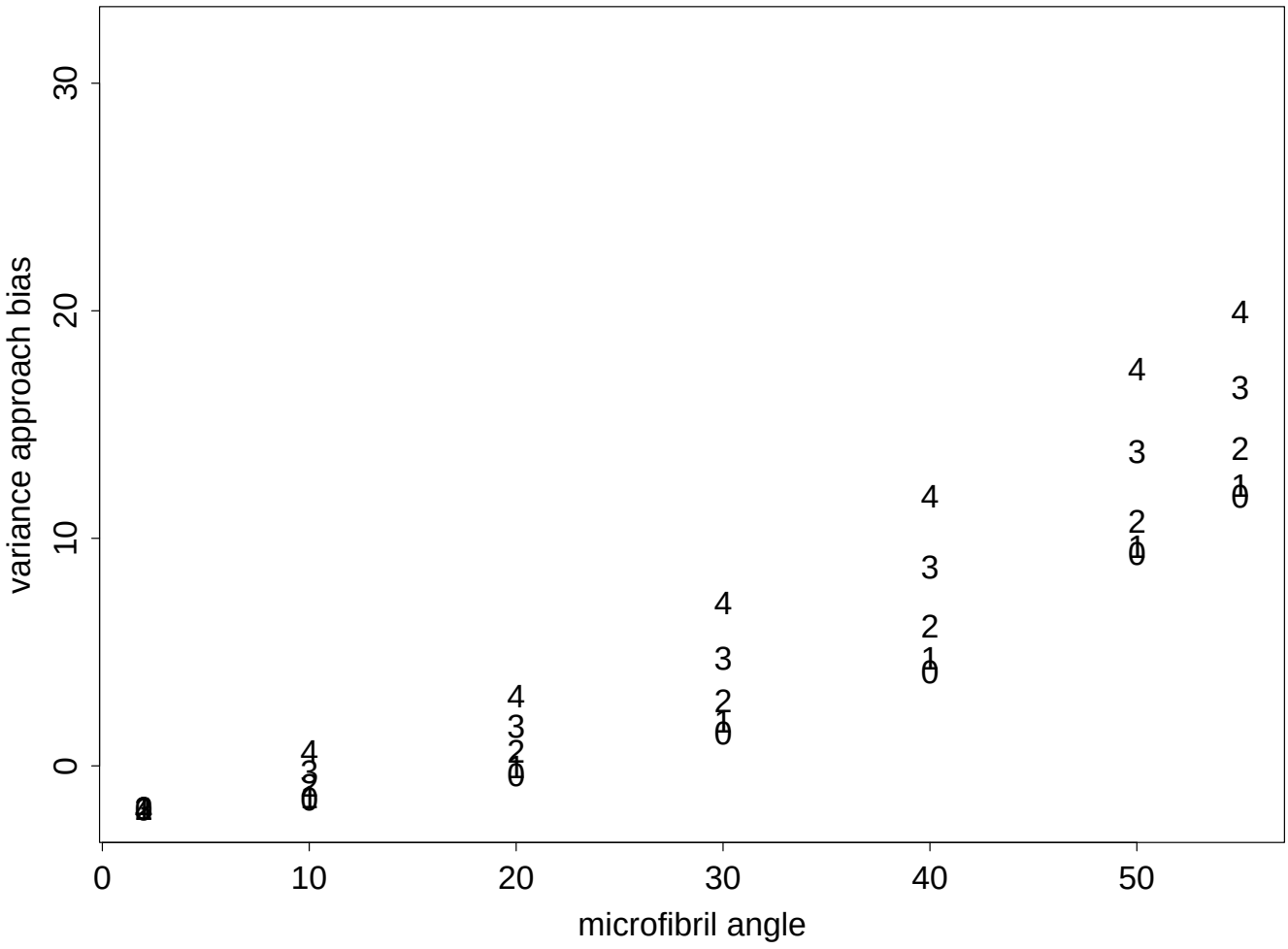

Figure 5: Variance approach bias versus true microfibril angle. **45 degree rotation**. 0 - 0 degree tilt. 1 - 10 degree tilt. 2 - 20 degree tilt. 3 - 30 degree tilt. 4 - 40 degree tilt. Theoretical biases. Profiles combined. Rectangular cell cross-section.

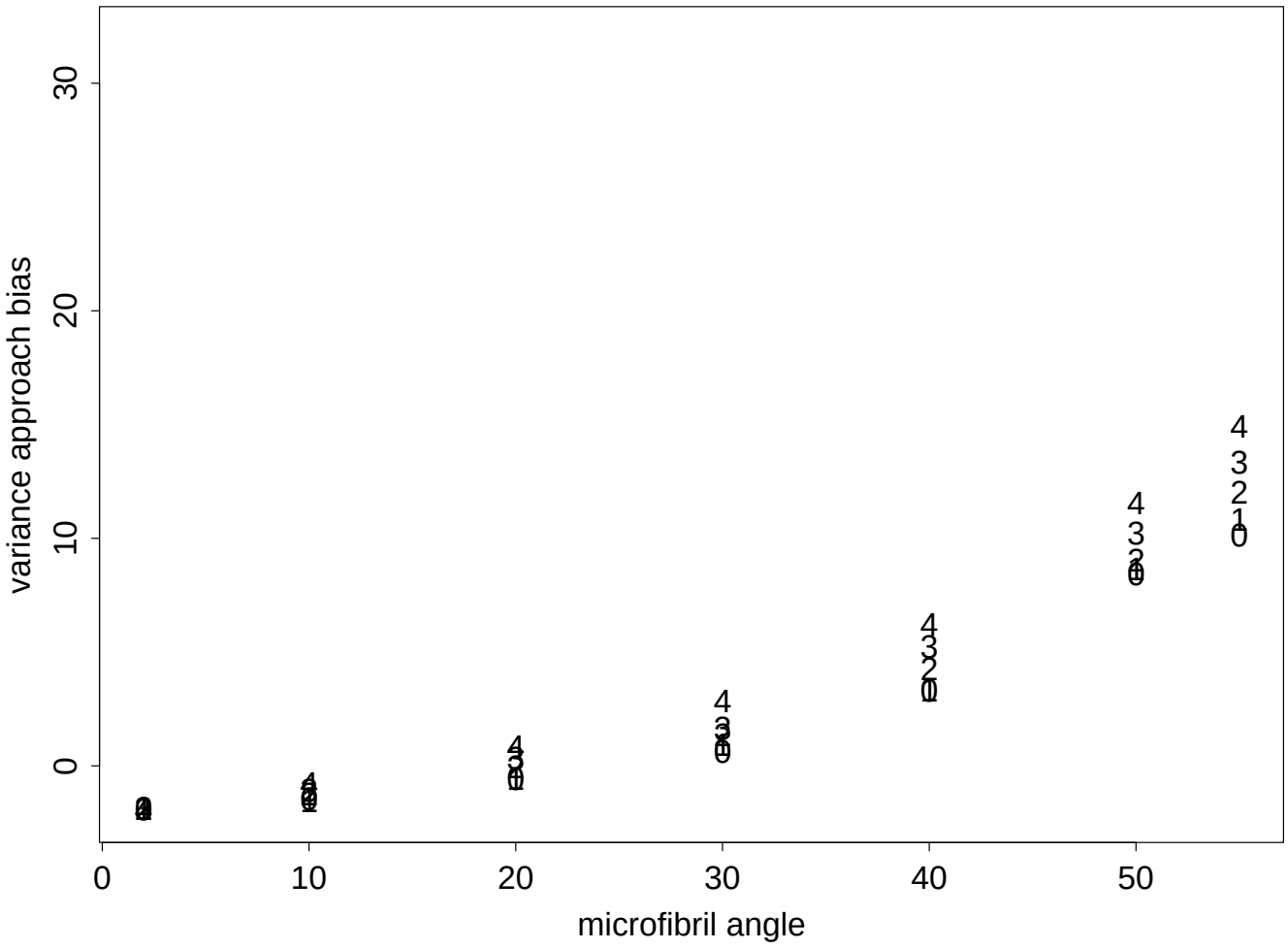

Figure 6: Variance approach bias versus true microfibril angle. **60 degree rotation**. 0 - 0 degree tilt. 1 - 10 degree tilt. 2 - 20 degree tilt. 3 - 30 degree tilt. 4 - 40 degree tilt. Theoretical biases. Profiles combined. Rectangular cell cross-section.

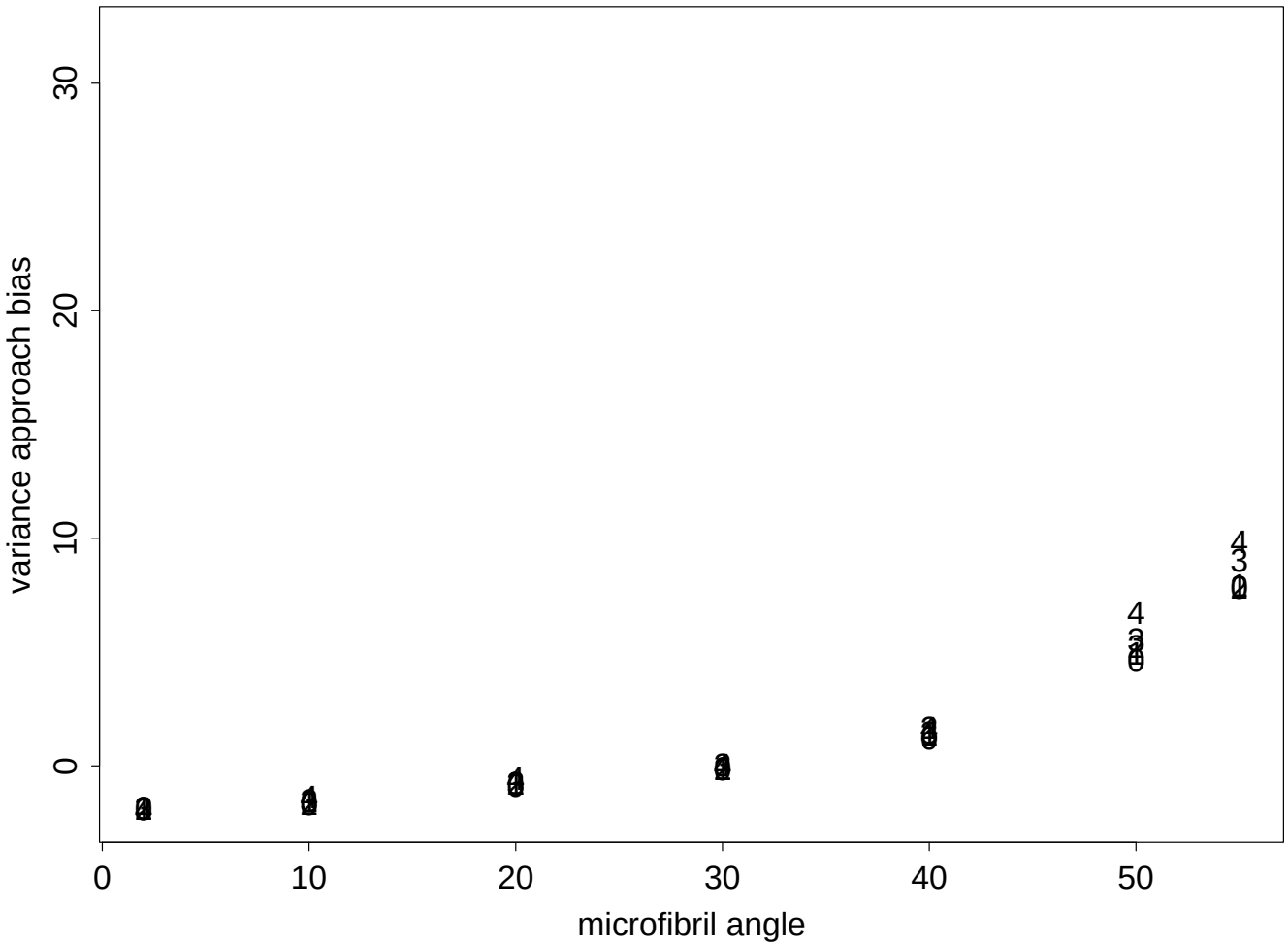

Figure 7: Variance approach bias versus true microfibril angle. **75 degree rotation**. 0 - 0 degree tilt. 1 - 10 degree tilt. 2 - 20 degree tilt. 3 - 30 degree tilt. 4 - 40 degree tilt. Theoretical biases. Profiles combined. Rectangular cell cross-section.

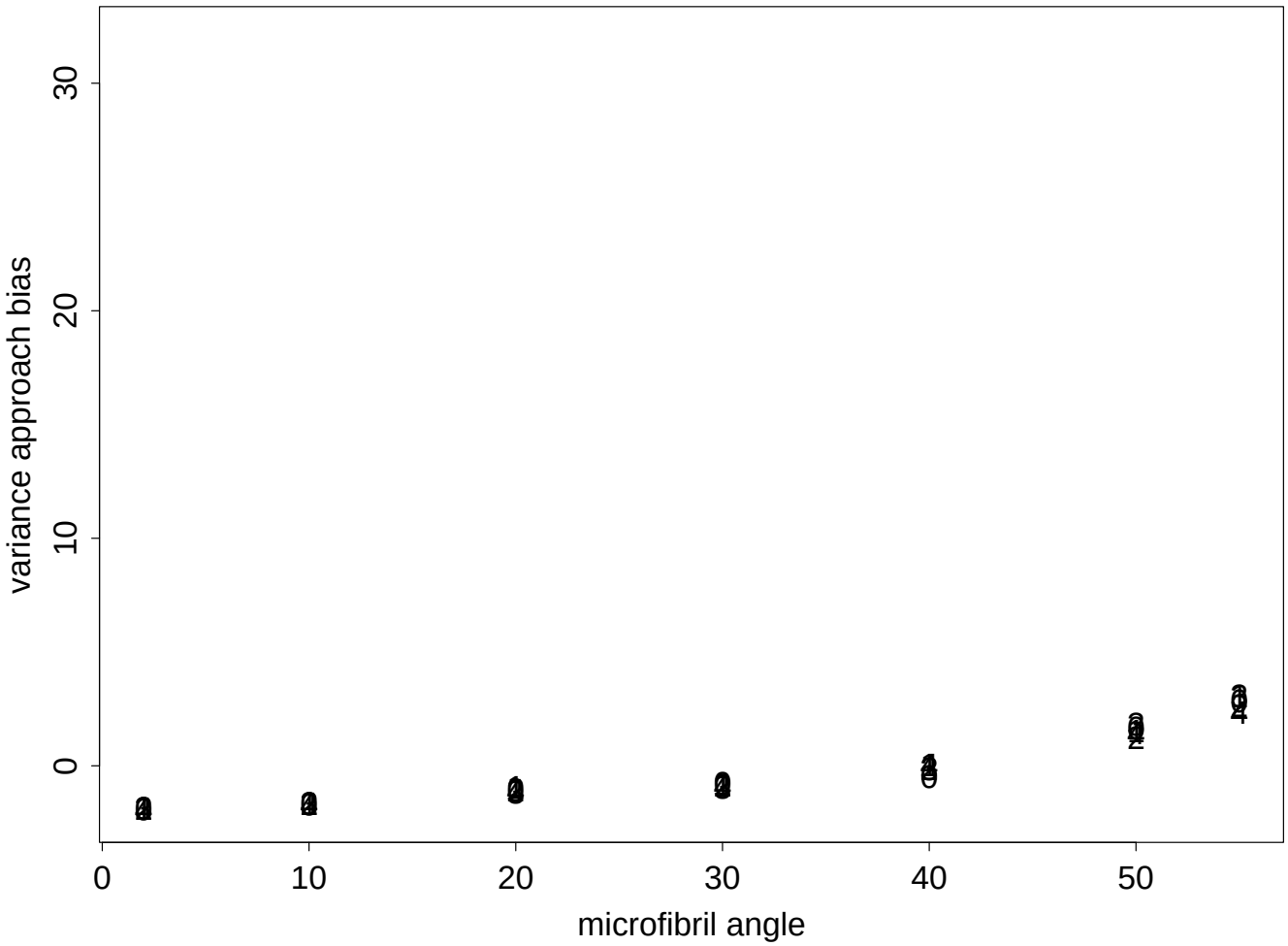

Figure 8: Variance approach bias versus true microfibril angle. **90 degree rotation**. 0 - 0 degree tilt. 1 - 10 degree tilt. 2 - 20 degree tilt. 3 - 30 degree tilt. 4 - 40 degree tilt. Theoretical biases. Profiles combined. Rectangular cell cross-section.

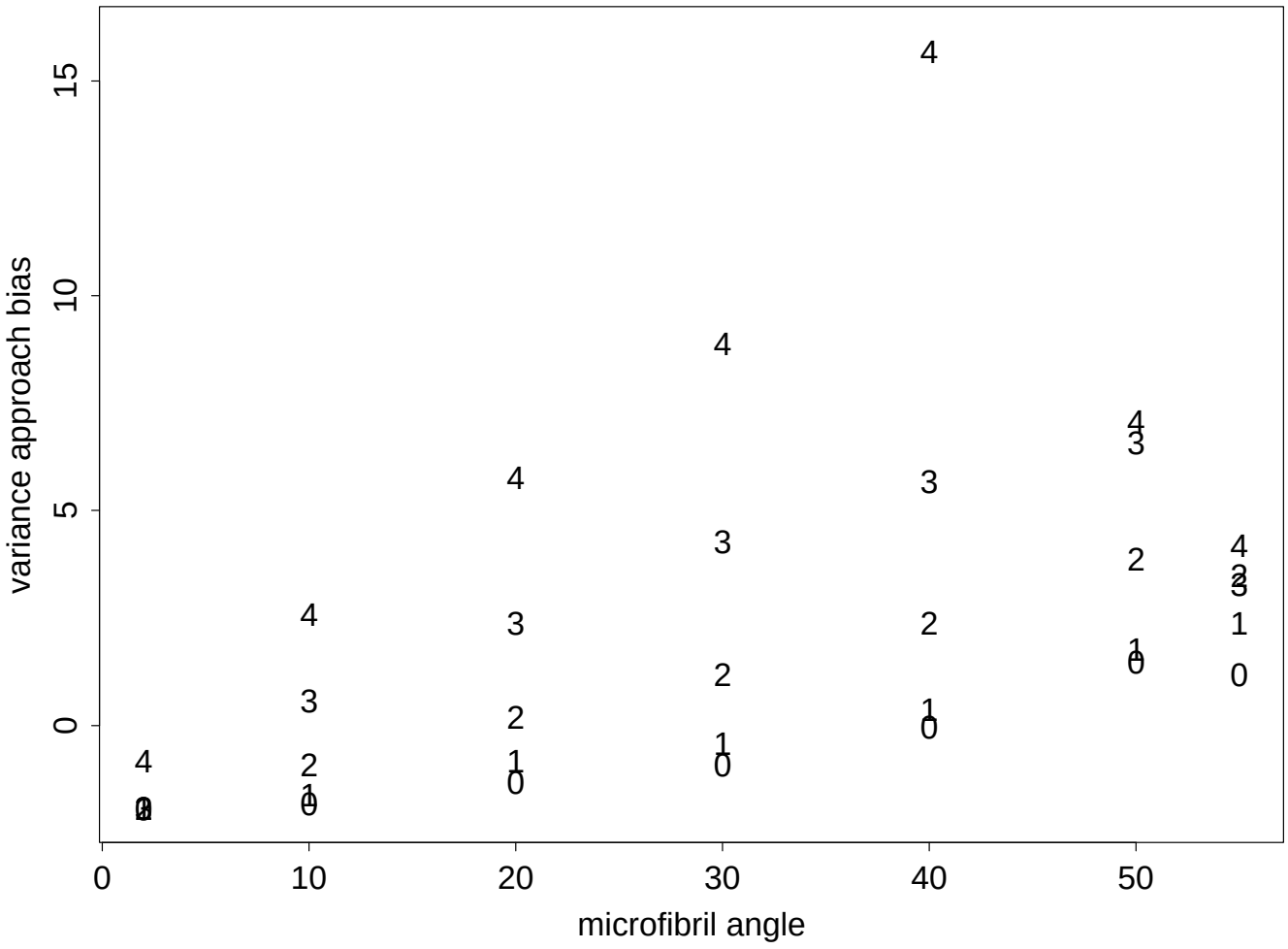

Figure 9: Variance approach bias versus true microfibril angle. **0 degree rotation**. 0 - 0 degree tilt. 1 - 10 degree tilt. 2 - 20 degree tilt. 3 - 30 degree tilt. 4 - 40 degree tilt. **Practical biases.** Profiles combined. Rectangular cell cross-section.

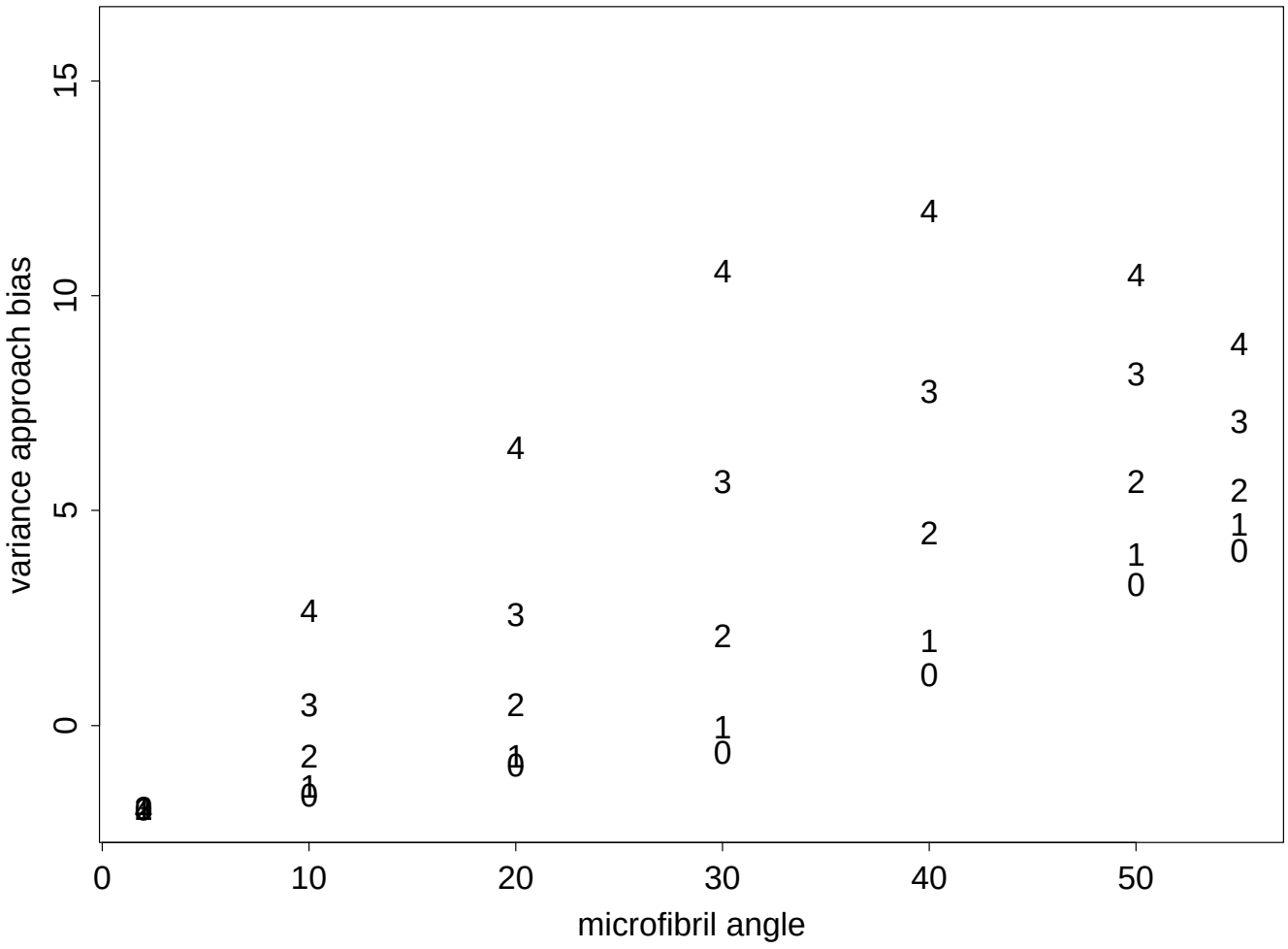

Figure 10: Variance approach bias versus true microfibril angle. **15 degree rotation**. 0 - 0 degree tilt. 1 - 10 degree tilt. 2 - 20 degree tilt. 3 - 30 degree tilt. 4 - 40 degree tilt. **Practical biases.** Profiles combined. Rectangular cell cross-section.

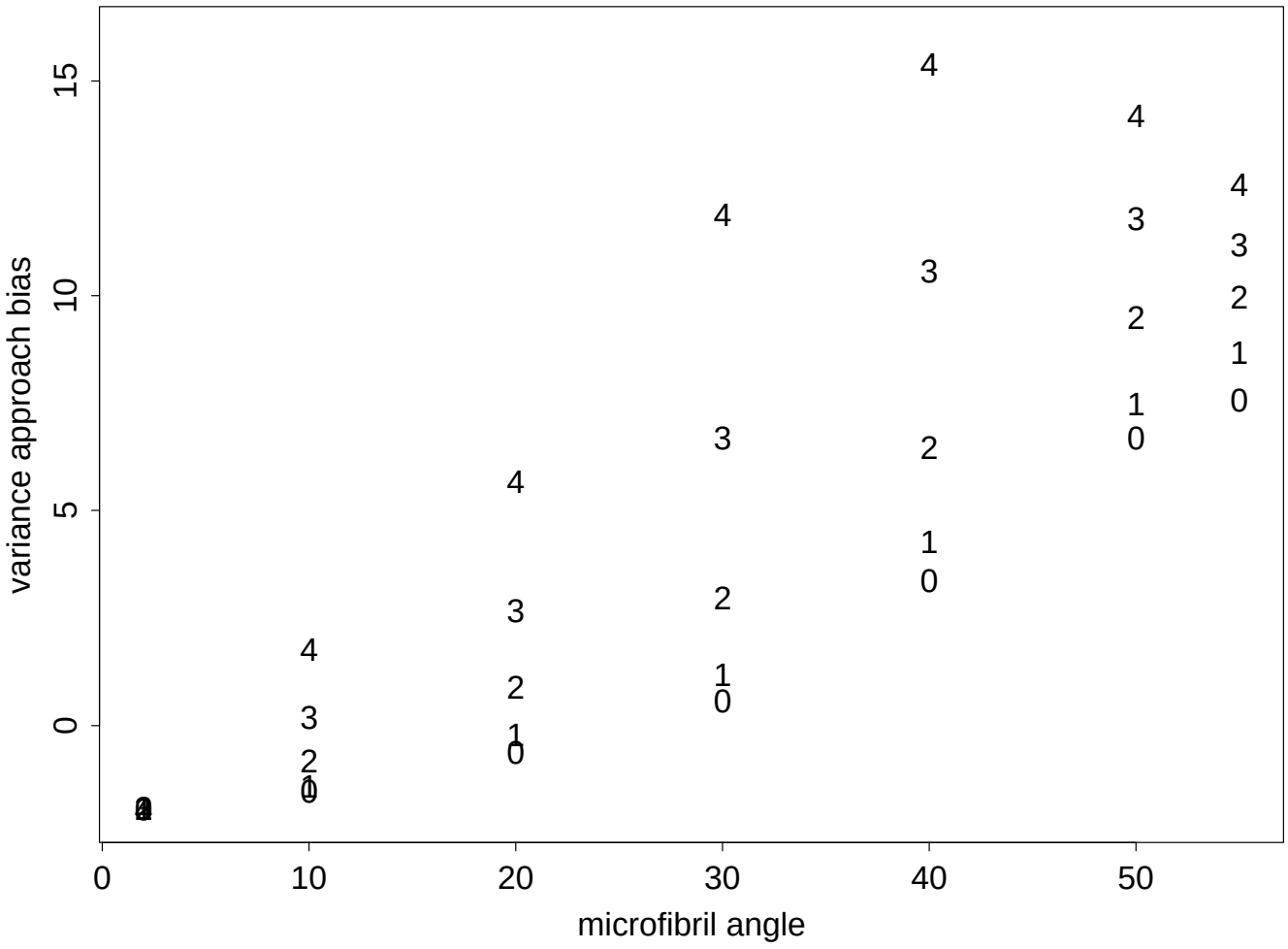

Figure 11: Variance approach bias versus true microfibril angle. **30 degree rotation**. 0 - 0 degree tilt. 1 - 10 degree tilt. 2 - 20 degree tilt. 3 - 30 degree tilt. 4 - 40 degree tilt. **Practical biases.** Profiles combined. Rectangular cell cross-section.

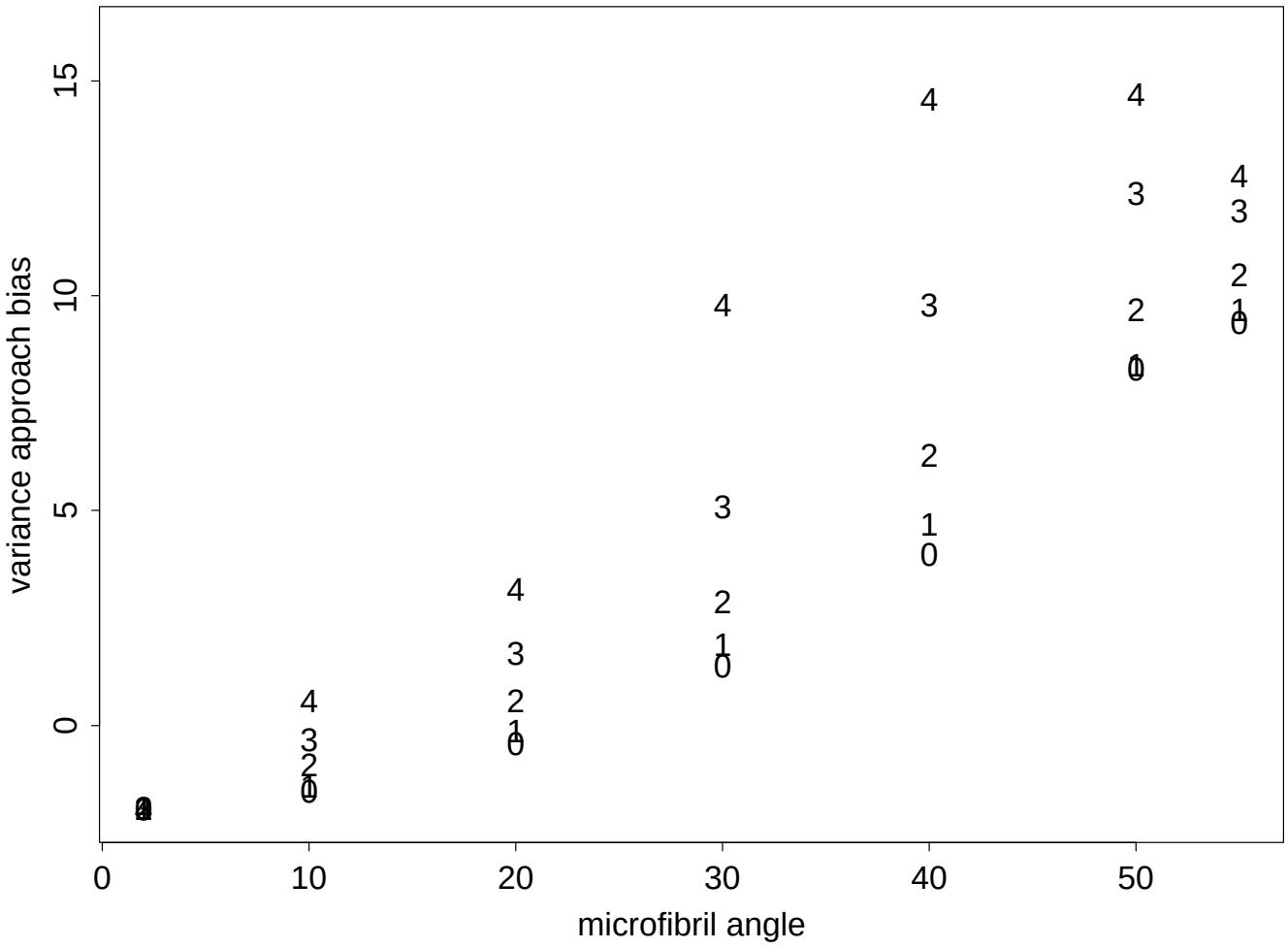

Figure 12: Variance approach bias versus true microfibril angle. **45 degree rotation**. 0 - 0 degree tilt. 1 - 10 degree tilt. 2 - 20 degree tilt. 3 - 30 degree tilt. 4 - 40 degree tilt. **Practical biases.** Profiles combined. Rectangular cell cross-section.

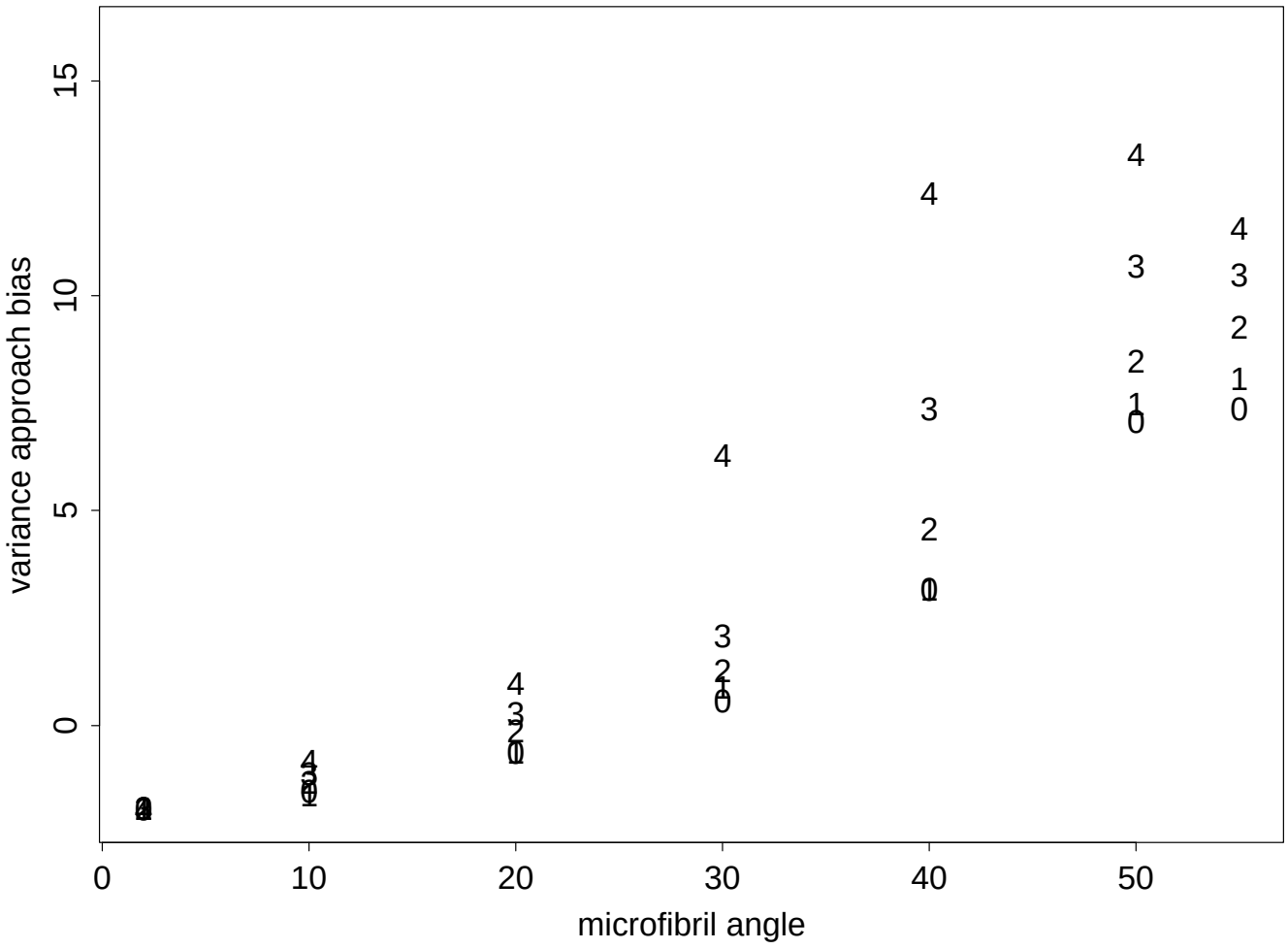

Figure 13: Variance approach bias versus true microfibril angle. **60 degree rotation**. 0 - 0 degree tilt. 1 - 10 degree tilt. 2 - 20 degree tilt. 3 - 30 degree tilt. 4 - 40 degree tilt. **Practical biases.** Profiles combined. Rectangular cell cross-section.

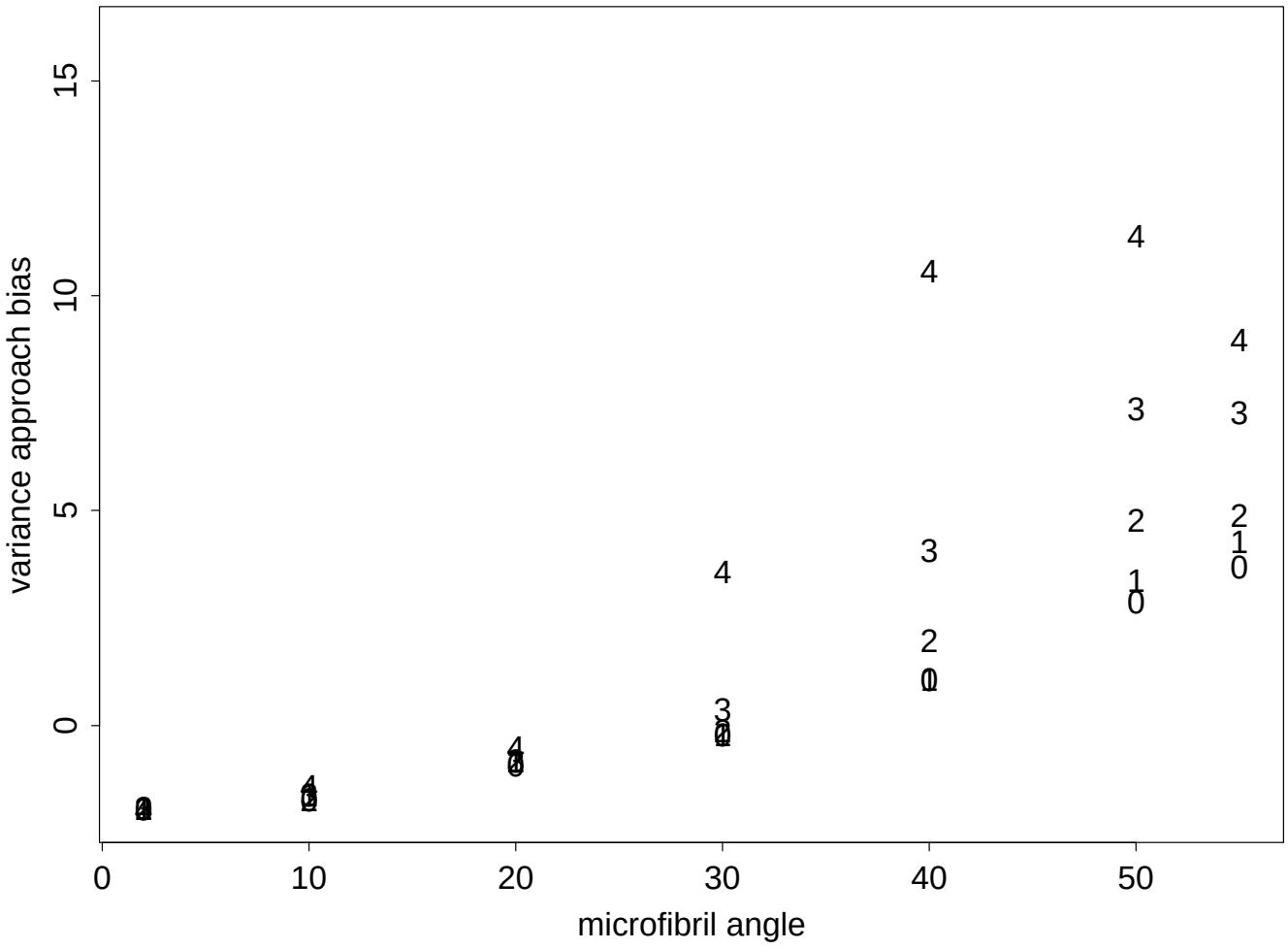

Figure 14: Variance approach bias versus true microfibril angle. **75 degree rotation**. 0 - 0 degree tilt. 1 - 10 degree tilt. 2 - 20 degree tilt. 3 - 30 degree tilt. 4 - 40 degree tilt. **Practical biases.** Profiles combined. Rectangular cell cross-section.

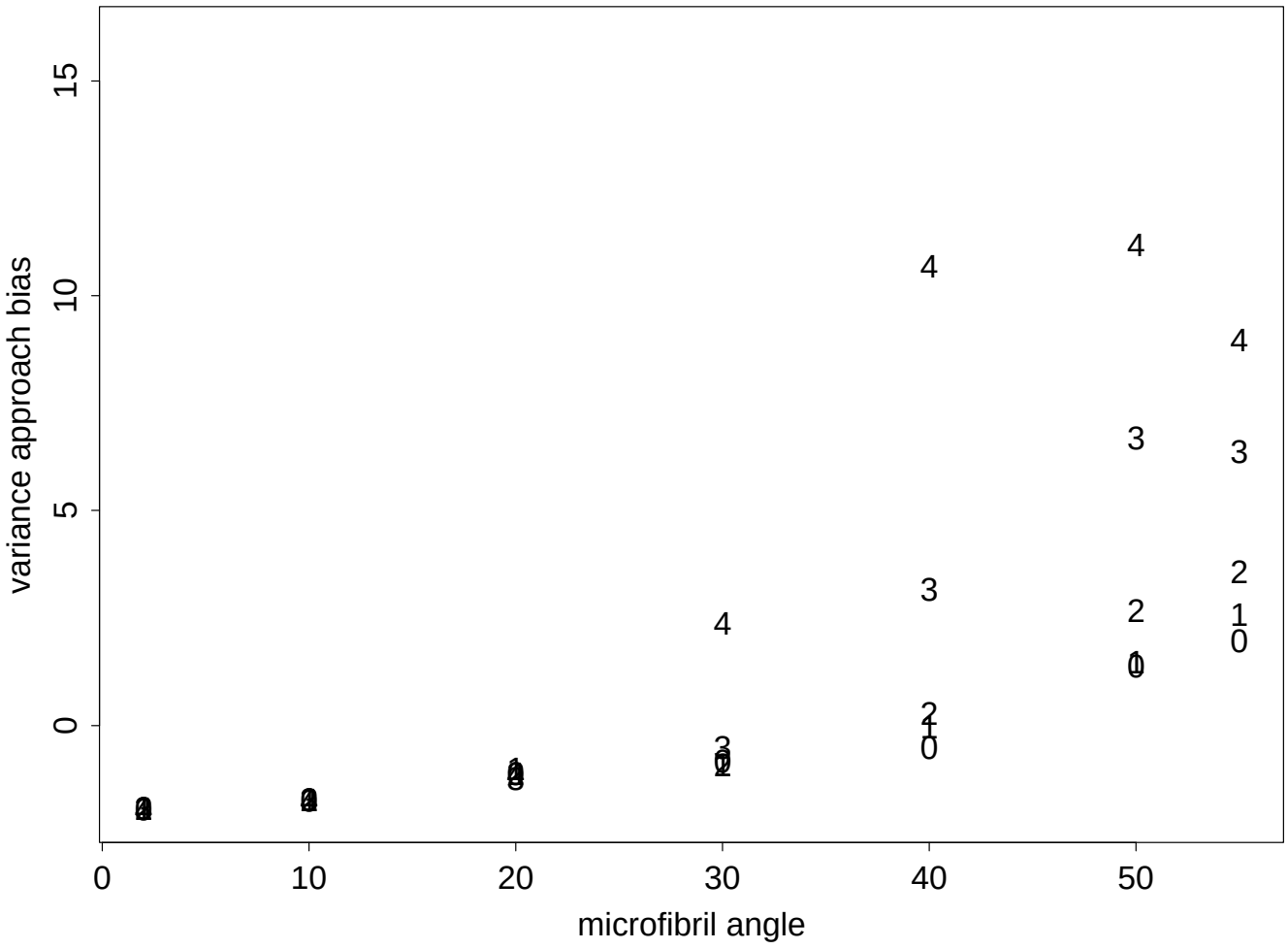

Figure 15: Variance approach bias versus true microfibril angle. **90 degree rotation**. 0 - 0 degree tilt. 1 - 10 degree tilt. 2 - 20 degree tilt. 3 - 30 degree tilt. 4 - 40 degree tilt. **Practical biases.** Profiles combined. Rectangular cell cross-section.

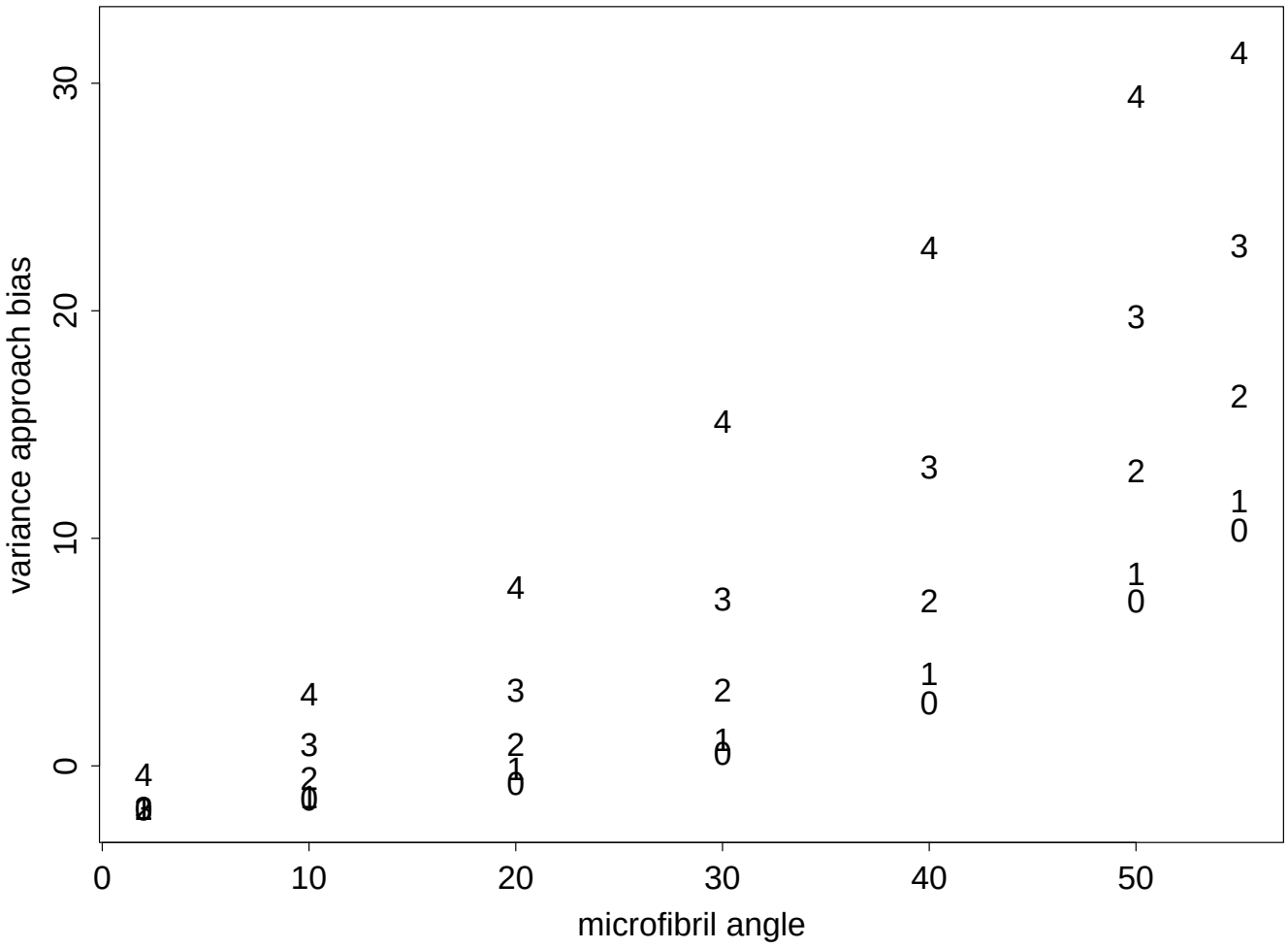

Figure 16: Variance approach bias versus true microfibril angle. **0 degree rotation**. 0 - 0 degree tilt. 1 - 10 degree tilt. 2 - 20 degree tilt. 3 - 30 degree tilt. 4 - 40 degree tilt. Theoretical biases. Profiles combined. Hexagonal cell cross-section.

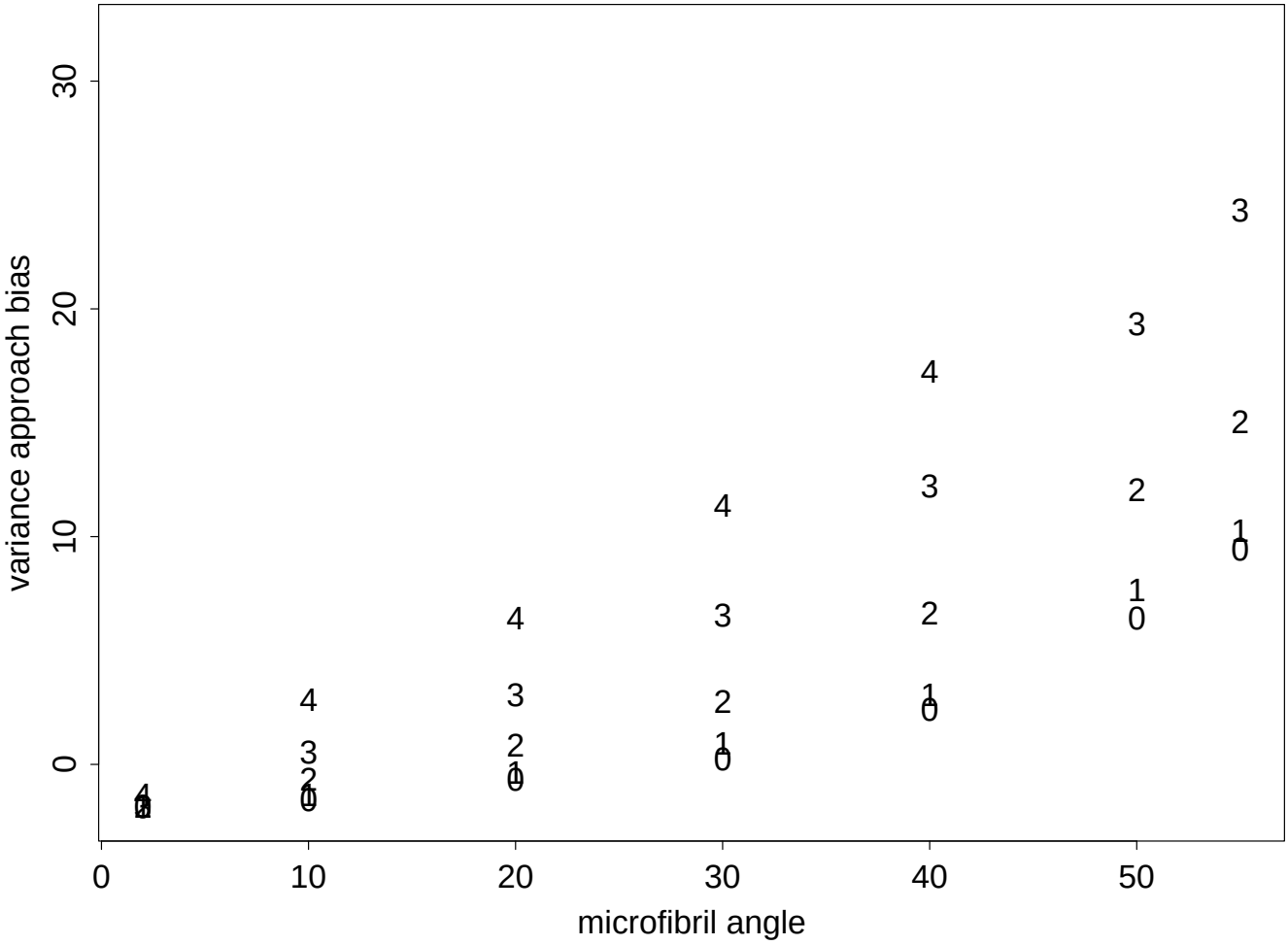

Figure 17: Variance approach bias versus true microfibril angle. **15 degree rotation**. 0 - 0 degree tilt. 1 - 10 degree tilt. 2 - 20 degree tilt. 3 - 30 degree tilt. 4 - 40 degree tilt. Theoretical biases. Profiles combined. Hexagonal cell cross-section. Values are missing for 40 degree tilt, 50 and 55 degree MFAs because there are no reflections from the left 1 face in these cases.

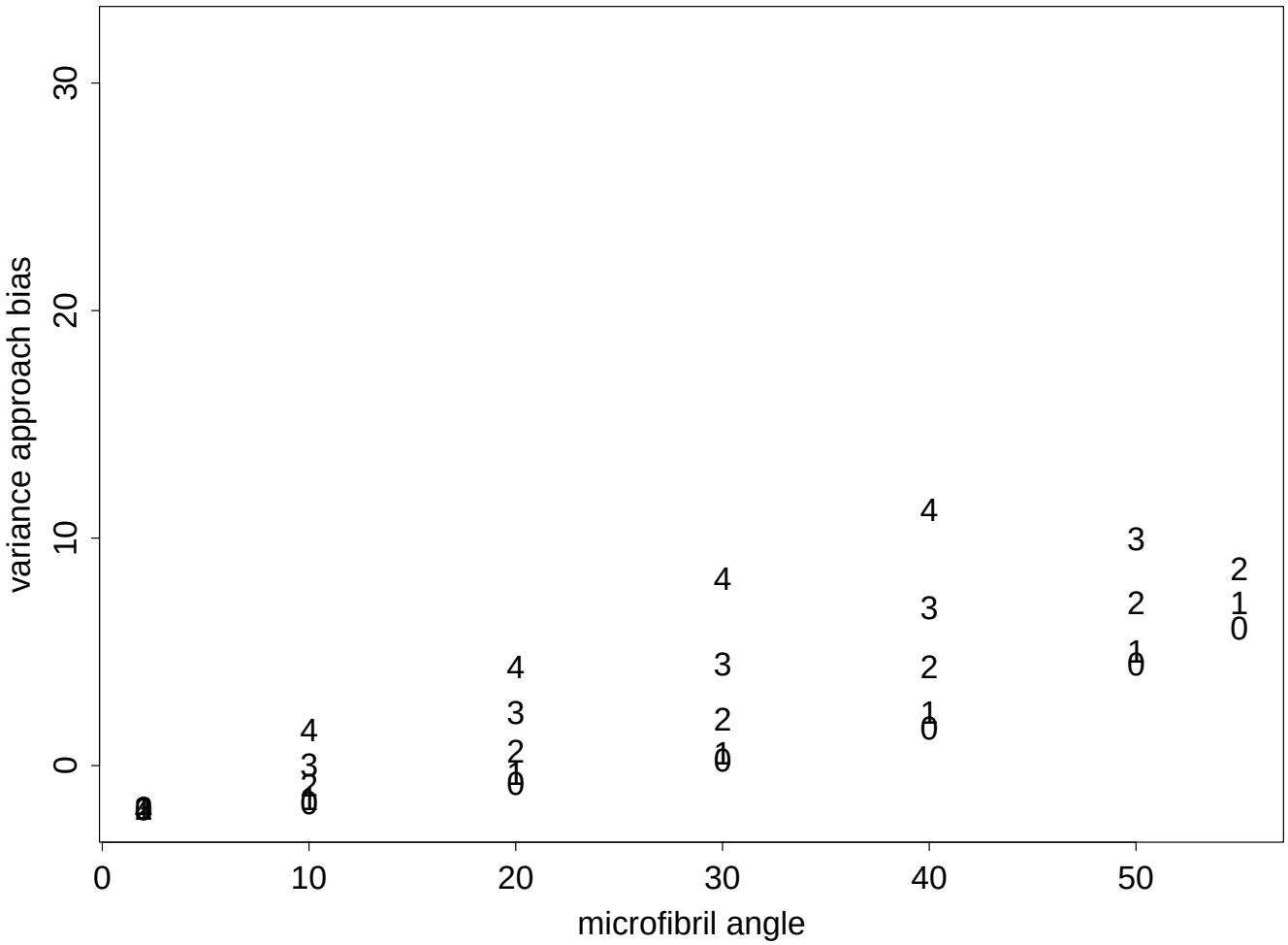

Figure 18: Variance approach bias versus true microfibril angle. **30 degree rotation**. 0 - 0 degree tilt. 1 - 10 degree tilt. 2 - 20 degree tilt. 3 - 30 degree tilt. 4 - 40 degree tilt. Theoretical biases. Profiles combined. Hexagonal cell cross-section. Values are missing for 30 degree tilt, 55 degree MFA, and 40 degree tilt, 50 and 55 degree MFAs because there are no reflections from the left 1 face in these cases.

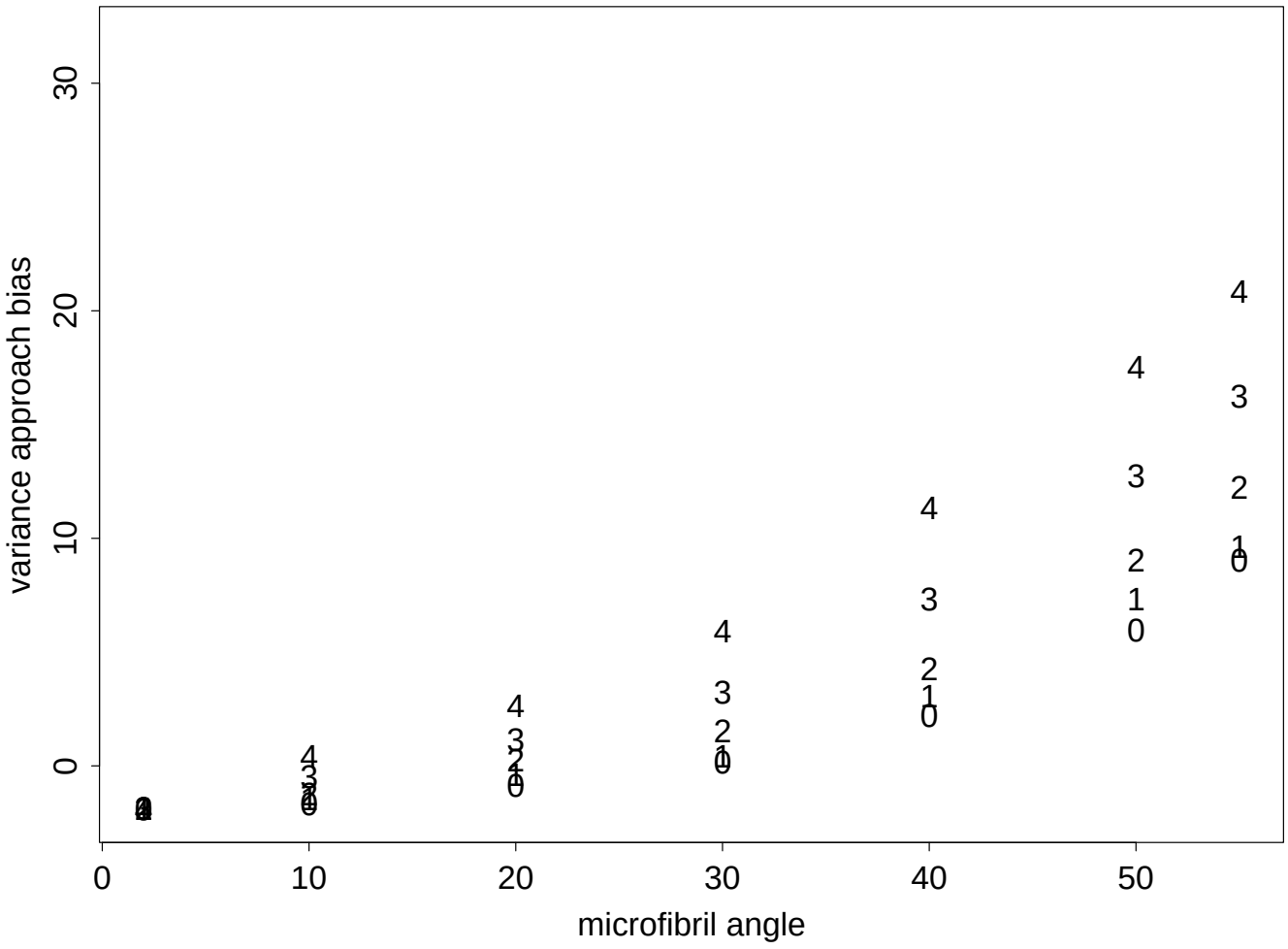

Figure 19: Variance approach bias versus true microfibril angle. **45 degree rotation**. 0 - 0 degree tilt. 1 - 10 degree tilt. 2 - 20 degree tilt. 3 - 30 degree tilt. 4 - 40 degree tilt. Theoretical biases. Profiles combined. Hexagonal cell cross-section.

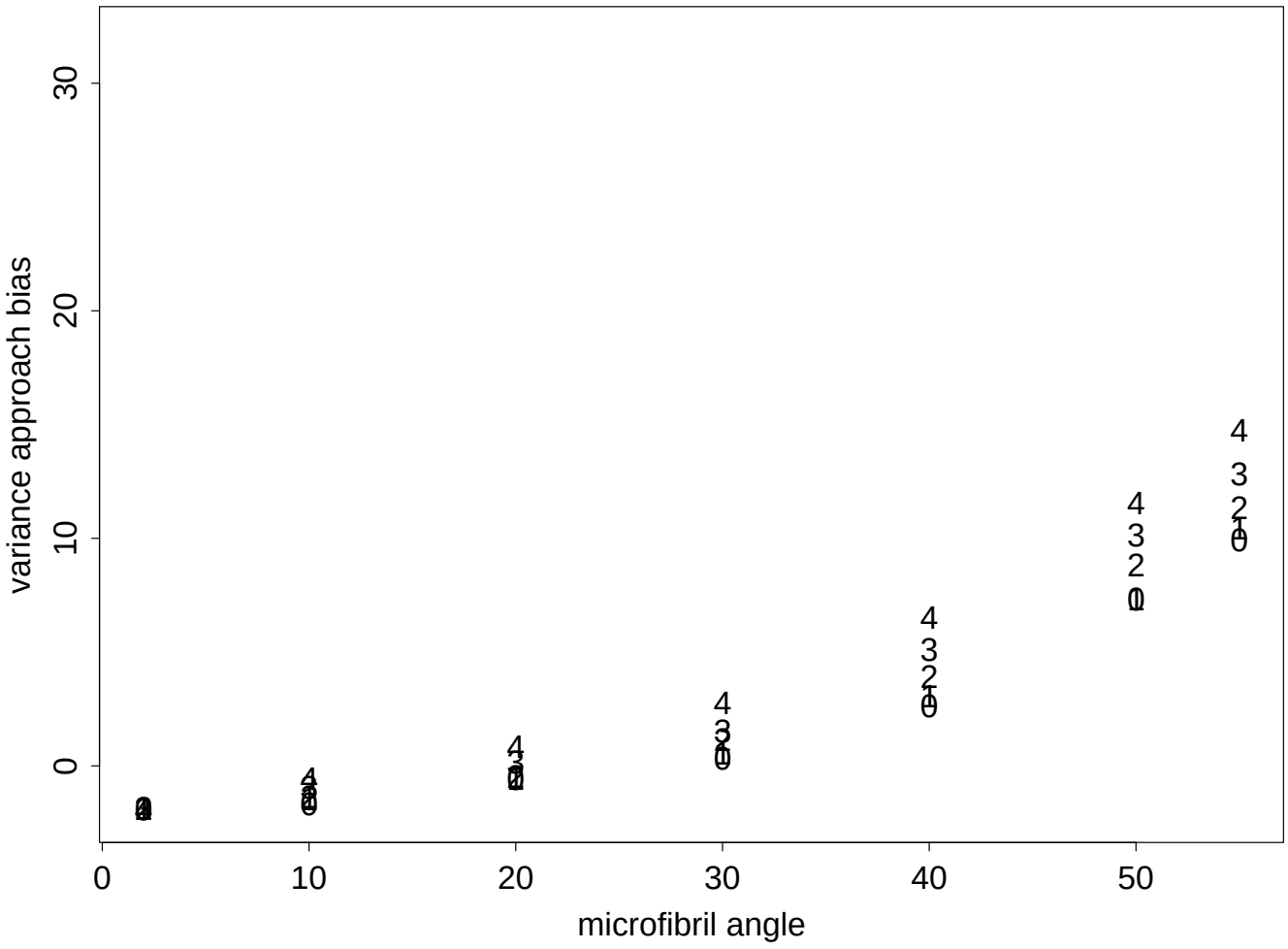

Figure 20: Variance approach bias versus true microfibril angle. **60 degree rotation**. 0 - 0 degree tilt. 1 - 10 degree tilt. 2 - 20 degree tilt. 3 - 30 degree tilt. 4 - 40 degree tilt. Theoretical biases. Profiles combined. Hexagonal cell cross-section.

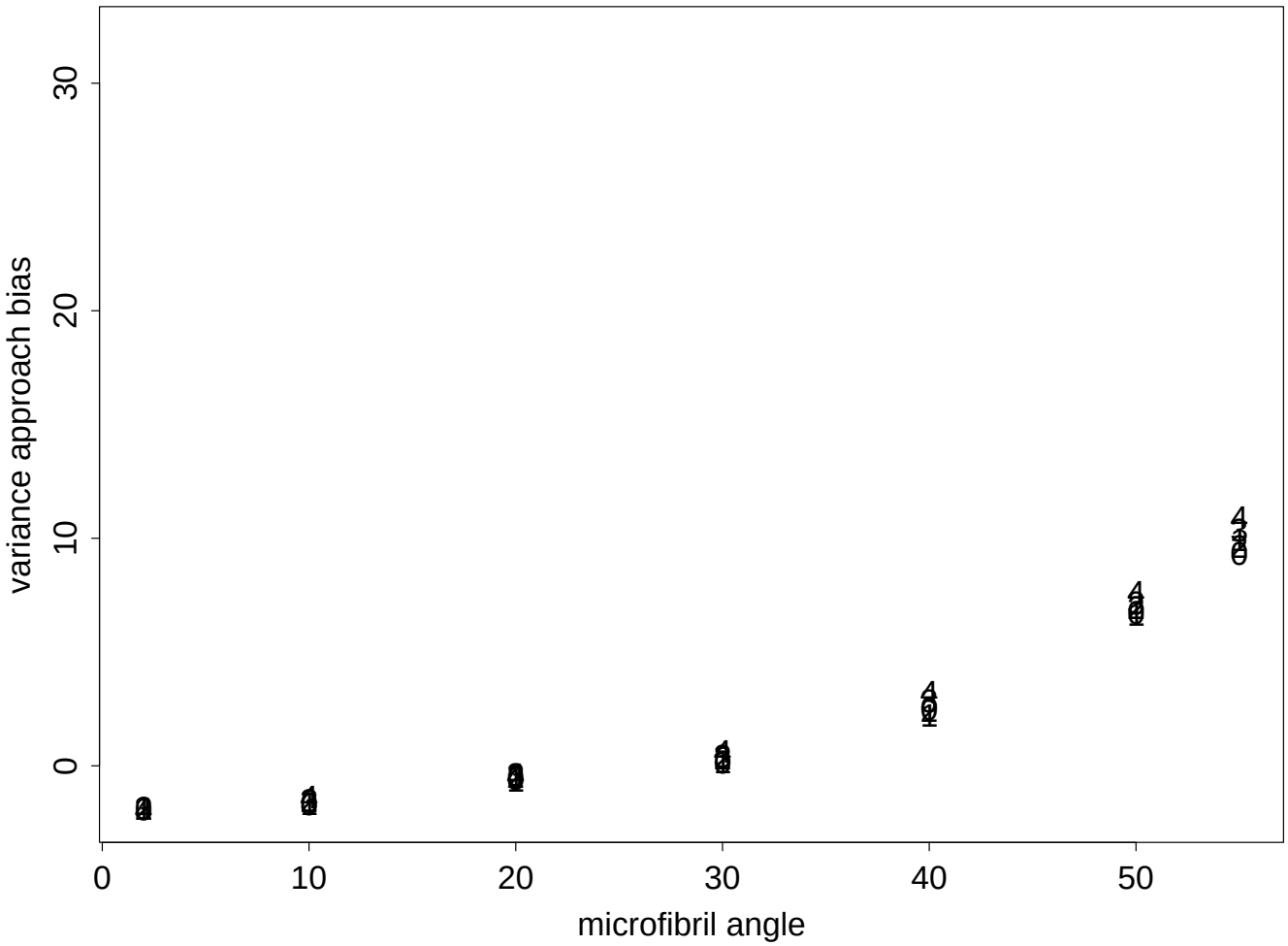

Figure 21: Variance approach bias versus true microfibril angle. **75 degree rotation**. 0 - 0 degree tilt. 1 - 10 degree tilt. 2 - 20 degree tilt. 3 - 30 degree tilt. 4 - 40 degree tilt. Theoretical biases. Profiles combined. Hexagonal cell cross-section.

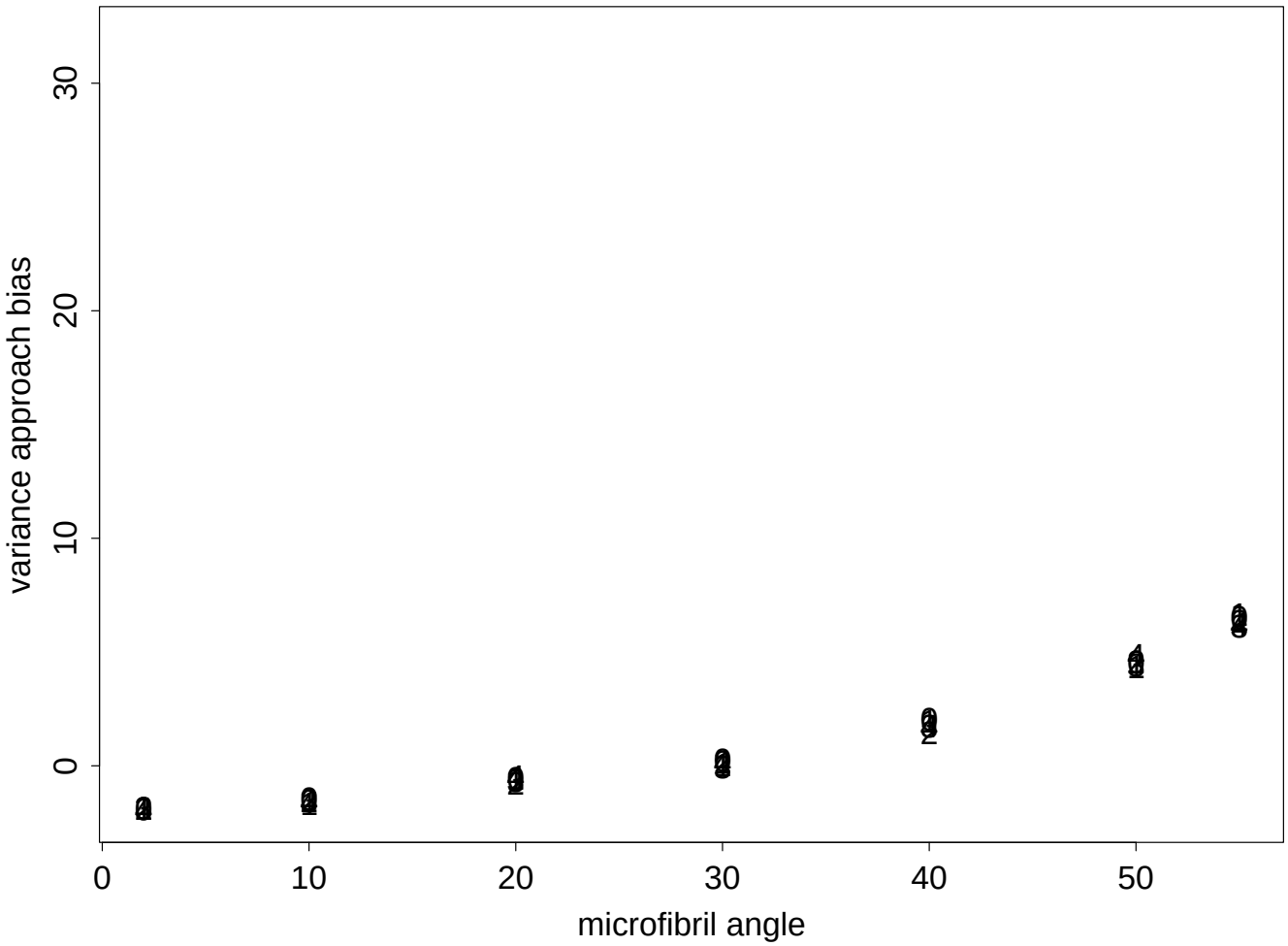

Figure 22: Variance approach bias versus true microfibril angle. **90 degree rotation**. 0 - 0 degree tilt. 1 - 10 degree tilt. 2 - 20 degree tilt. 3 - 30 degree tilt. 4 - 40 degree tilt. Theoretical biases. Profiles combined. Hexagonal cell cross-section.

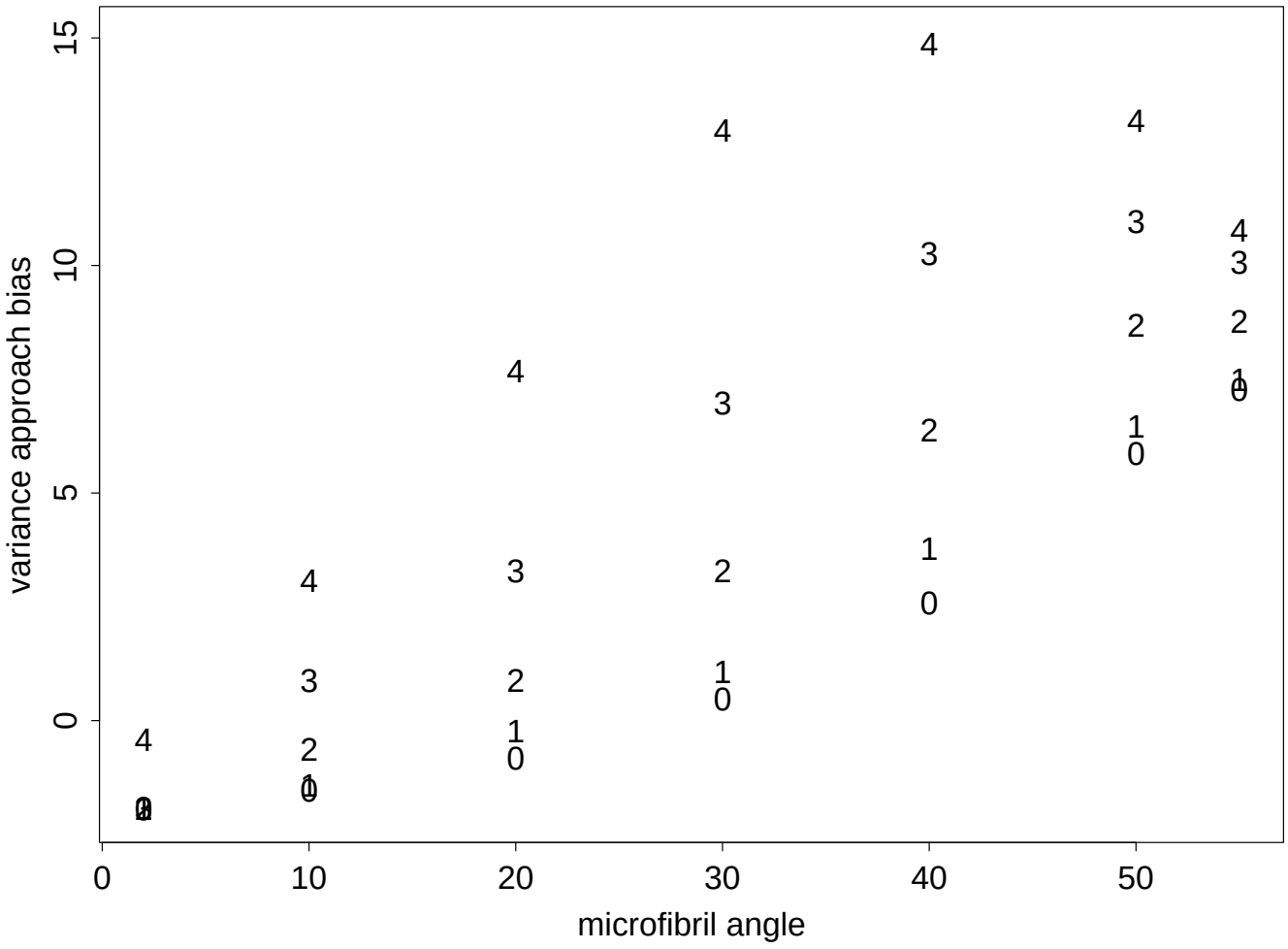

Figure 23: Variance approach bias versus true microfibril angle. **0 degree rotation**. 0 - 0 degree tilt. 1 - 10 degree tilt. 2 - 20 degree tilt. 3 - 30 degree tilt. 4 - 40 degree tilt. **Practical biases.** Profiles combined. Hexagonal cell cross-section.

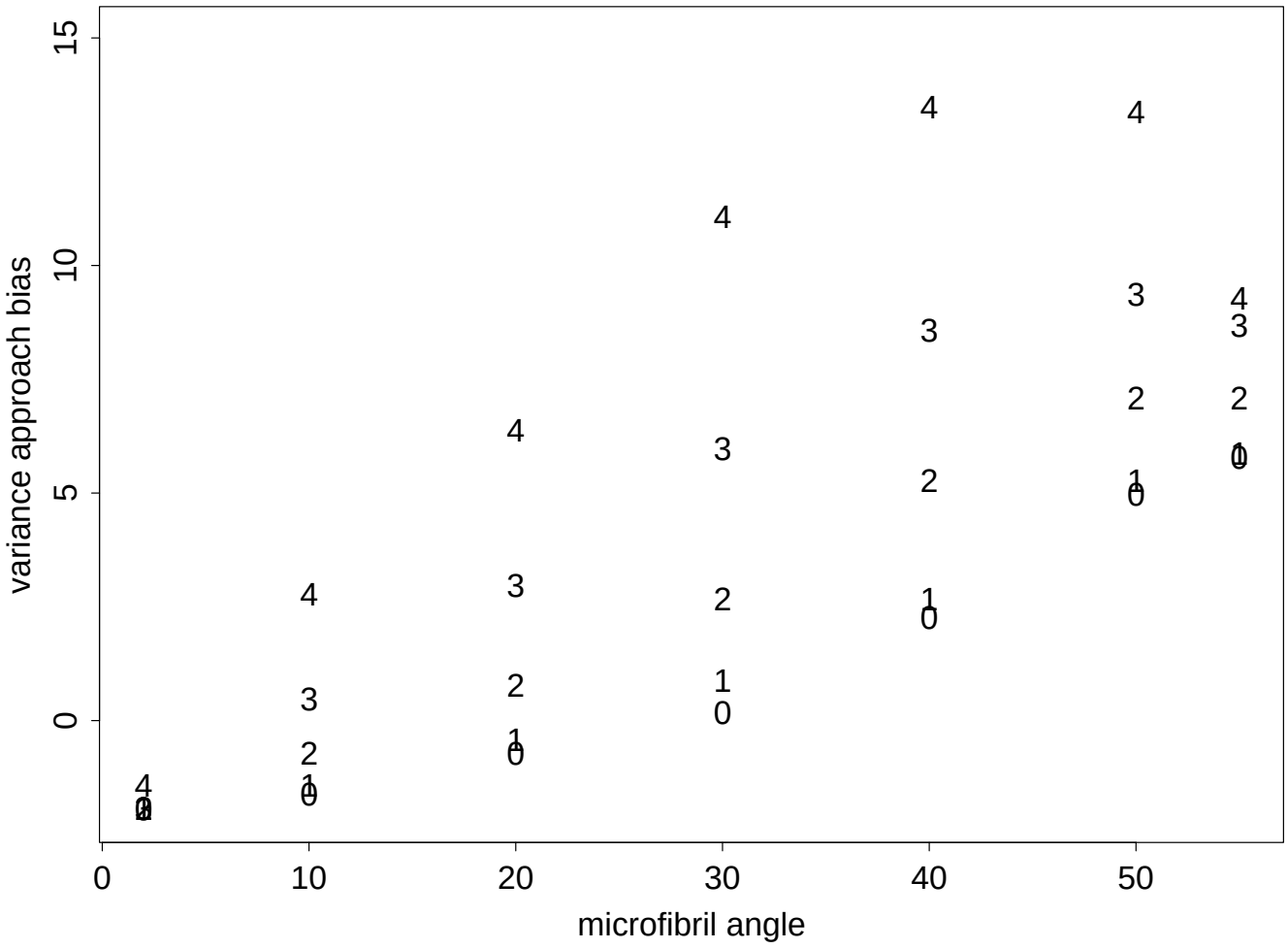

Figure 24: Variance approach bias versus true microfibril angle. **15 degree rotation**. 0 - 0 degree tilt. 1 - 10 degree tilt. 2 - 20 degree tilt. 3 - 30 degree tilt. 4 - 40 degree tilt. **Practical biases.** Profiles combined. Hexagonal cell cross-section.

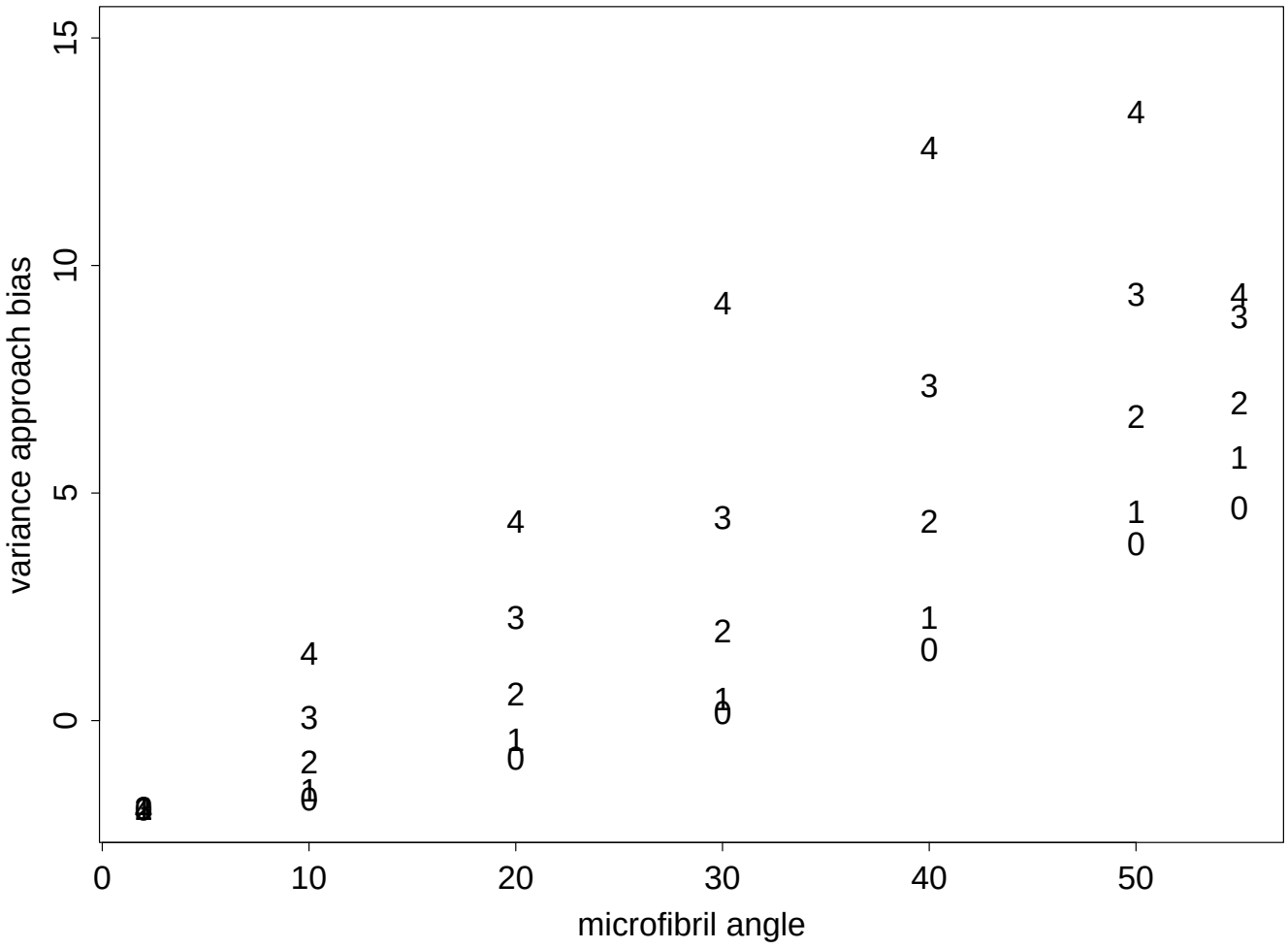

Figure 25: Variance approach bias versus true microfibril angle. **30 degree rotation**. 0 - 0 degree tilt. 1 - 10 degree tilt. 2 - 20 degree tilt. 3 - 30 degree tilt. 4 - 40 degree tilt. **Practical biases.** Profiles combined. Hexagonal cell cross-section.

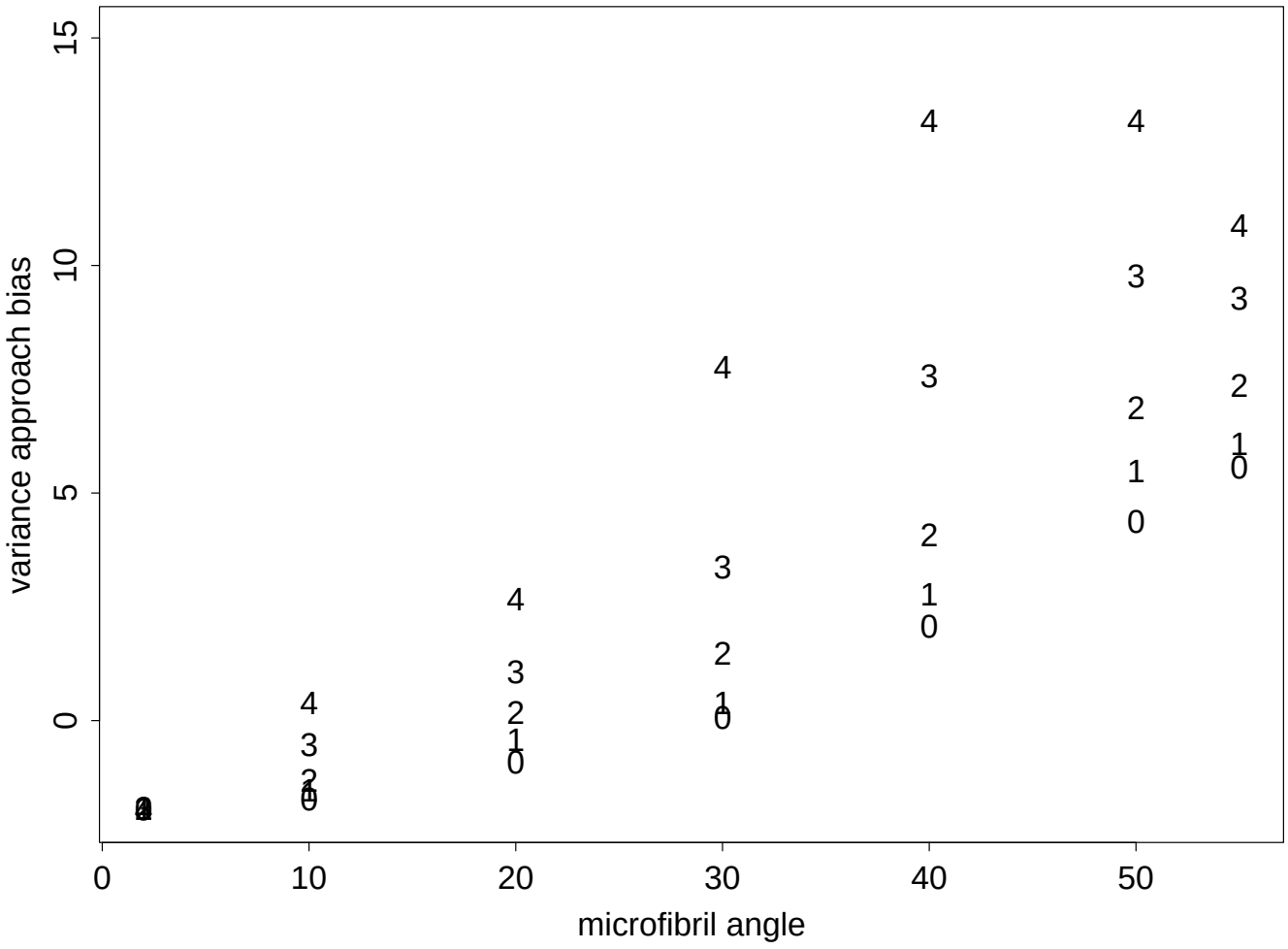

Figure 26: Variance approach bias versus true microfibril angle. **45 degree rotation**. 0 - 0 degree tilt. 1 - 10 degree tilt. 2 - 20 degree tilt. 3 - 30 degree tilt. 4 - 40 degree tilt. **Practical biases.** Profiles combined. Hexagonal cell cross-section.

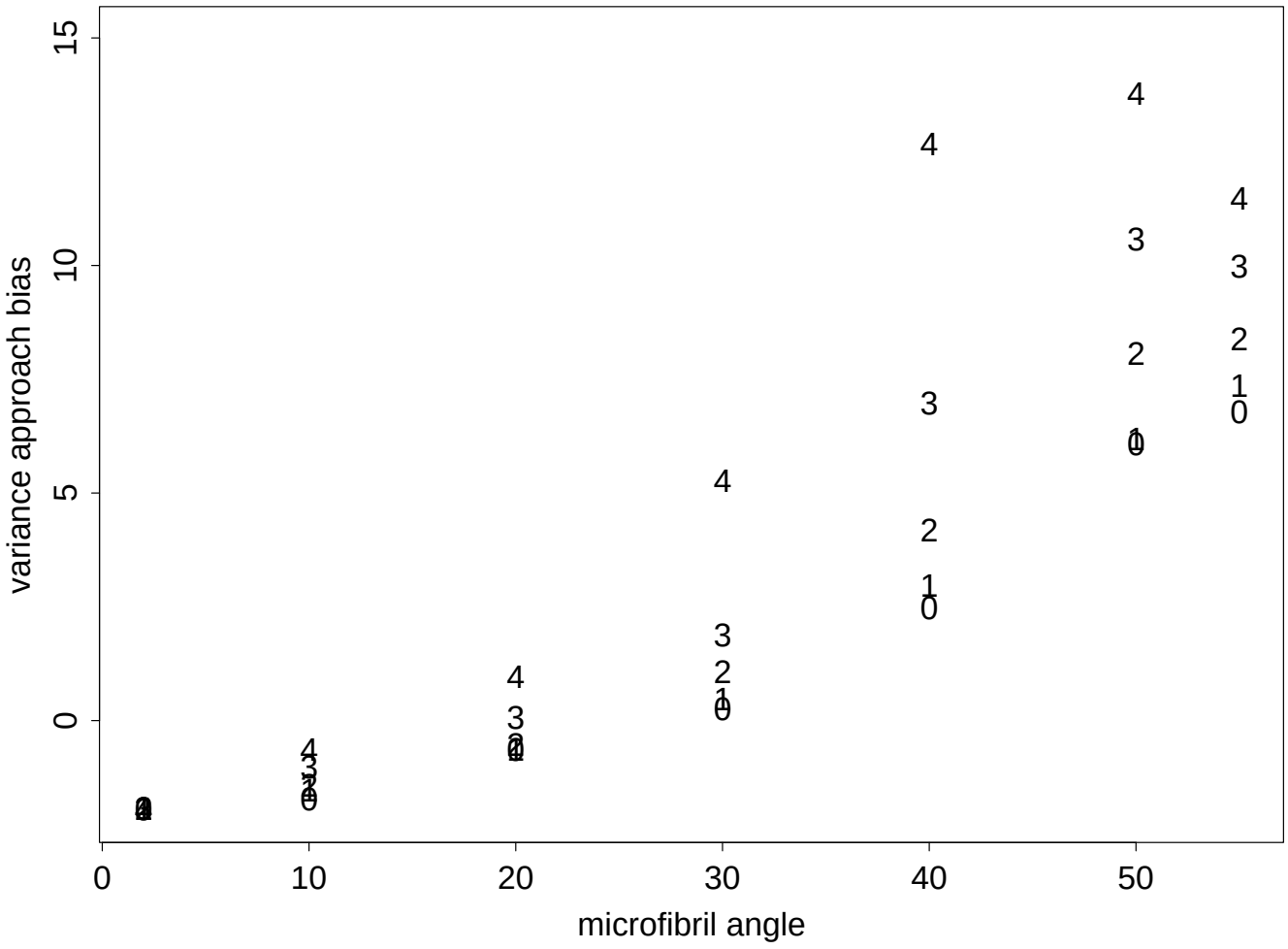

Figure 27: Variance approach bias versus true microfibril angle. **60 degree rotation**. 0 - 0 degree tilt. 1 - 10 degree tilt. 2 - 20 degree tilt. 3 - 30 degree tilt. 4 - 40 degree tilt. **Practical biases.** Profiles combined. Hexagonal cell cross-section.

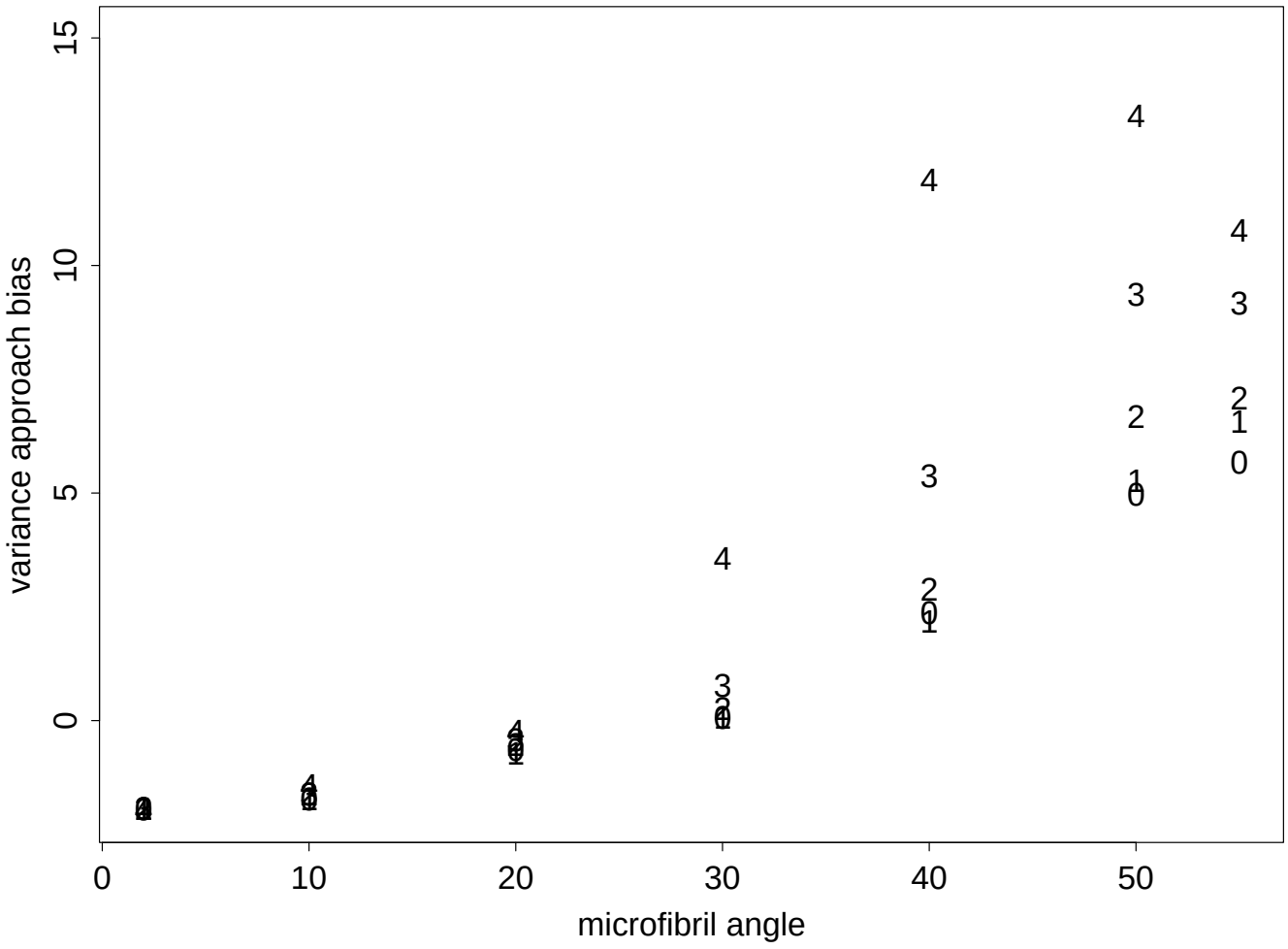

Figure 28: Variance approach bias versus true microfibril angle. **75 degree rotation**. 0 - 0 degree tilt. 1 - 10 degree tilt. 2 - 20 degree tilt. 3 - 30 degree tilt. 4 - 40 degree tilt. **Practical biases.** Profiles combined. Hexagonal cell cross-section.

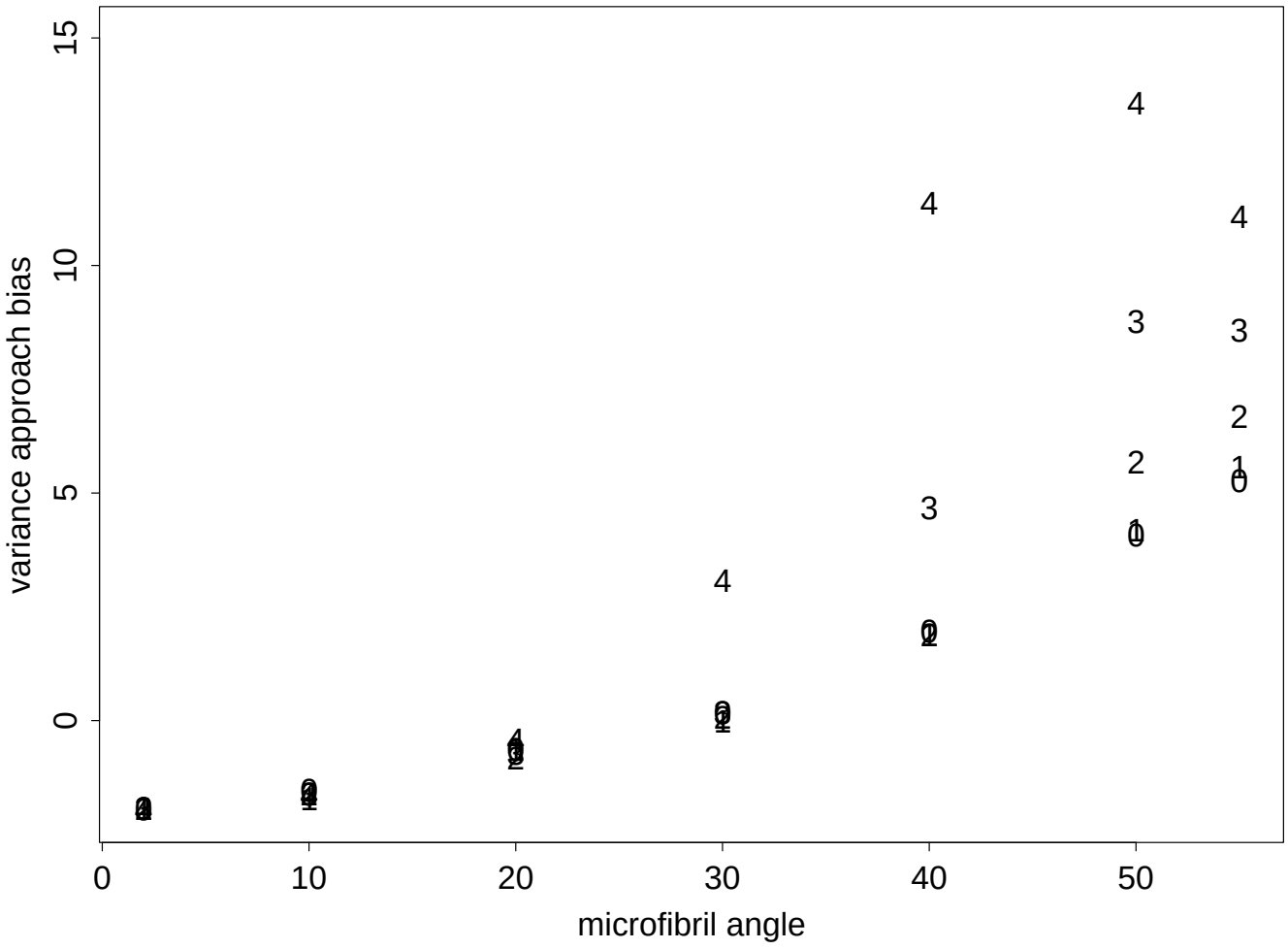

Figure 29: Variance approach bias versus true microfibril angle. **90 degree rotation**. 0 - 0 degree tilt. 1 - 10 degree tilt. 2 - 20 degree tilt. 3 - 30 degree tilt. 4 - 40 degree tilt. **Practical biases.** Profiles combined. Hexagonal cell cross-section.

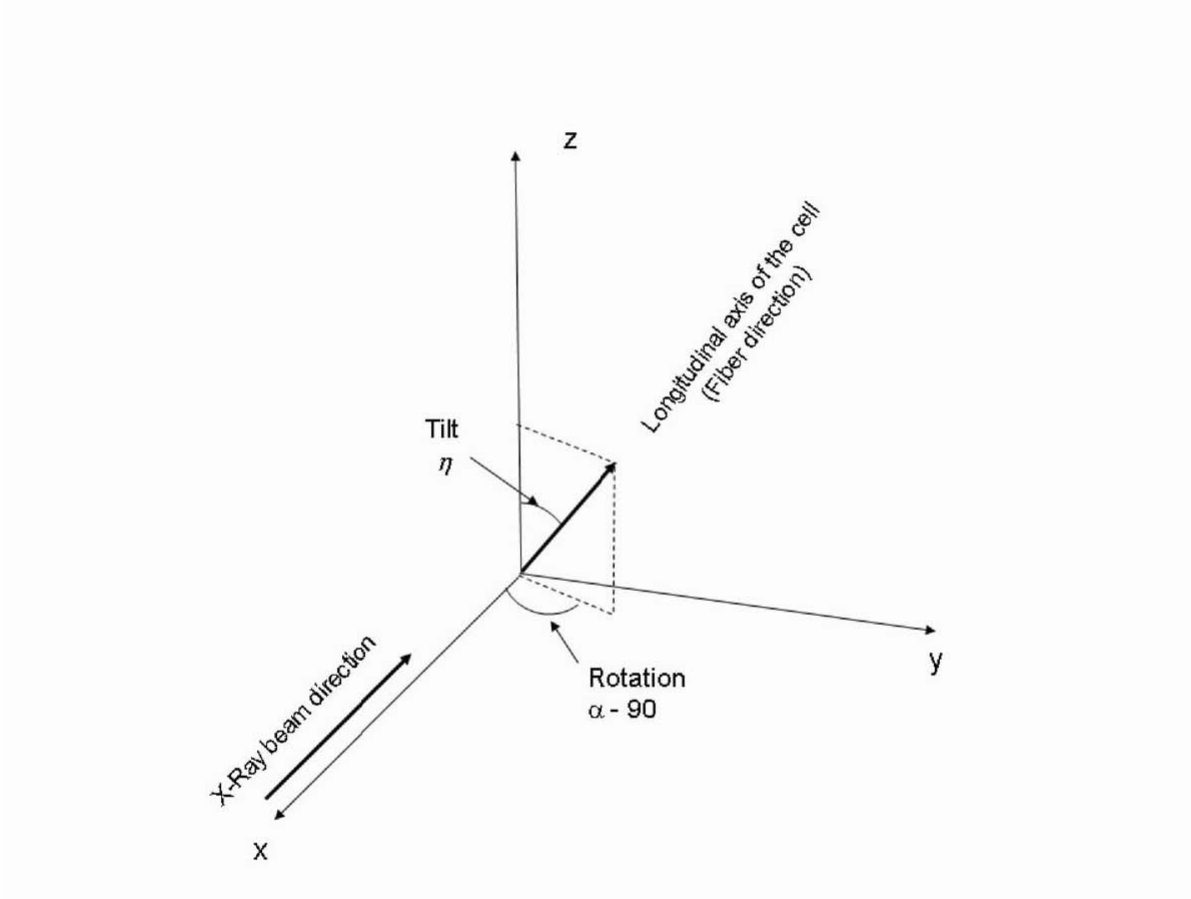

Figure 30: η tilt and $\alpha - 90$ rotation of the wood cell. (Recall that the "fiber direction" differs from the "microfibril direction". The microfibrils are wrapped in a helical manner about a wood cell.)

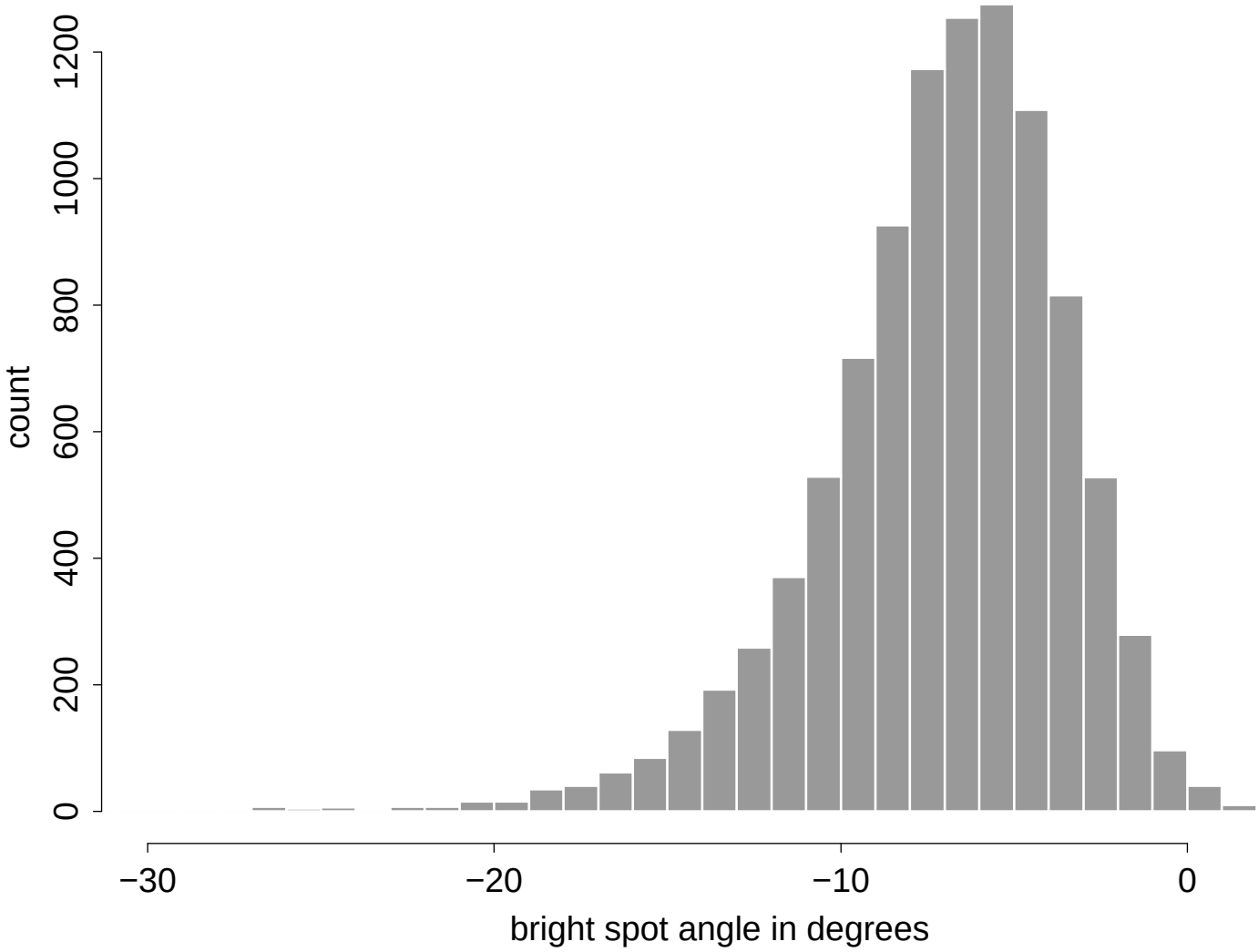

Figure 31: Histogram of the broadened left profile bright spot associated with the left face of a rectangular wood cell when cell rotation = 0 degrees, cell tilt = 0 degrees, and MFA = 30 degrees. The skewness of this distribution is -1.28. This figure was generated by calculating the left profile, left face bright spot locations associated with 10,000 MFA draws from a Gaussian distribution centered at 30 degrees, with variance $6^2 + (30/3)^2$.

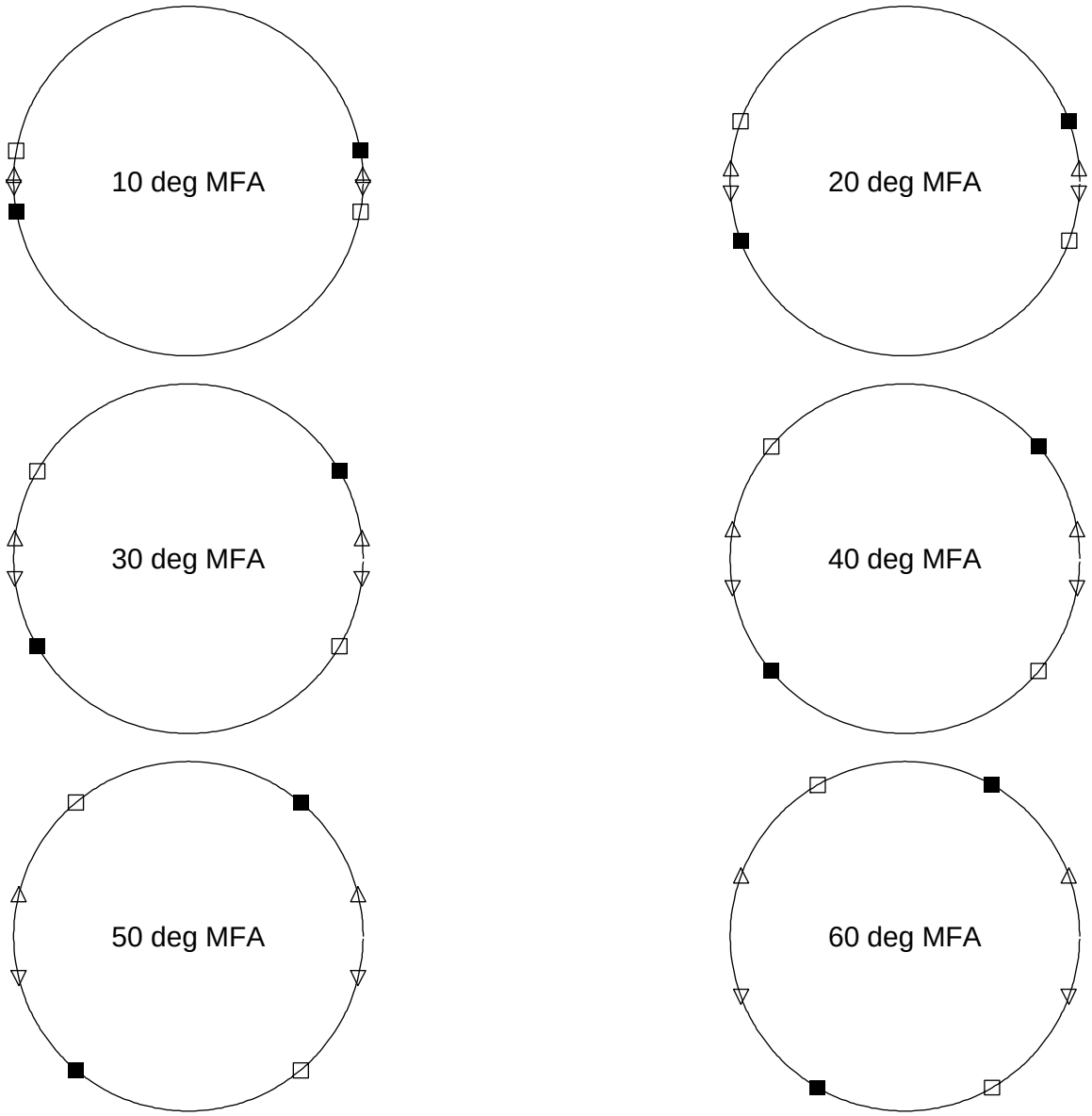

Figure 32: Locations of high intensity X-ray spots on the back plane for wood cell tilt = 0 degrees and wood cell rotation = 0 degrees

□ — spots due to the **front** (before tilt and rotation) face
■ — spots due to the **back** face
△ — spots due to the **right** face
▽ — spots due to the **left** face

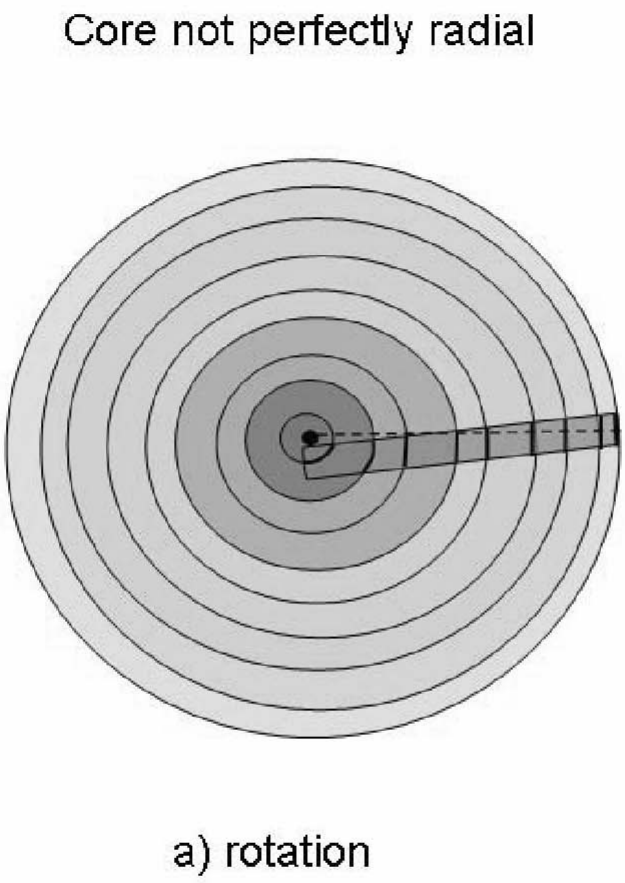

Figure 33: a) Cell rotation caused by a non-perfectly radial core

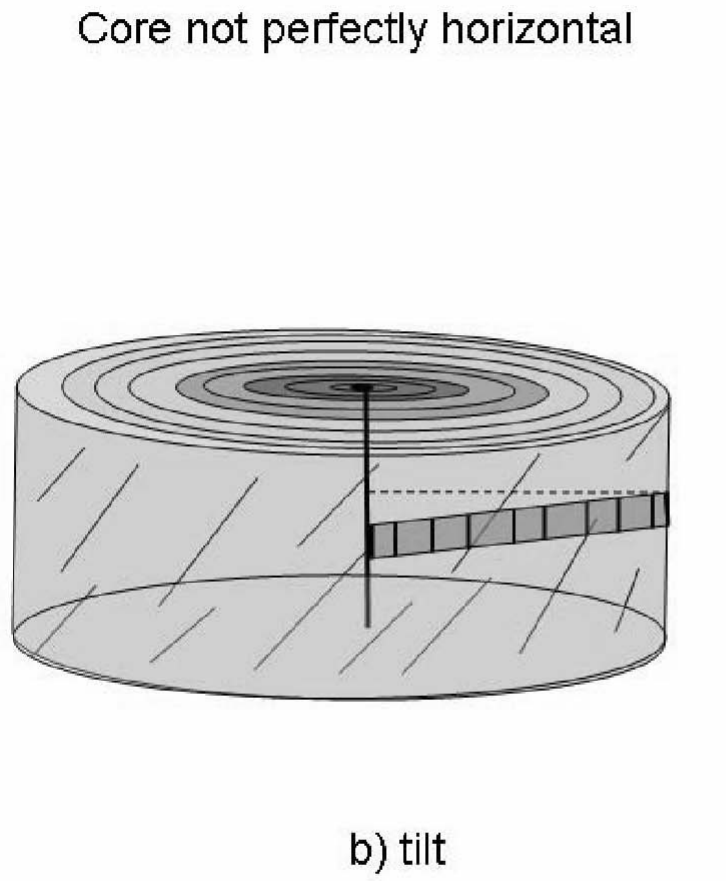

Figure 33: b) Cell alpha tilt due to a non-perfectly horizontal core

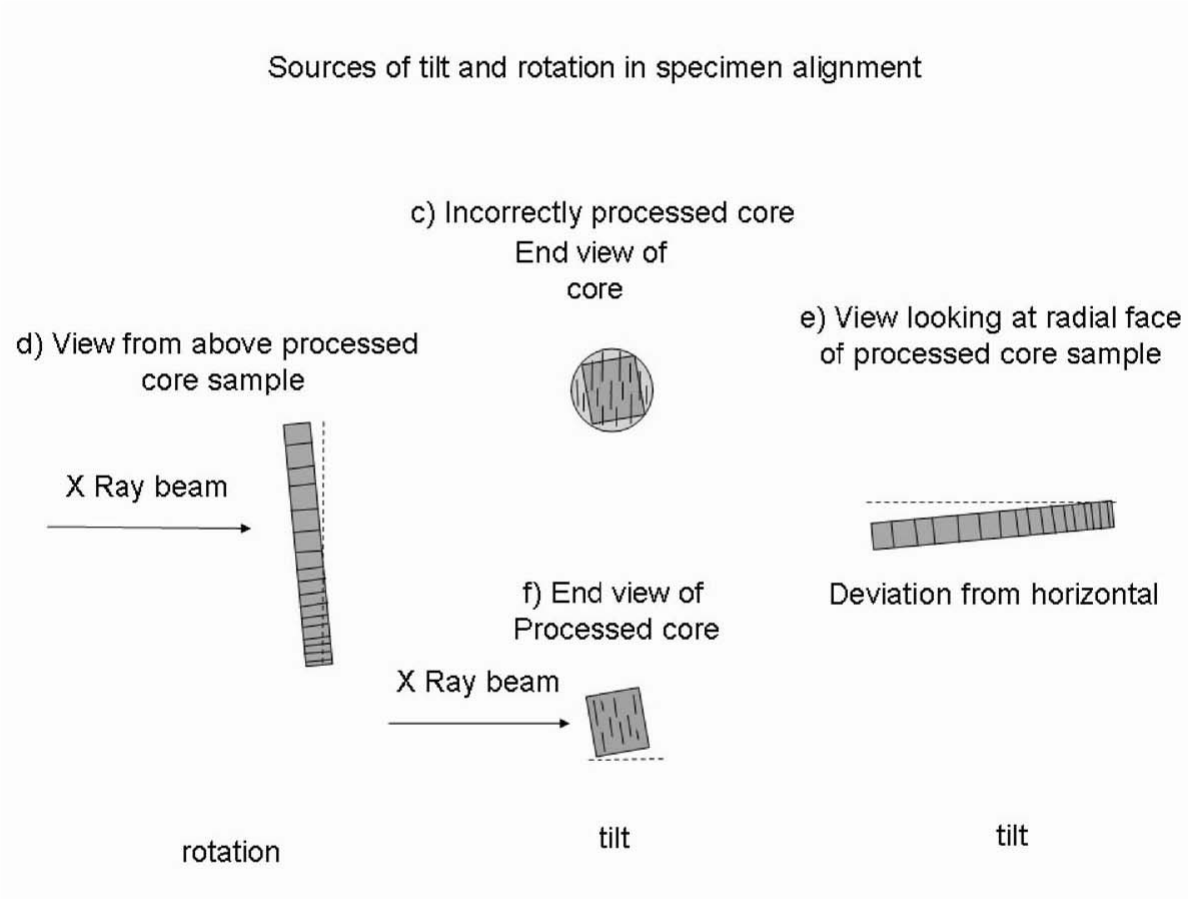

Figure 33: c-f) Cell rotation and alpha and beta tilts caused by incorrect processing of the core and by mis-alignment of the processed core

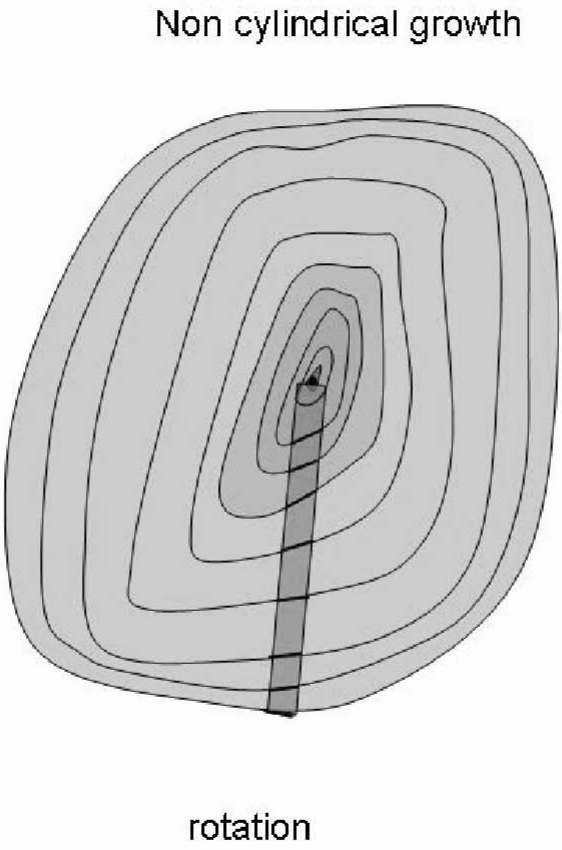

Figure 34: a) Cell rotation caused by non-cylindrical growth

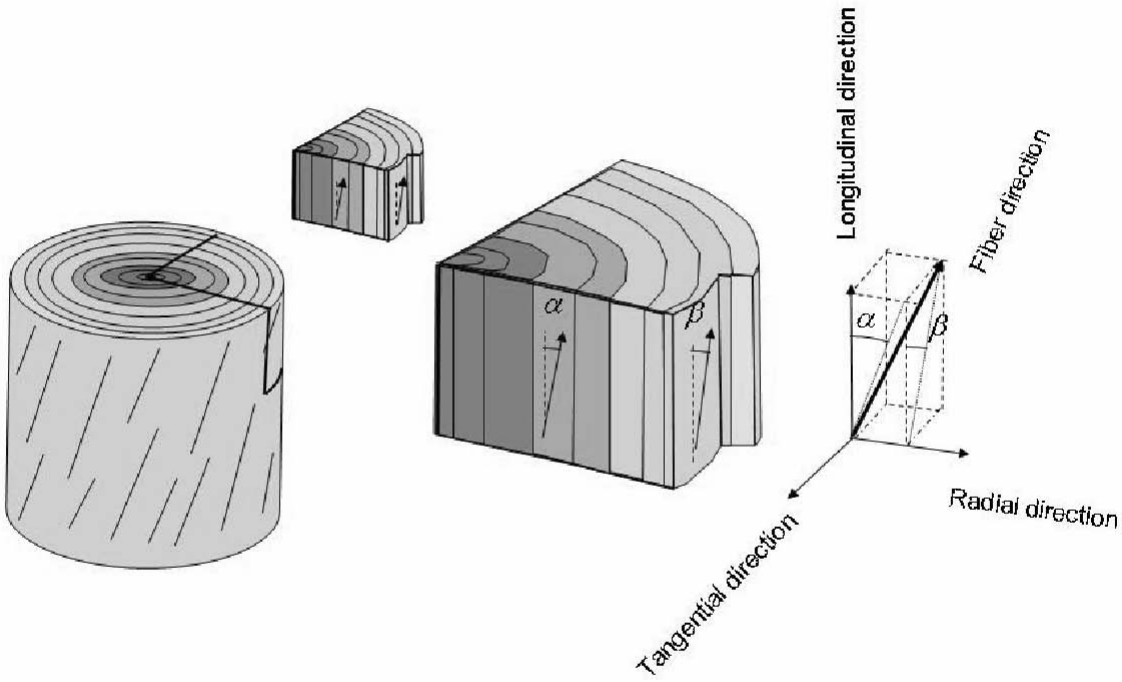

Figure 34: b) Natural alpha and beta (spiral growth) tilts

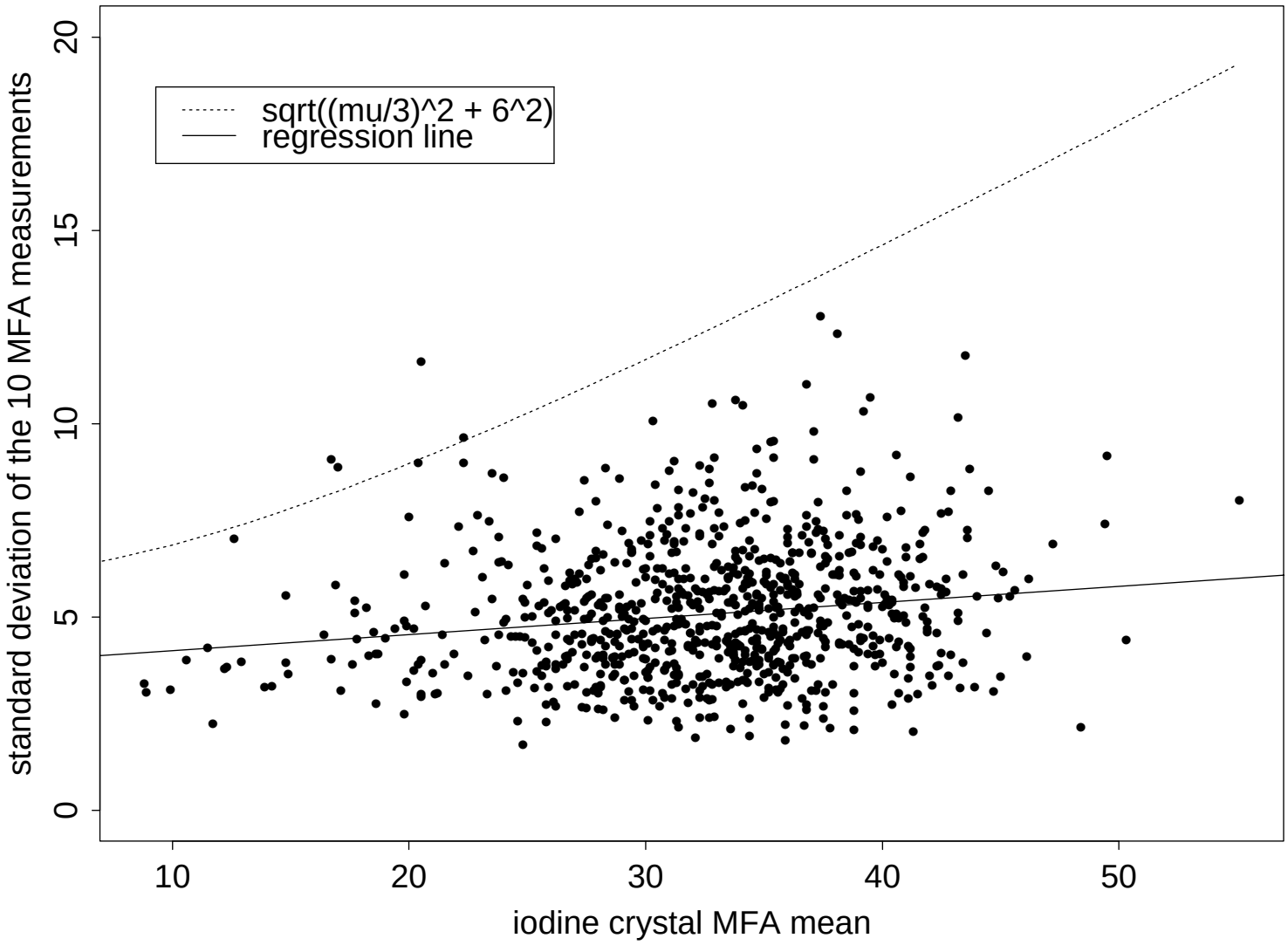

Figure 35: Microfibril angle standard deviation versus microfibril angle. Harry Alden's iodine crystallization data.

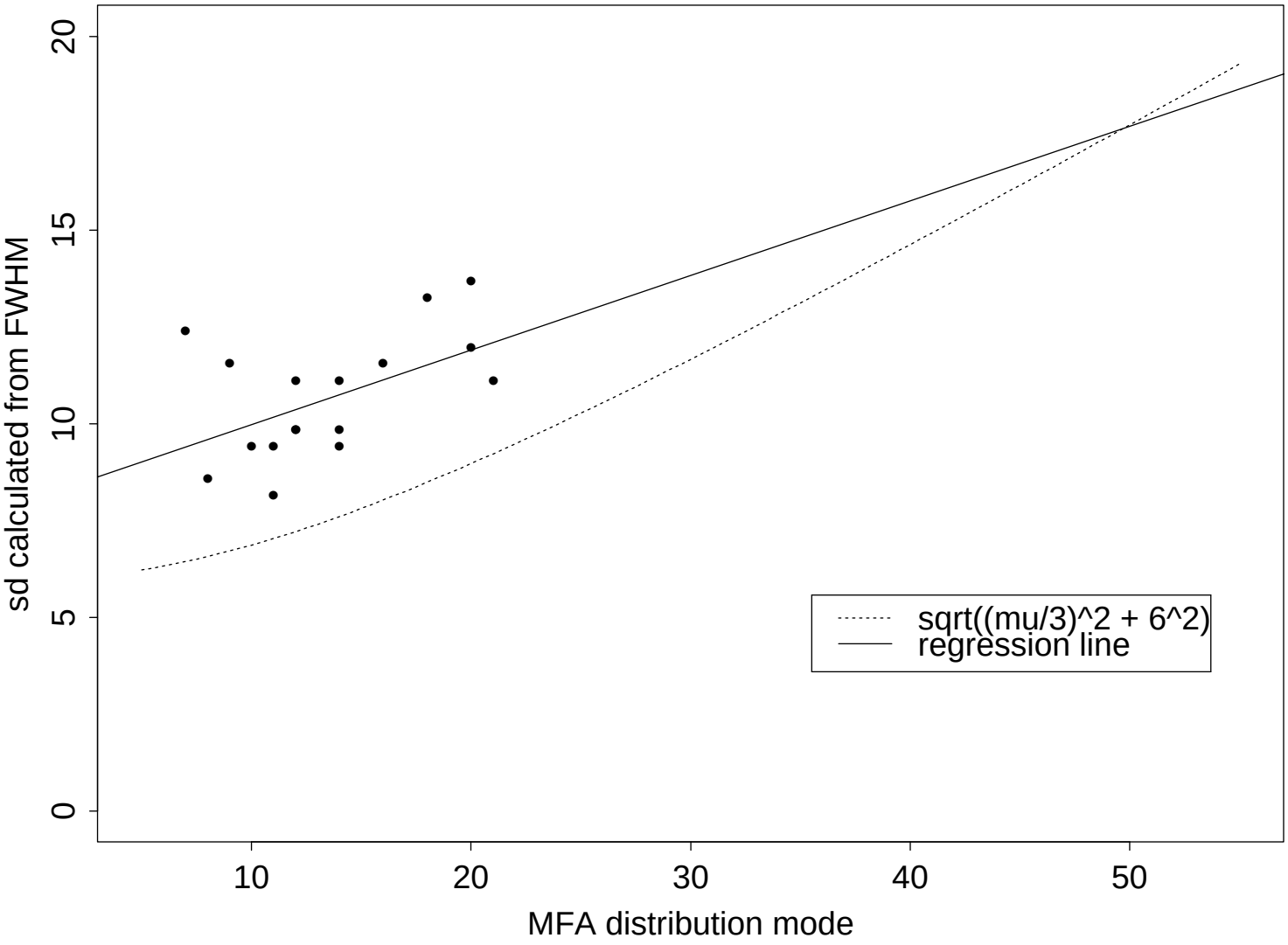

Figure 36: Single cell microfibril angle standard deviation (calculated from full width at half maximum values) versus mode of the single cell microfibril angle distribution. Values from 17 cells (1 obscured). Peura *et al.* (2008a).

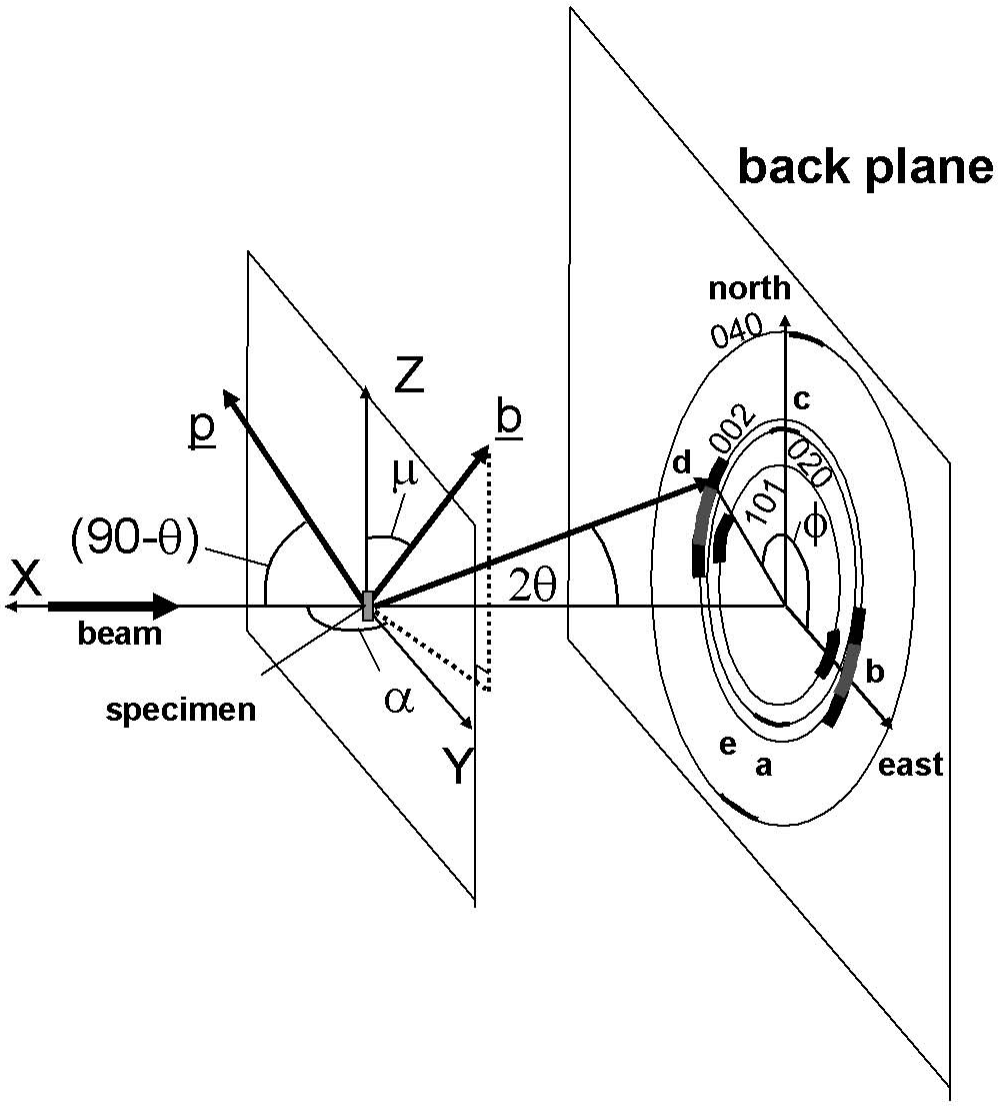

Figure 37: Geometry of the X-ray diffraction. The microfibril angle, μ, and the rotation, $\alpha - 90$ are non-zero in this figure, but the tilt, η, is zero. See Figure 30 for a non-zero tilt.

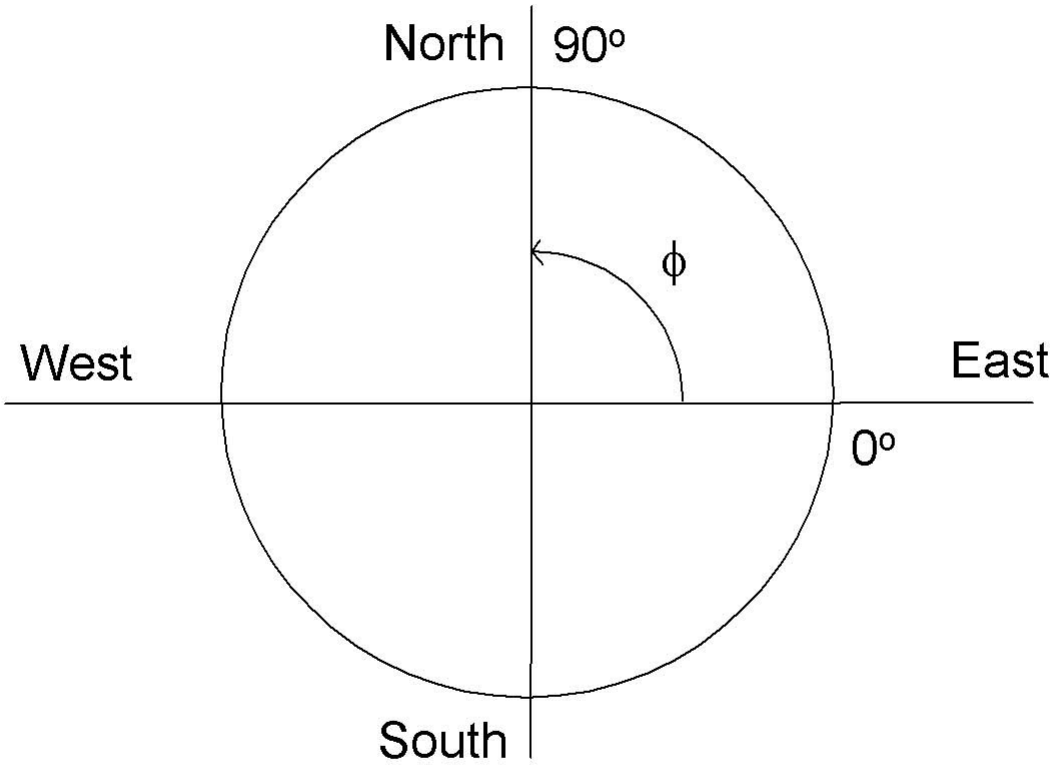

Figure 38: Back plane circle

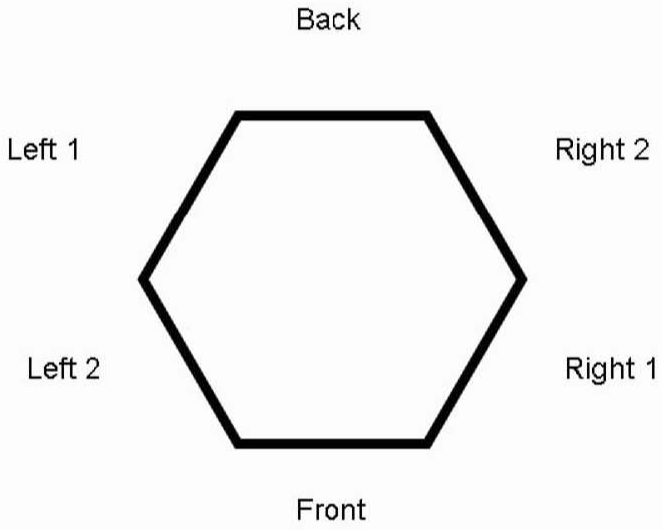

Figure 39: Definitions of the Front, Right 1, Right 2, Back, Left 1, and Left 2 faces of a cell with a hexagonal cross-section

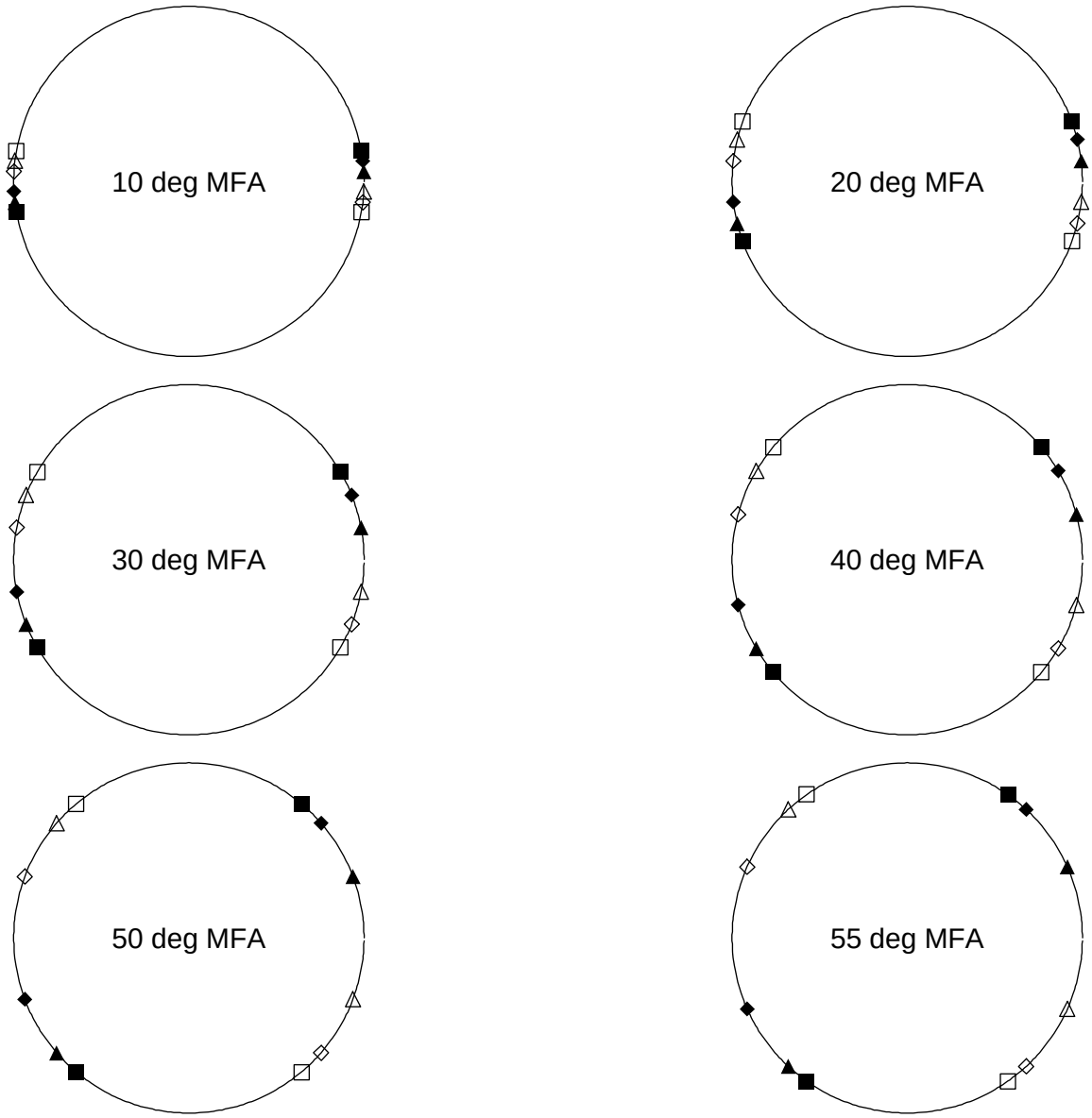

Figure 40: Locations of high-intensity X-ray spots on the back plane for a hexagonal cross section, a wood cell tilt of 0 degrees, and **wood cell rotation = 0 degrees.**

□ — spots due to the **front** (before tilt and rotation) face
■ — spots due to the **back** face
△ — spots due to the **right 1** face
▲ — spots due to the **left 1** face
◇ — spots due to the **left 2** face
◆ — spots due to the **right 2** face

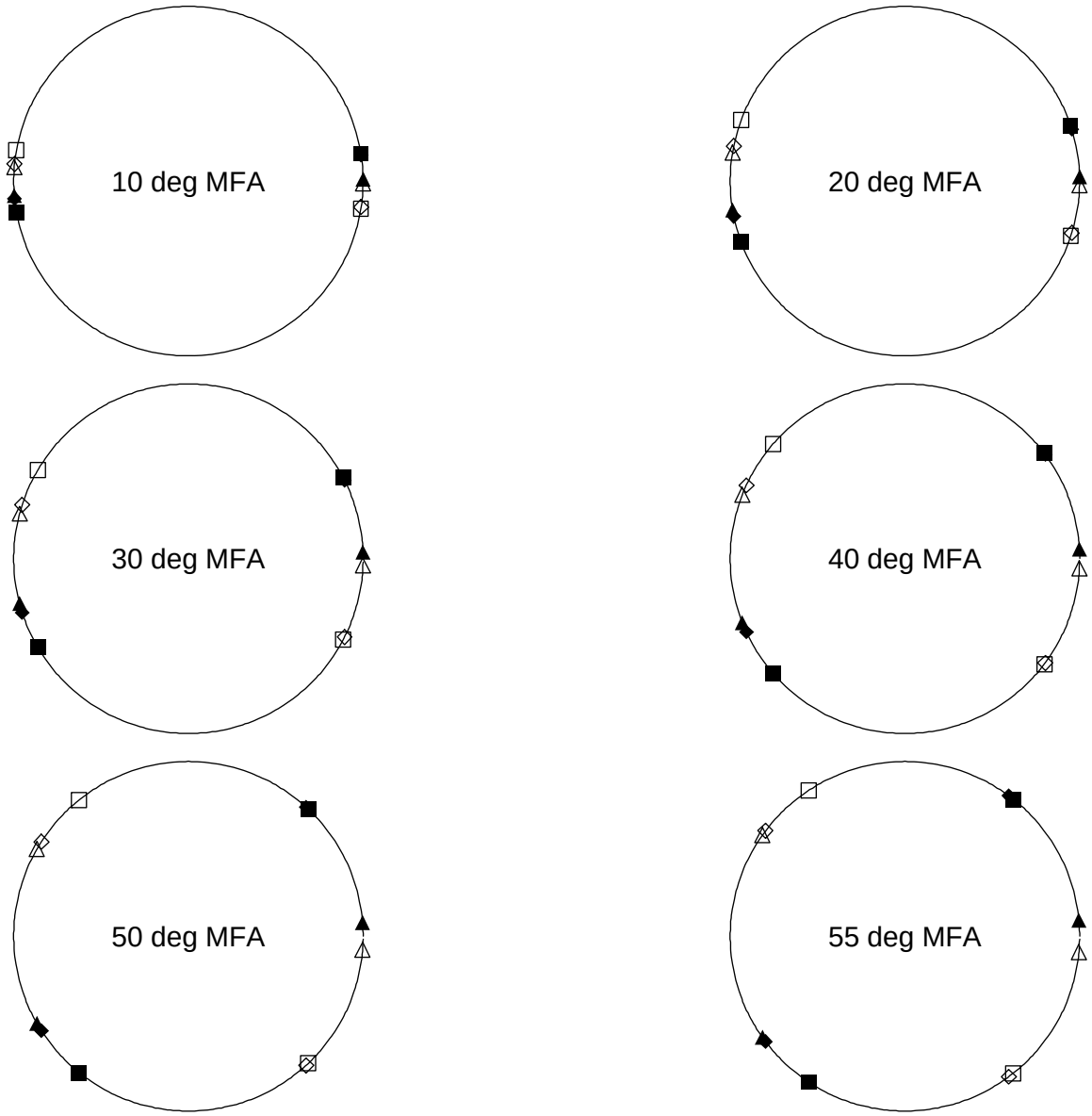

Figure 41: Locations of high-intensity X-ray spots on the back plane for a hexagonal cross section, a wood cell tilt of 0 degrees, and **wood cell rotation = 15 degrees.**

□ — spots due to the **front** (before tilt and rotation) face
■ — spots due to the **back** face
△ — spots due to the **right 1** face
▲ — spots due to the **left 1** face
◊ — spots due to the **left 2** face
⧫ — spots due to the **right 2** face

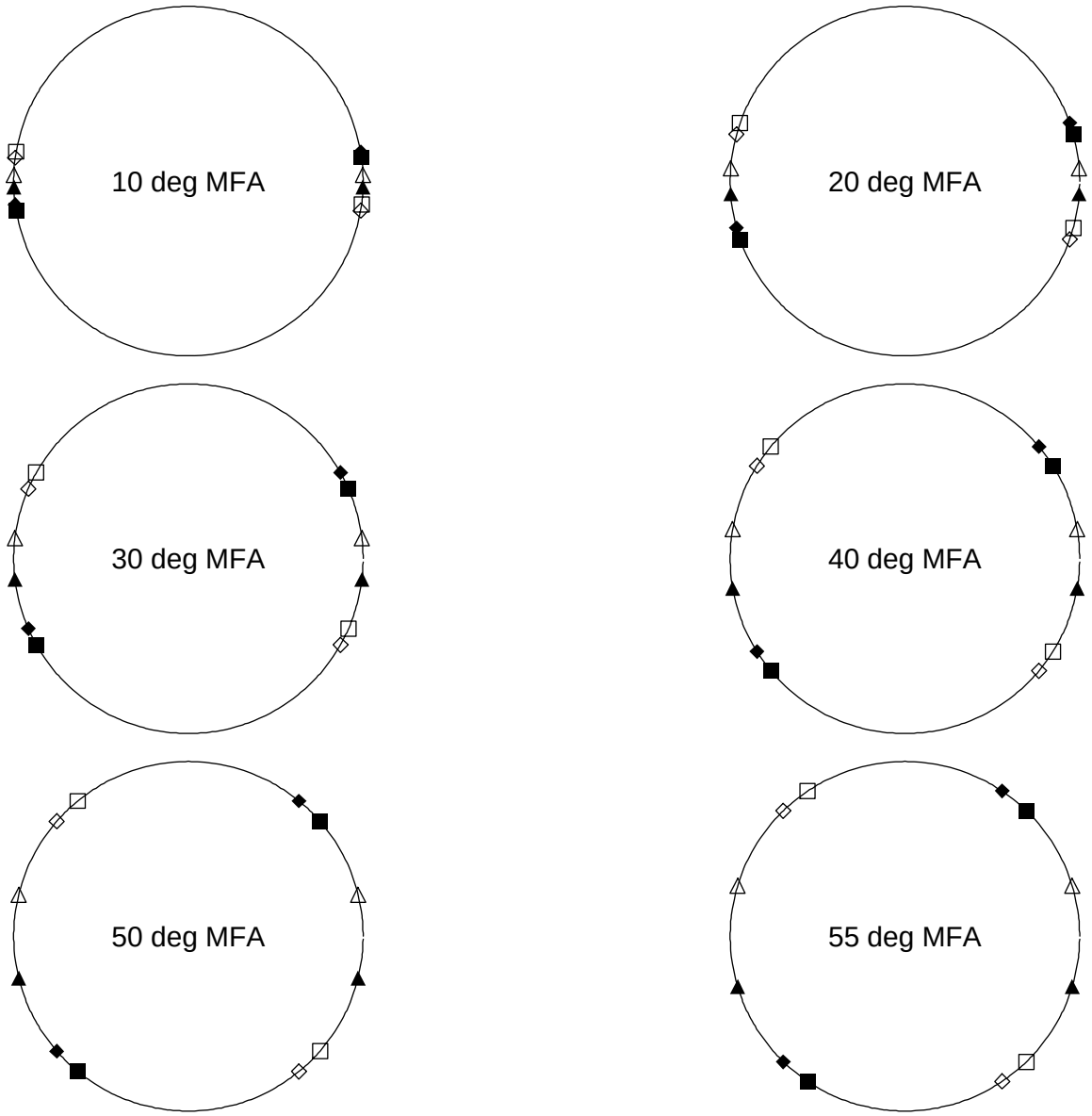

Figure 42: Locations of high-intensity X-ray spots on the back plane for a hexagonal cross section, a wood cell tilt of 0 degrees, and **wood cell rotation = 30 degrees.**

□ — spots due to the **front** (before tilt and rotation) face
■ — spots due to the **back** face
△ — spots due to the **right 1** face
▲ — spots due to the **left 1** face
◊ — spots due to the **left 2** face
⧫ — spots due to the **right 2** face

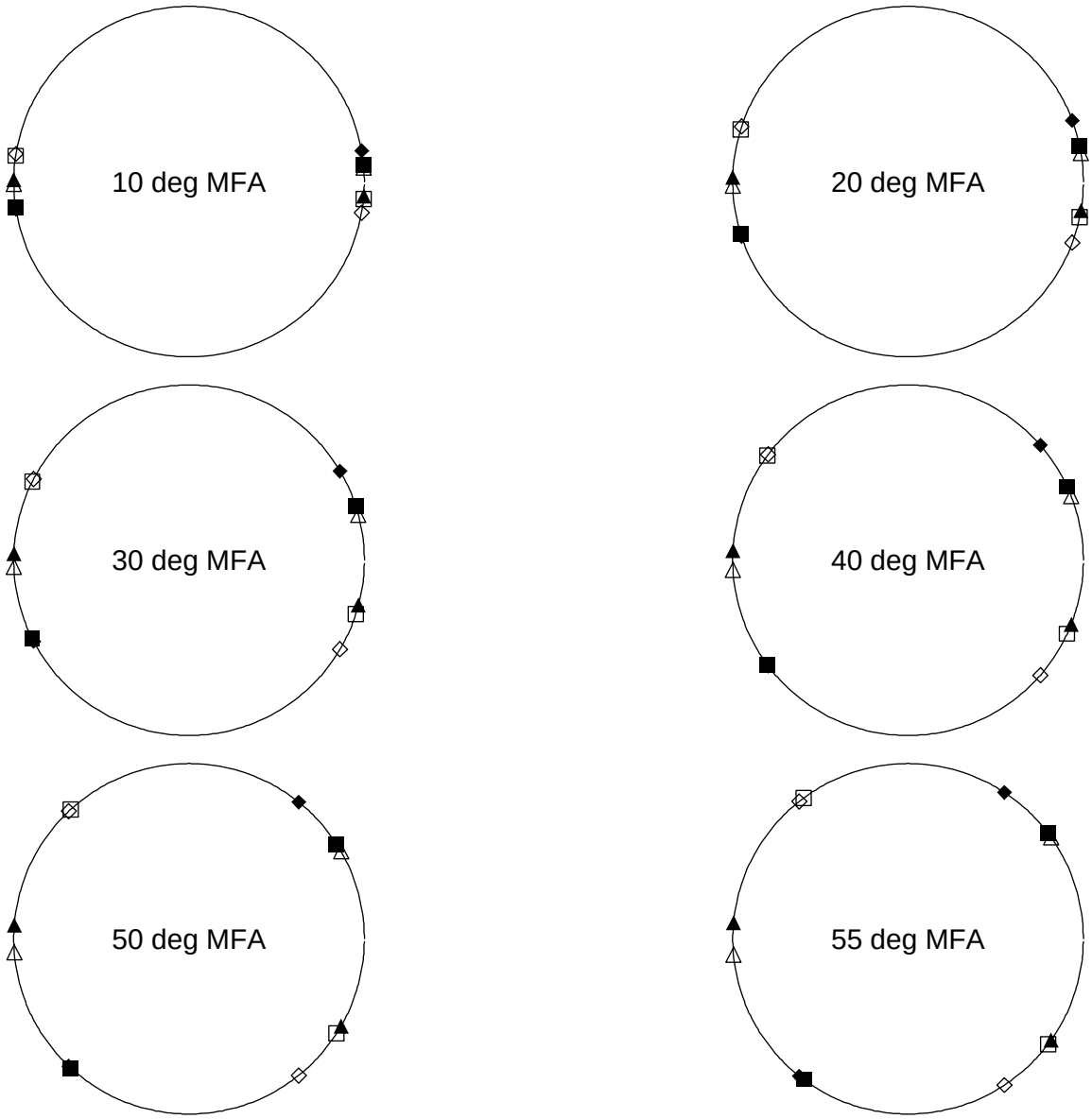

Figure 43: Locations of high-intensity X-ray spots on the back plane for a hexagonal cross section, a wood cell tilt of 0 degrees, and **wood cell rotation = 45 degrees.**

□ — spots due to the **front** (before tilt and rotation) face
■ — spots due to the **back** face
△ — spots due to the **right 1** face
▲ — spots due to the **left 1** face
◊ — spots due to the **left 2** face
⧫ — spots due to the **right 2** face

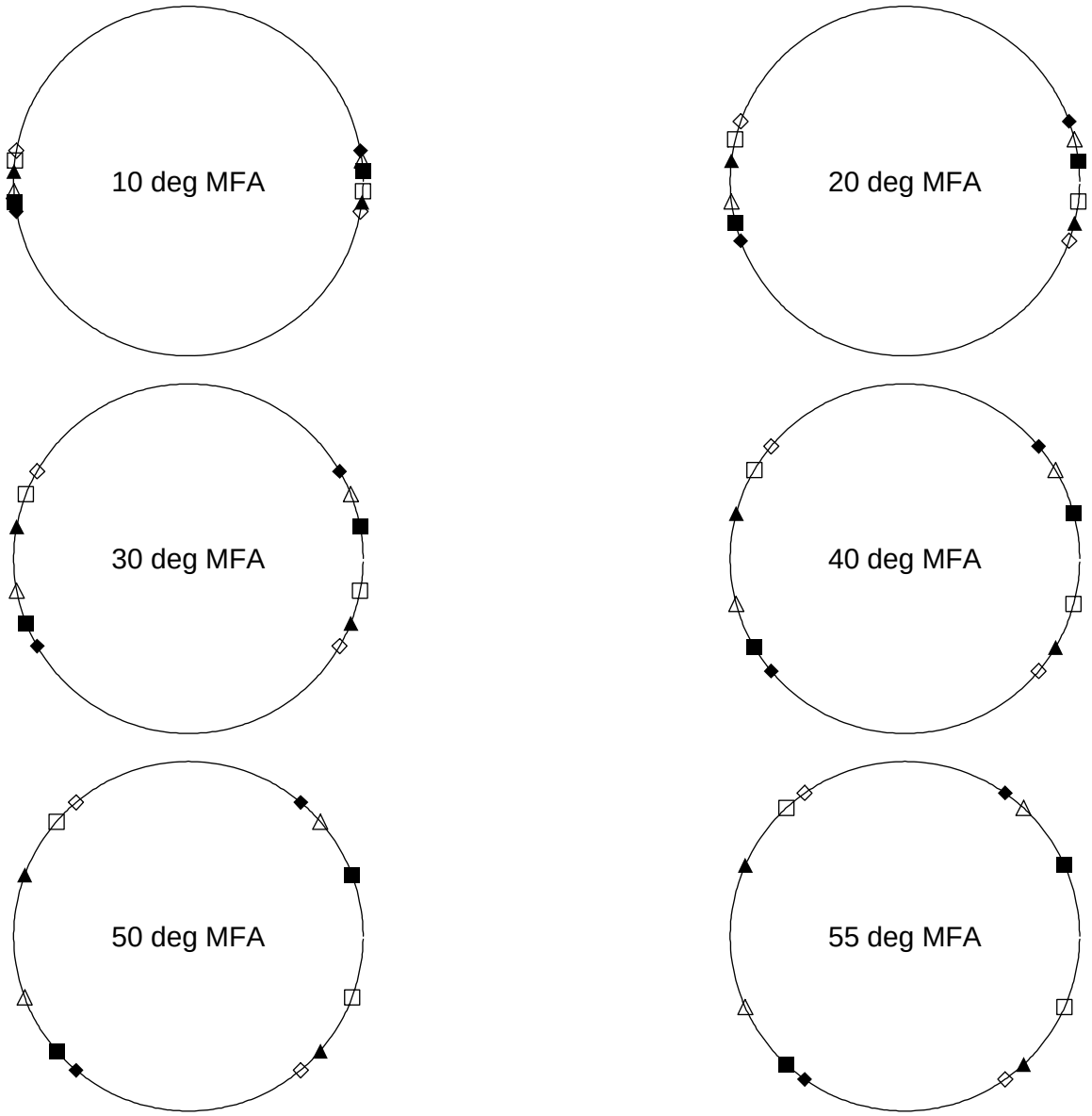

Figure 44: Locations of high-intensity X-ray spots on the back plane for a hexagonal cross section, a wood cell tilt of 0 degrees, and **wood cell rotation = 60 degrees.**

□ — spots due to the **front** (before tilt and rotation) face
■ — spots due to the **back** face
△ — spots due to the **right 1** face
▲ — spots due to the **left 1** face
◊ — spots due to the **left 2** face
⧫ — spots due to the **right 2** face

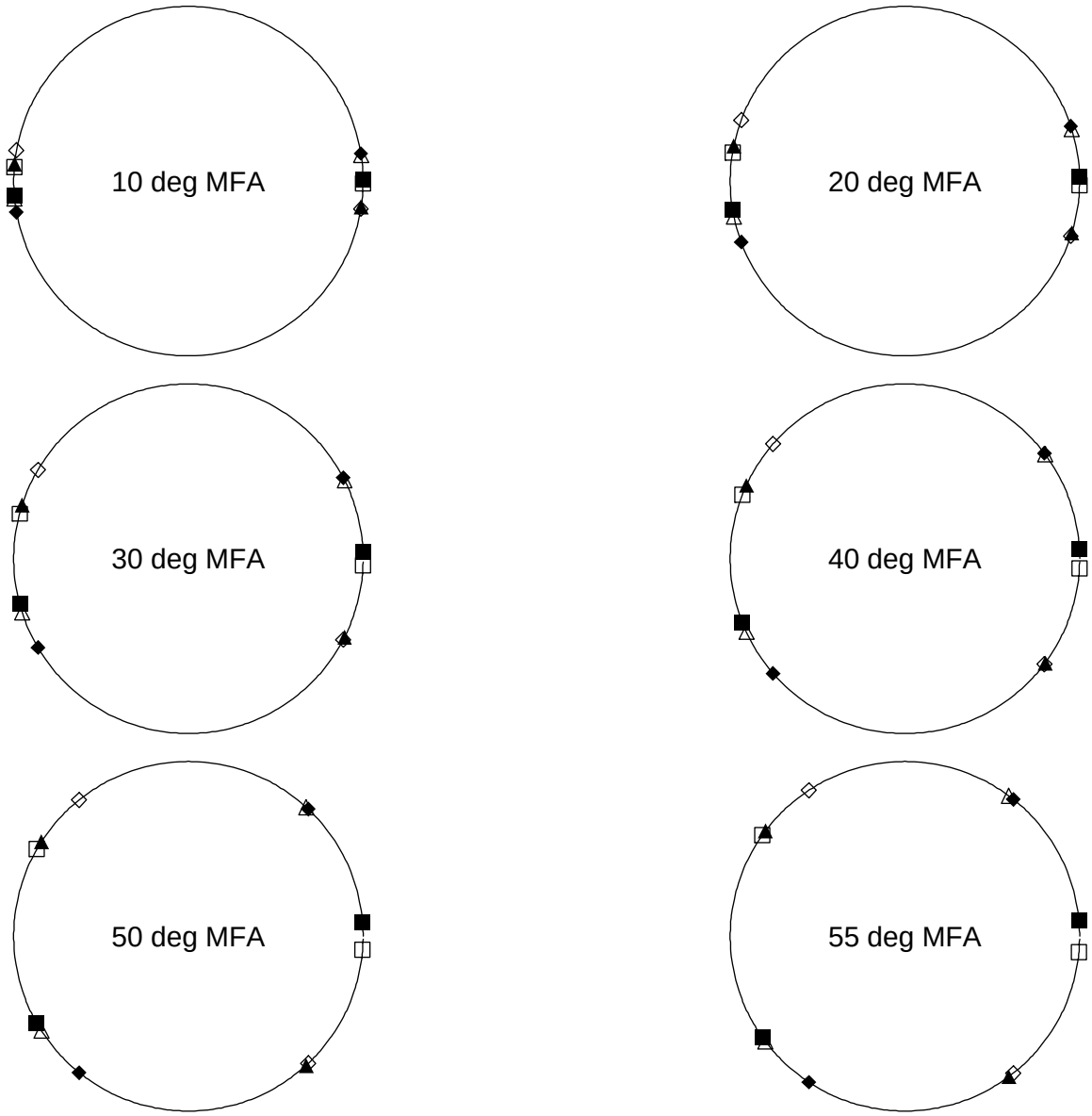

Figure 45: Locations of high-intensity X-ray spots on the back plane for a hexagonal cross section, a wood cell tilt of 0 degrees, and **wood cell rotation = 75 degrees.**

□ — spots due to the **front** (before tilt and rotation) face
■ — spots due to the **back** face
△ — spots due to the **right 1** face
▲ — spots due to the **left 1** face
◊ — spots due to the **left 2** face
⧫ — spots due to the **right 2** face

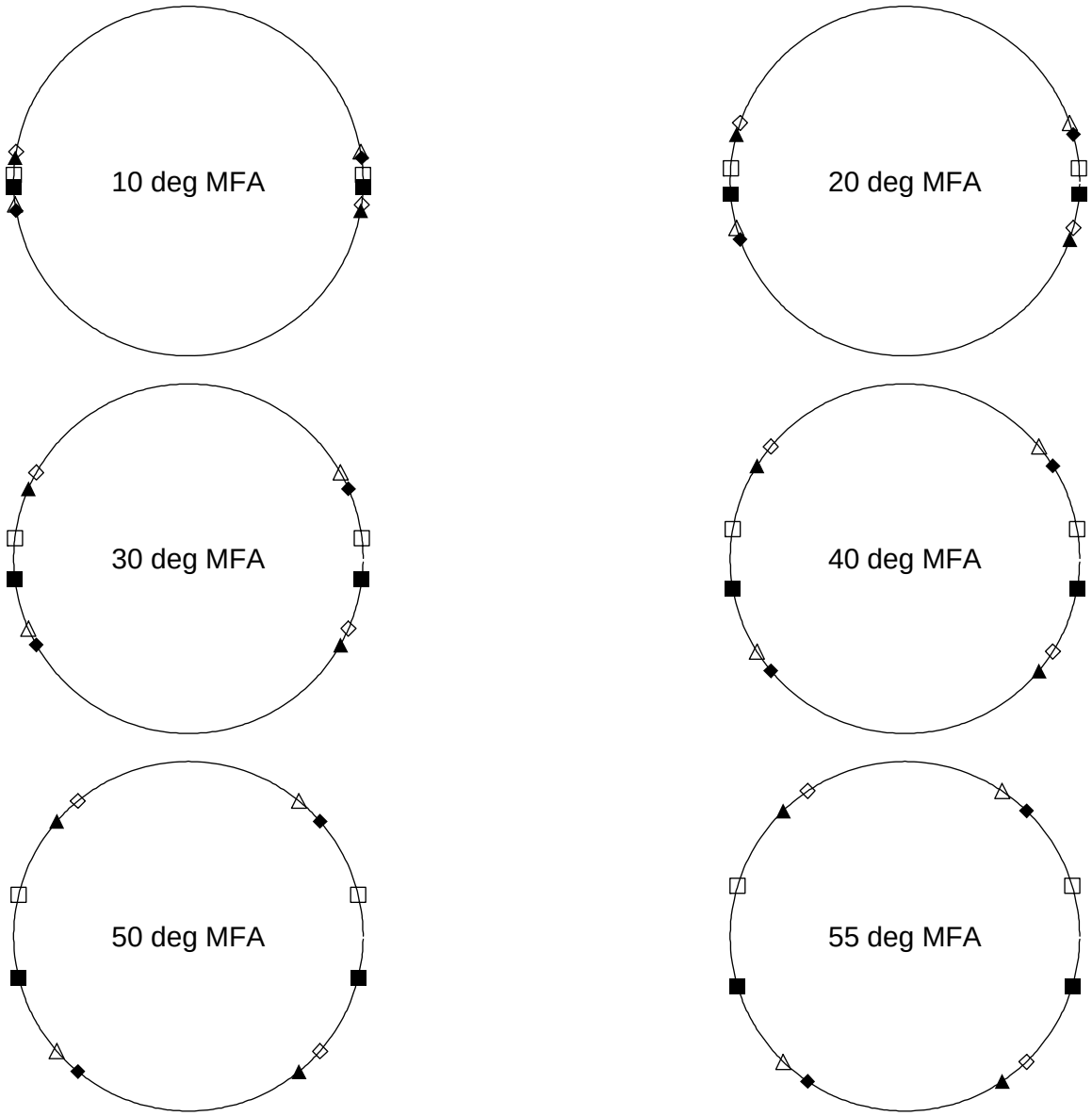

Figure 46: Locations of high-intensity X-ray spots on the back plane for a hexagonal cross section, a wood cell tilt of 0 degrees, and **wood cell rotation = 90 degrees.**

□ — spots due to the **front** (before tilt and rotation) face
■ — spots due to the **back** face
△ — spots due to the **right 1** face
▲ — spots due to the **left 1** face
◊ — spots due to the **left 2** face
⧫ — spots due to the **right 2** face

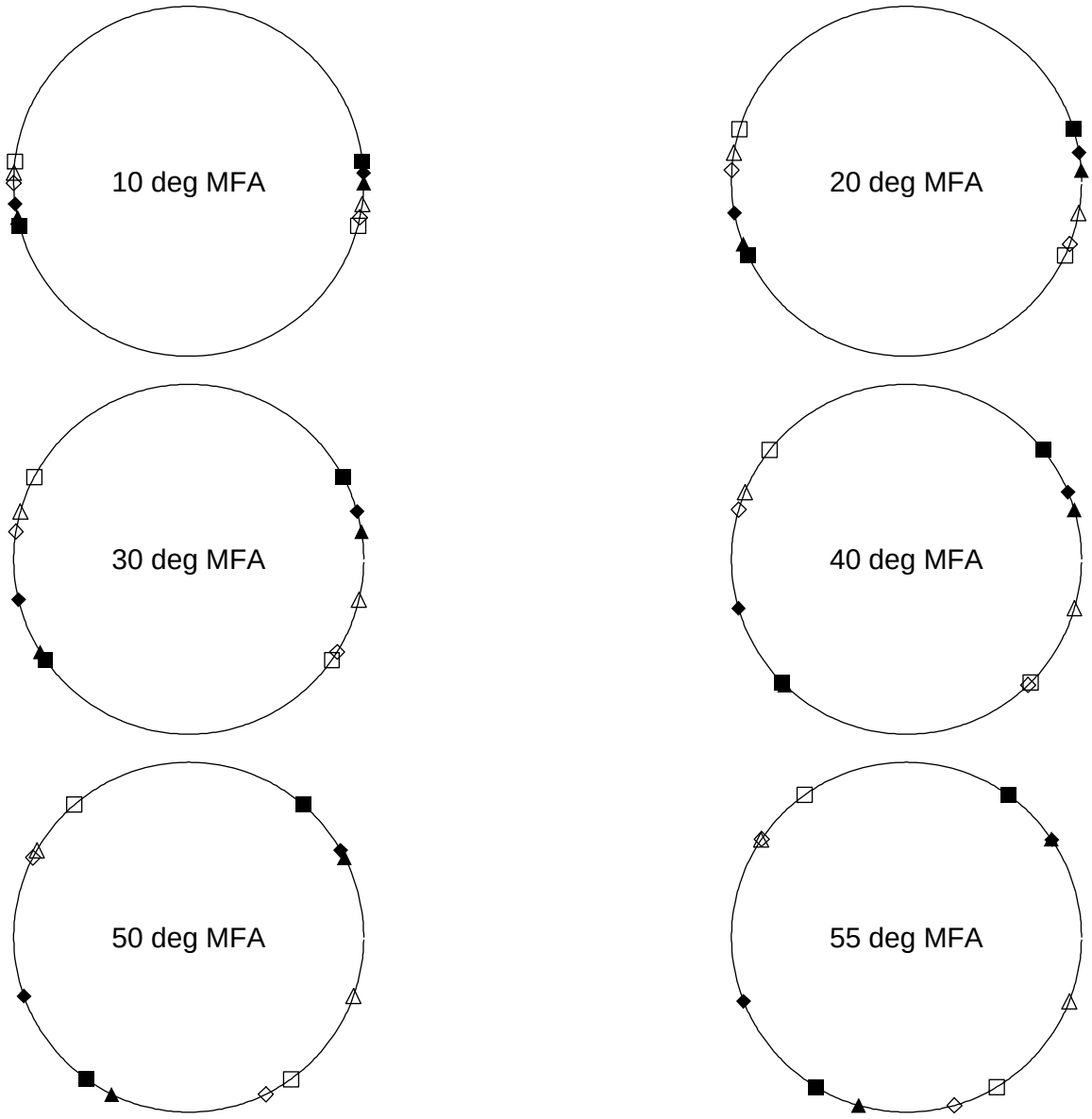

Figure 47: Locations of high-intensity X-ray spots on the back plane for a hexagonal cross section, a wood cell tilt of 20 degrees, and **wood cell rotation = 0 degrees.**

□ — spots due to the **front** (before tilt and rotation) face
■ — spots due to the **back** face
△ — spots due to the **right 1** face
▲ — spots due to the **left 1** face
◇ — spots due to the **left 2** face
♦ — spots due to the **right 2** face

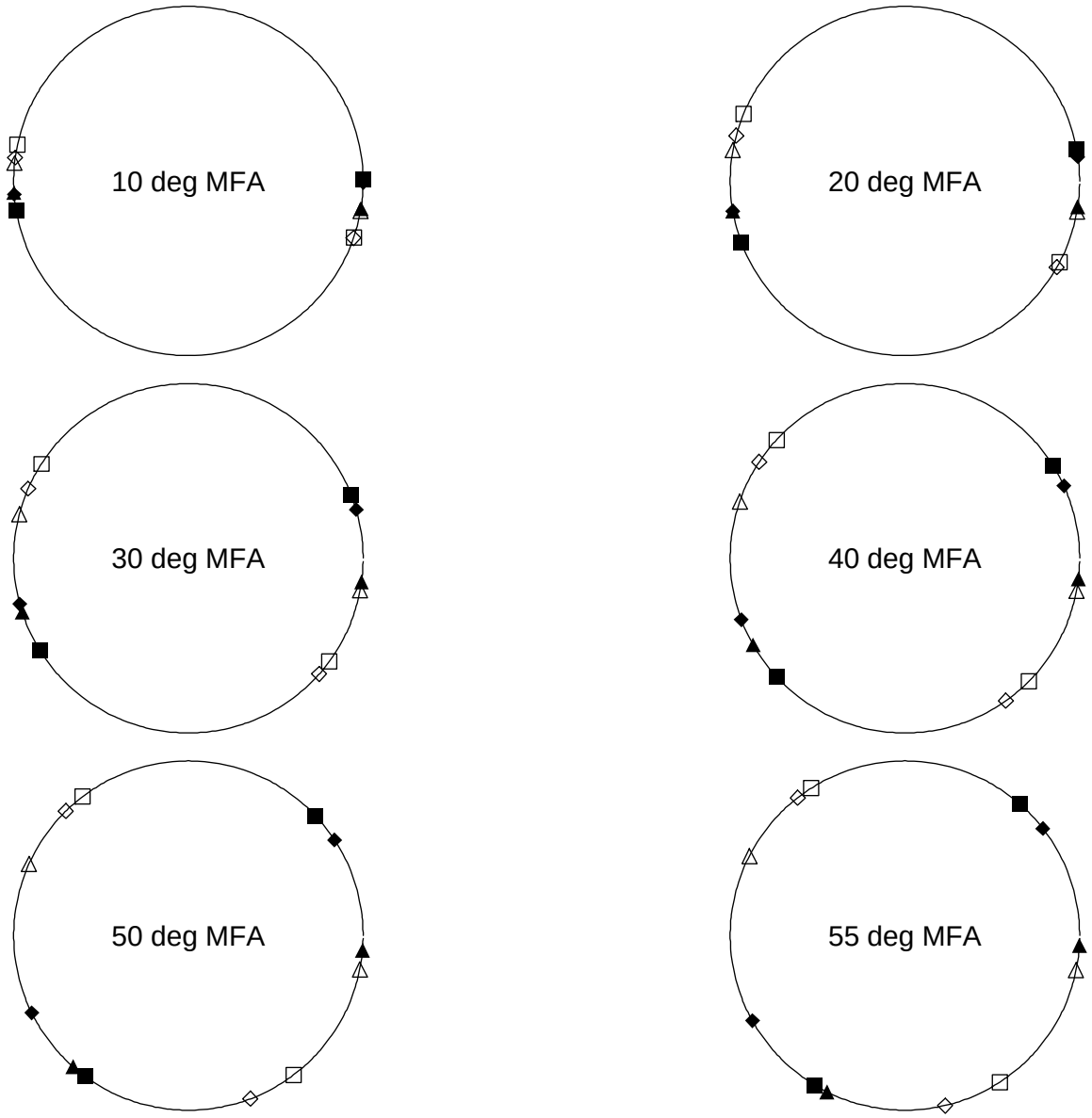

Figure 48: Locations of high-intensity X-ray spots on the back plane for a hexagonal cross section, a wood cell tilt of 20 degrees, and **wood cell rotation = 15 degrees.**

□ — spots due to the **front** (before tilt and rotation) face
■ — spots due to the **back** face
△ — spots due to the **right 1** face
▲ — spots due to the **left 1** face
◊ — spots due to the **left 2** face
⧫ — spots due to the **right 2** face

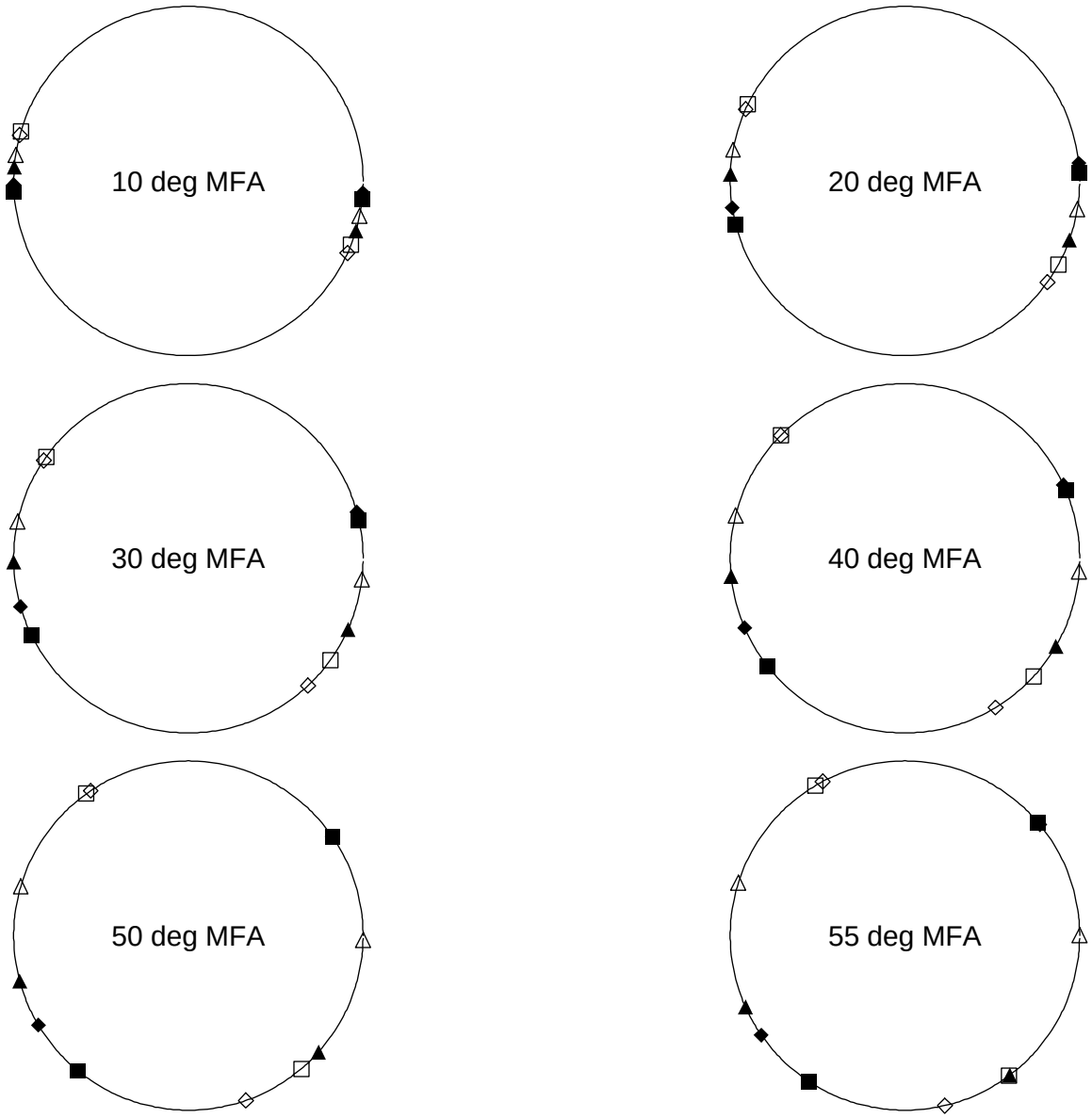

Figure 49: Locations of high-intensity X-ray spots on the back plane for a hexagonal cross section, a wood cell tilt of 20 degrees, and **wood cell rotation = 30 degrees.**

□ — spots due to the **front** (before tilt and rotation) face
■ — spots due to the **back** face
△ — spots due to the **right 1** face
▲ — spots due to the **left 1** face
◊ — spots due to the **left 2** face
⧫ — spots due to the **right 2** face

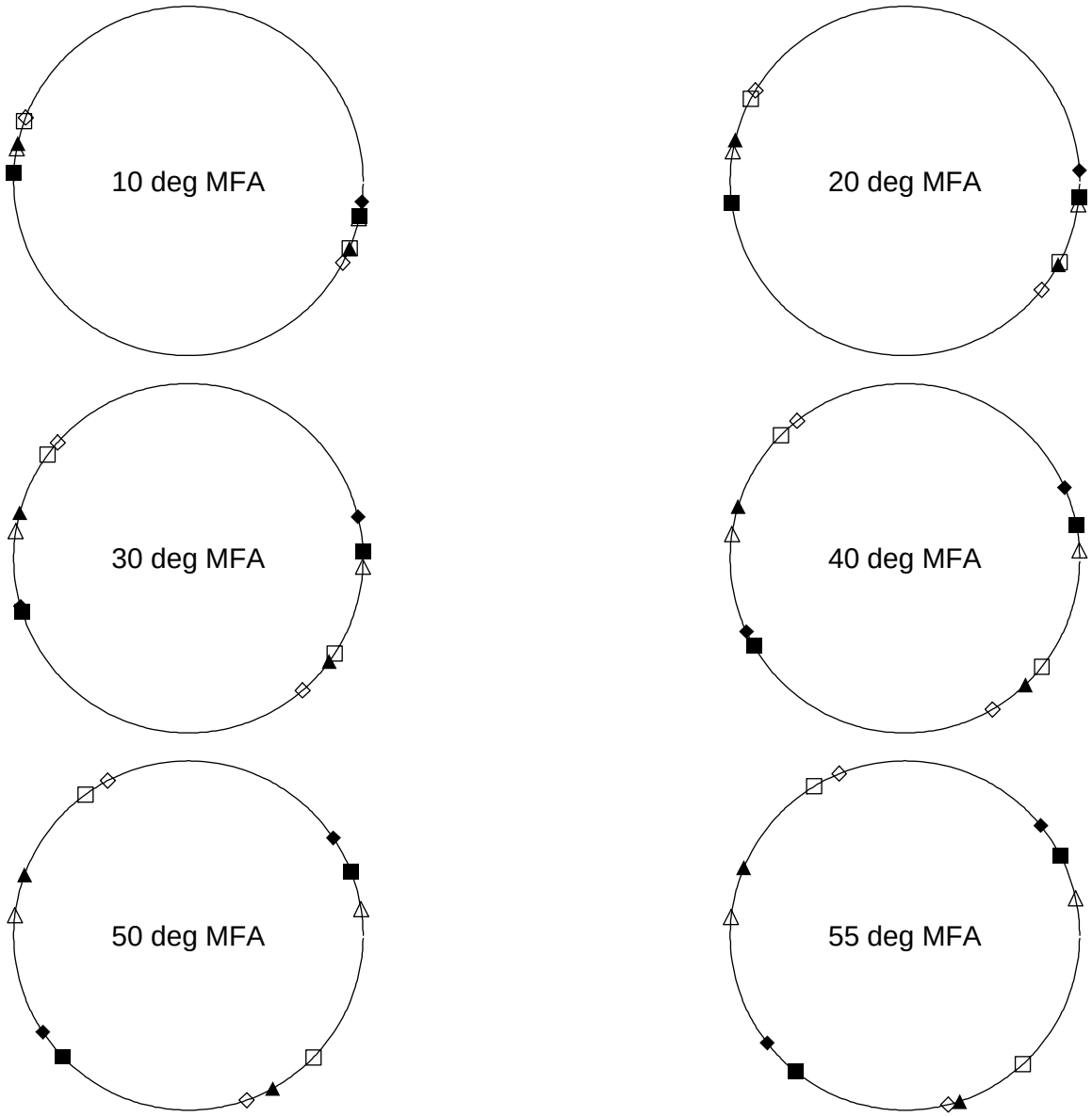

Figure 50: Locations of high-intensity X-ray spots on the back plane for a hexagonal cross section, a wood cell tilt of 20 degrees, and **wood cell rotation = 45 degrees.**

□ — spots due to the **front** (before tilt and rotation) face
■ — spots due to the **back** face
△ — spots due to the **right 1** face
▲ — spots due to the **left 1** face
◊ — spots due to the **left 2** face
⧫ — spots due to the **right 2** face

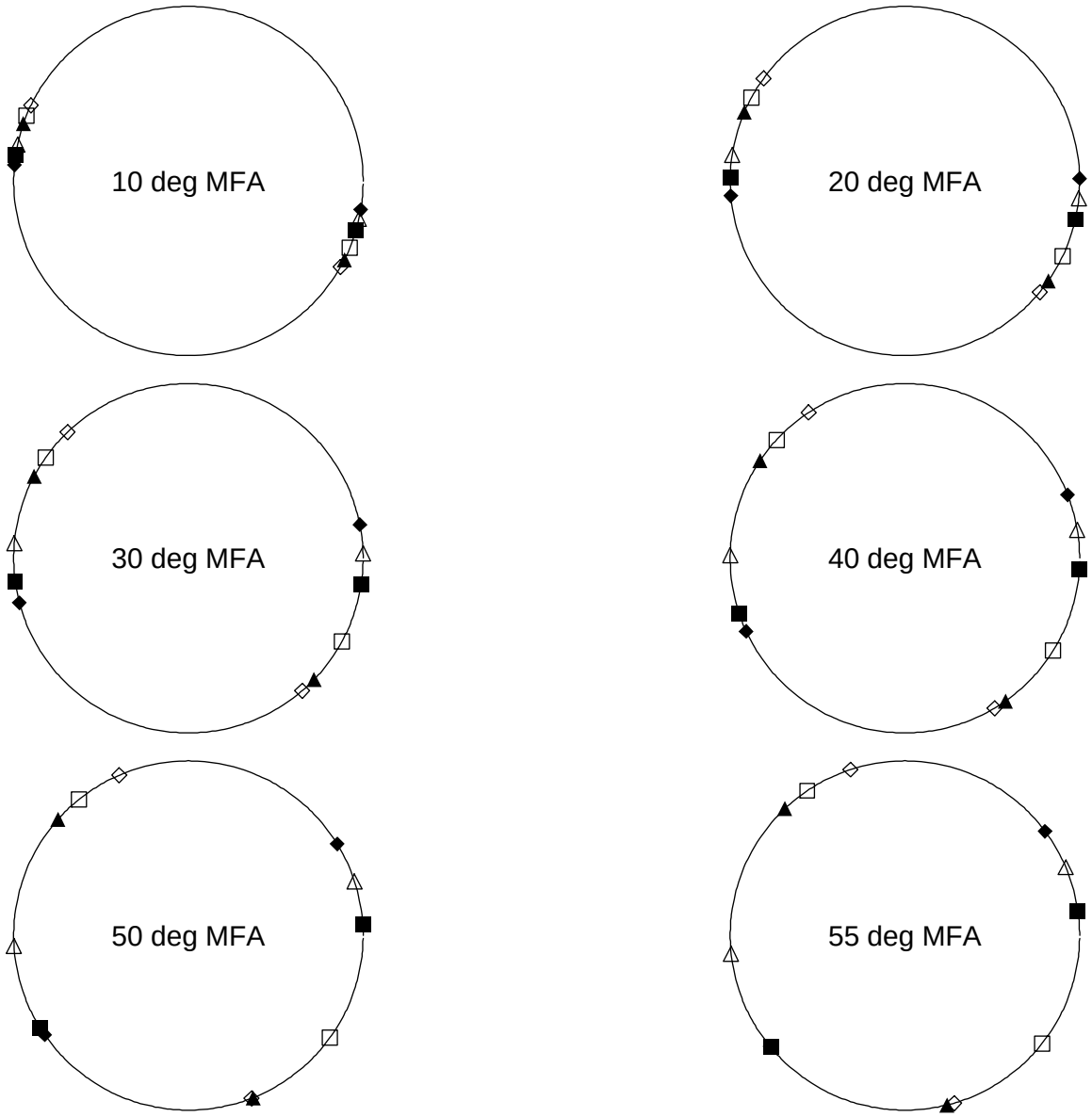

Figure 51: Locations of high-intensity X-ray spots on the back plane for a hexagonal cross section, a wood cell tilt of 20 degrees, and **wood cell rotation = 60 degrees.**

□ — spots due to the **front** (before tilt and rotation) face
■ — spots due to the **back** face
△ — spots due to the **right 1** face
▲ — spots due to the **left 1** face
◊ — spots due to the **left 2** face
⧫ — spots due to the **right 2** face

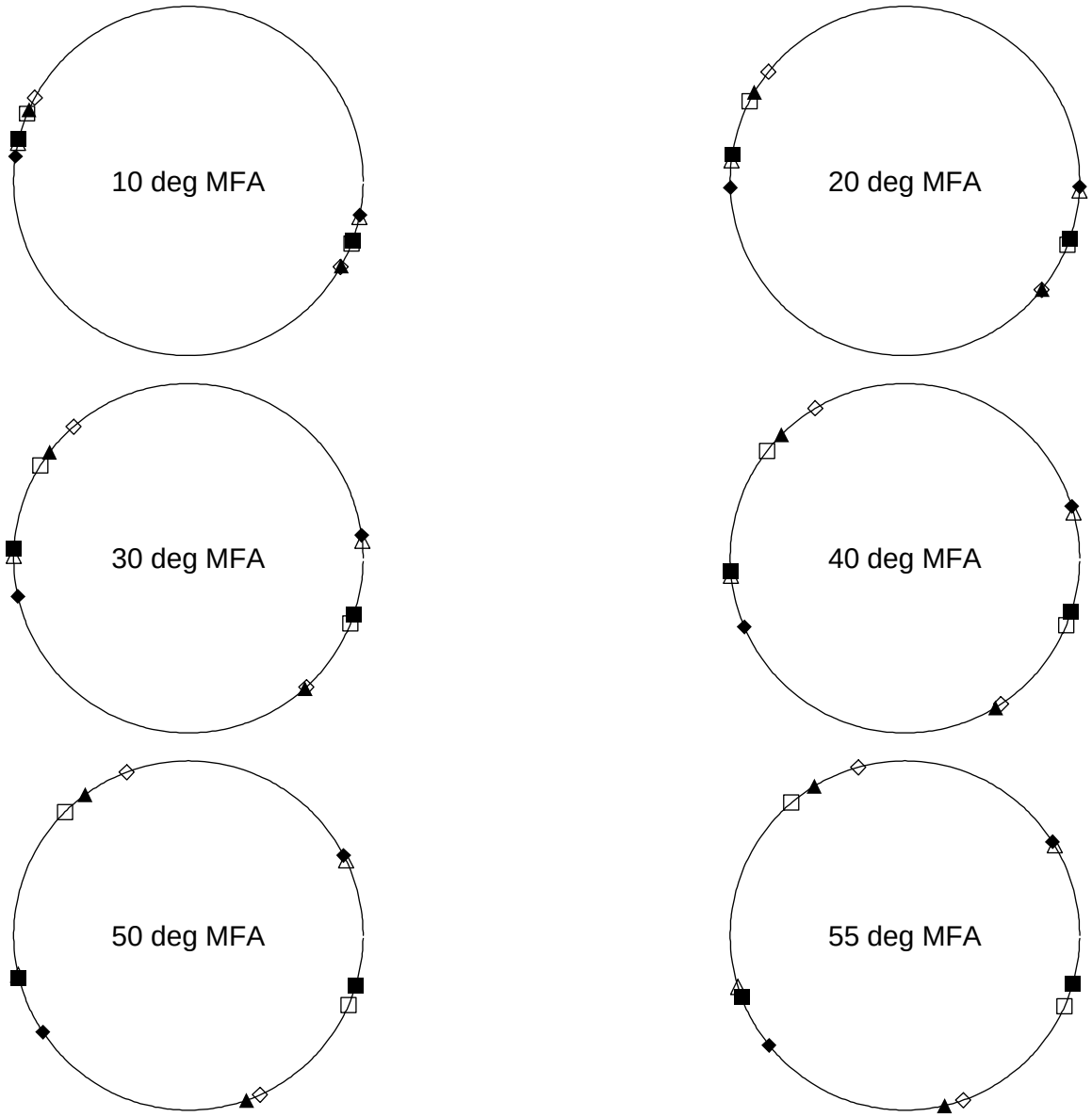

Figure 52: Locations of high-intensity X-ray spots on the back plane for a hexagonal cross section, a wood cell tilt of 20 degrees, and **wood cell rotation = 75 degrees.**

□ — spots due to the **front** (before tilt and rotation) face
■ — spots due to the **back** face
△ — spots due to the **right 1** face
▲ — spots due to the **left 1** face
◊ — spots due to the **left 2** face
⧫ — spots due to the **right 2** face

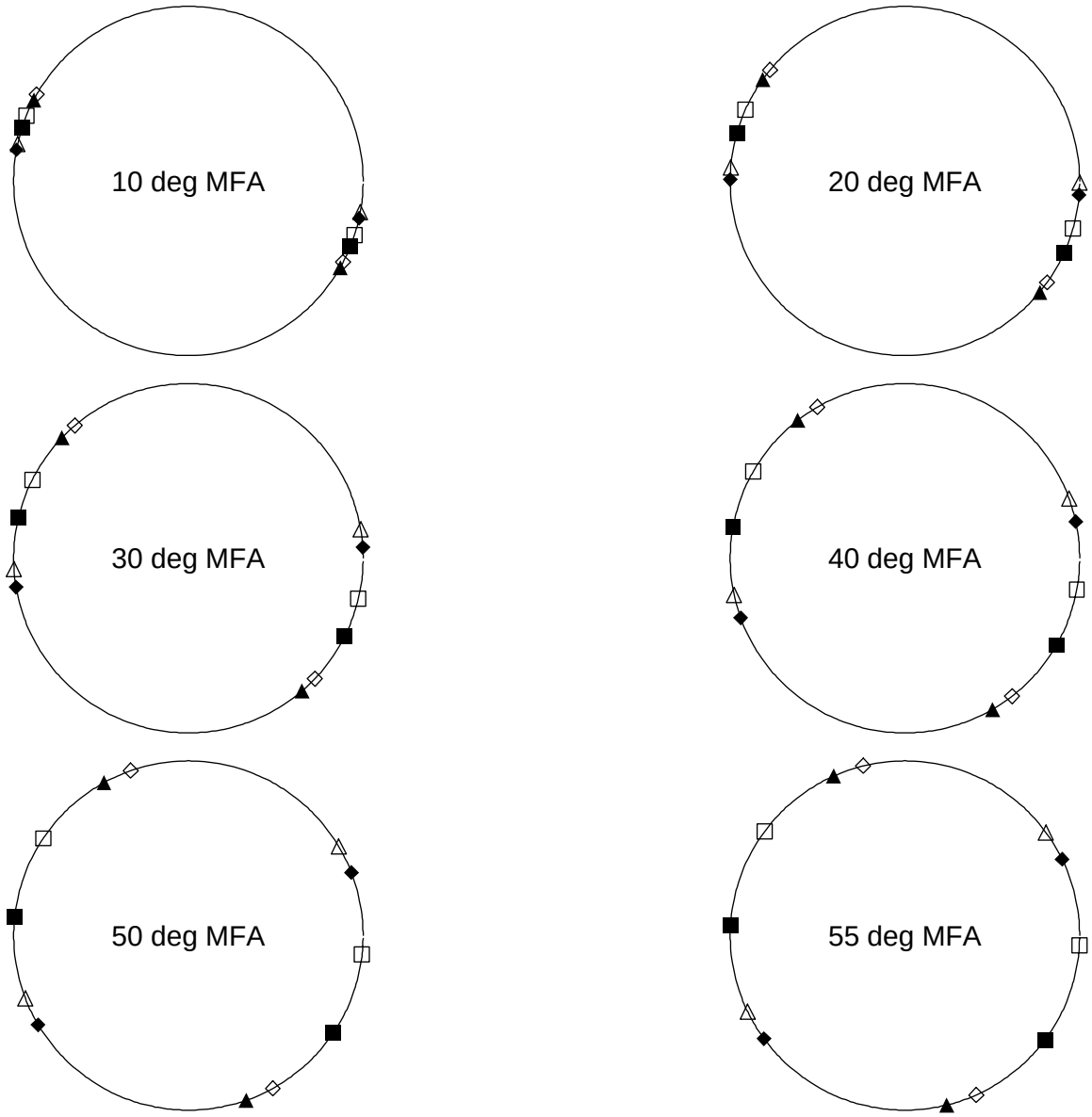

Figure 53: Locations of high-intensity X-ray spots on the back plane for a hexagonal cross section, a wood cell tilt of 20 degrees, and **wood cell rotation = 90 degrees.**

□ — spots due to the **front** (before tilt and rotation) face
■ — spots due to the **back** face
△ — spots due to the **right 1** face
▲ — spots due to the **left 1** face
◊ — spots due to the **left 2** face
⧫ — spots due to the **right 2** face